technische universität dortmund

XPS and XPD Investigations of Low-dimensional Silicon-based Surface-structures

Marie Schmitz

born in Datteln

- 2021 -

A document submitted in partial fulfillment of
the requirements for the degree of

Dr. rer. nat.

to the Faculty of Physics
TU Dortmund University, Germany

Supervised by
Prof. Dr. Carsten Westphal
Prof. Dr. Martina Müller

Abstract

This work deals with the analysis of the structural arrangement and the chemical properties of two silicon-based surface systems. The investigation is performed using x-ray photoelectron spectroscopy (**XPS**), x-ray photoelectron diffraction (**XPD**), and low-energy electron diffraction (**LEED**) techniques. Before the investigation of the systems, the clean and reconstructed surfaces are investigated using XPS, XPD, and LEED. Initially, a system with sub-monolayer platinum on a p(2×1)-reconstructed Si(100) substrate is prepared via electron beam evaporation. At 1/6 ML Pt a low-dimensional Si-Pt silicide forms after high temperature annealing at approximately $T \approx 1000\,°C$. High-resolution core-level XPS spectra of the Si $2p$ and Pt $4f$-signals indicate a bond between the Si and the Pt-atoms. There is no significant component that could show a Pt-Pt interaction. XPD measurements are taken of the Si $2p$ and Pt $4f$-signals and subsequently simulated using different starting structures. The best structure model reveals R-factors below 0.1 for both, Si $2p$ and Pt $4f$-signals. The unit cell of the structural arrangement contains 4 platinum atoms with a periodicity of $\left(\begin{smallmatrix} 3 & -6 \\ 4 & 0 \end{smallmatrix} \right)$. The top-most silicon layer rearranged in a cross-like structure between the Pt-atoms.

As second system, silicon is deposited onto a (2×1)-reconstructed Au(110) surface, forming a low-dimensional surface alloy. While the sample is held on a temperature of $T = 400\,°C$, 0.2 ML silicon are deposited via physical vapor deposition. The investigation with LEED reveals a combination of two overlapping domains described by the matrices $\left(\begin{smallmatrix} 10 & -2 \\ -1 & 4 \end{smallmatrix} \right)$ and $\left(\begin{smallmatrix} 10 & 2 \\ 1 & 4 \end{smallmatrix} \right)$. High-resolution core-level XPS measurements of the Au $4f$ and Si $2p$-signals showed two distinct components that could be assigned to Au-Si bonds. XPD pattern, recorded for Au $4f$ and Si $2p$ are simulated with different structural arrangements. R-factors below 0.1 indicate an excellent agreement with the measured data. The resulting structure model is consistent with the size of the unit cell obtained in the LEED measurement. Additionally, it agrees with the missing-row reconstruction of the substrate. In the structure model, the top-most Au-atoms are arranged between the Si-atoms.

Kurzfassung

Diese Arbeit befasst sich mit der Analyse der strukturellen Anordnung und den chemischen Eigenschaften von zwei siliziumbasierten Oberflächensystemen. Die Untersuchung wird mit Hilfe der Röntgenphotoelektronenspektroskopie (**XPS**), der Röntgenphotoelektronenbeugung (**XPD**) und der Niederenergie-Elektronenbeugung (**LEED**) durchgeführt. Vor der Untersuchung der Systeme werden die sauberen und rekonstruierten Oberflächen mit XPS, XPD und LEED untersucht. Zunächst wird ein System mit einer dünnen Schicht Platin auf einem $p(2 \times 1)$-rekonstruierten Si(100)-Substrat durch Elektronenstrahlverdampfung hergestellt. Bei 1/6 ML Platin bildet sich nach dem Ausheilen bei etwa $T \approx 1000\,°\mathrm{C}$ ein niedrigdimensionales Si-Pt Silizid. Hochauflösende XPS-Spektren der Si $2p$- und Pt $4f$-Signale weisen auf eine Bindung zwischen den Silizium- und Platinatomen hin. Es gibt eine signifikante Komponente, die eine Pt-Pt-Wechselwirkung anzeigen könnte. Es werden XPD-Messungen der Si $2p$- und Pt $4f$-Signale durchgeführt und anschließend mit verschiedenen Ausgangsstrukturen simuliert. Das beste Strukturmodell ergibt R-Faktoren unter 0,1 sowohl für Si $2p$- als auch für Pt $4f$-Signale. Die Einheitszelle der Strukturanordnung enthält 4 Platinatome mit einer Periodizität von $\left(\begin{smallmatrix} 3 & -6 \\ 4 & 0 \end{smallmatrix}\right)$. Die oberste Siliziumschicht ordnet sich in einer kreuzförmigen Struktur zwischen den Platinatomen um. Als zweites System wird Silizium auf eine (2×1)-rekonstruierte Au(110)-Oberfläche abgeschieden, wodurch eine niedrigdimensionale Oberflächenlegierung gebildet wird. Während die Probe auf einer Temperatur von $T = 400\,°\mathrm{C}$ gehalten wird, werden 0,2 ML Si durch physikalische Gasphasenabscheidung aufgebracht. Die Untersuchung mit LEED ergibt eine Kombination aus zwei sich überlappenden Bereichen, die durch die Matrizen $\left(\begin{smallmatrix} 10 & -2 \\ -1 & 4 \end{smallmatrix}\right)$ und $\left(\begin{smallmatrix} 10 & 2 \\ 1 & 4 \end{smallmatrix}\right)$ beschrieben wird. Hochauflösende XPS-Messungen der Au $4f$- und Si $2p$-Signale zeigen zwei unterschiedliche Komponenten, die Au-Si-Bindungen zugeordnet werden können. XPD-Muster, die für Au $4f$ und Si $2p$ aufgezeichnet werden, werden mit unterschiedlichen strukturellen Anordnungen simuliert. R-Faktoren unter 0,1 zeigen eine ausgezeichnete Übereinstimmung mit den gemessenen Daten. Das resultierende Strukturmodell stimmt mit der Größe der Einheitszelle überein, die bei der LEED-Messung ermittelt wurde. Außerdem stimmt es mit der Rekonstruktion der fehlenden Reihen des Substrats überein. In dem Strukturmodell sind die obersten Goldatome zwischen den Siliziumatomen angeordnet.

Contents

Chapter 1

Introduction

Physics is a science that deals with phenomena of various dimensions, ranging from large objects such as galaxies down to the smallest particles. The main field of solid-state physics is the world of atoms and molecules. The size of these constituents of matter is the nanoscale with structural dimensions of less than 100 nm. The understanding of how materials behave at this scale and the specific manipulation of these systems enables the synthesis of completely new material properties. The engineering of nanomaterials through the systematic positioning of single atoms or molecules was already envisioned in 1959 in Richard Feynman's talk 'There's Plenty of Room at the Bottom' [1]. In the last decades, scientists and engineers in many sub-disciplines of biology, chemistry and physics have been striving for the aim of 'manipulating and controlling things on a small scale'. Nowadays, nanotechnology finds application in fields of electronics, medicine, biology, aerospace, agriculture, and many more [2, 3]. Here, new materials with unique properties promise to build the technology of the future. The main purpose of nanoscience and nanotechnology is the preparation, characterization, and application of low-dimensional structures. Some of the possible atomic configurations on the nanoscale are clusters, quantum dots, nano-wires, nano-ribbons, nano-tubes, and many other assemblies [4–6].

The physical and chemical properties of a material can vary significantly depending on structural changes and also on the structure of the substrate surface to which they are deposited. Not only new electrical and mechanical characteristics can be found through the investigations of low-dimensional systems, also the thermal, magnetic, and optical nature of compounds can feature interesting new properties [2]. Furthermore, the structural arrangement and bonding state of the atoms are of fundamental and technological interest. The detailed understanding of the physical and chemical

states is crucial for the development of new applications at the nanoscale.

For the application of the low-dimensional materials, it is important to understand exactly under which conditions the structures form and what properties they exhibit. To understand their characteristics, the preparation steps must be entirely elucidated. An intermediate state between a clean surface and systems like nano-ribbons or nano-wires is often a surface alloy [5, 7]. In many cases, the systems are formed coexisting on the sample surface, which could have an impact on the primal properties of the nanostructures. Though the process of surface alloy formation is often unintentional, it has now become a common method for the analysis of the interaction of individual atoms of different materials [8]. As surface alloys offer the advantage of rapid and flexible preparation, they are commonly used for the investigation of chemical, magnetic, or electronic properties of composed materials [9, 10]. For the formation of surface alloy systems, a host material is equipped with one or more guest materials, mainly metals, alloying into the surface or a few layers beneath. If the main material is silicon, which is bond to a more electropositive element, silicides are formed.

Since early years of research silicon was one of the materials with easily admission and knowledge how to handle. It has become an indispensable part of technological applications in the semiconductor industry. Silicon as substrate or adsorbent material offers multiple interesting properties. In this work, two silicon-based surface-structures are investigated. The first structure uses silicon as substrate, while at the other structure silicon atoms are used as adsorbate. In the first material system, sub-monolayer platinum is deposited onto a silicon substrate. This system has been the focus of several studies [11–13]. For this material combination, using a Si(100) substrate, the formation of both, a nano-wire structure and also a Si-Pt silicide system, has been reported [5, 14].
For the second system, silicon is used as adsorbate. Literature showed that silicon has formed nanostructures on several materials as silver [15, 16] and gold [6, 17]. In both cases the deposition of silicon onto the (110) orientated surface leads to the formation of silicon nano-ribbons. For the gold substrate an additional alloy phase has been reported [7].

Favored analysis techniques for the detailed structural and chemical investigation of surface systems are, beside optical methods, the measurement of electrons or ions emitted from or scattered at the sample. Here, x-ray photoelectron spectroscopy

(**XPS**) is a powerful tool for the non-destructive investigation of the chemical environment present at the surface and interface. Additionally, x-ray photoelectron diffraction (**XPD**) [18] in combination with simulation methods is unique for the analysis of the structural arrangement of single atoms at and beneath the surface. These two methods in combination with low-energy electron diffraction (**LEED**) enable a detailed examination of the surface.

For the Pt/Si(100) system, there have been several surface investigations using scanning tunneling microscopy (**STM**) [11, 14] and LEED [12, 13] and also chemical studies of the Si-Pt silicide formation [5]. Yet, the results of the studies suggest different structural formations of the Pt-atoms on the surface.
For Si/Au(110), studies using STM, LEED, and density functional theory (**DFT**) are conducted, revealing structural suggestions for the silicon nano-ribbon and the Au-Si alloy system. A more detailed study of the structural arrangement using XPD reveals a new structure model of the silicon nano-ribbons [19]. For the Au-Si alloy no further XPD investigations were obtained until now.

The principal purpose of this thesis is the structural and chemical investigation of two low-dimensional silicon-based surface systems. One system with silicon as substrate and a second system with silicon as adsorbate. The structure of the thesis is as follows:
Chapter 2 introduces the theoretical background of the main experimental methods XPS, XPD, and LEED as well as the methodology for the data analysis.
Chapter 3 depicts the experimental setup of the UHV-chamber at beamline 11 at **D**ortmunder **EL**ek**T**ronen-Speicherring-**A**nlage (**DELTA**). The construction and the operation mode of the main components for sample preparation, and the analysis tools are introduced.
Chapter 4 presents detailed information on the elements silicon, platinum, and gold which are the main materials used in this thesis. Furthermore, an overview of the known surface reconstruction phases of Si(100), and Au(110) are displayed, followed by a characterization of low-dimensional surface systems consisting of those materials.
Chapter 5 deals with the results of a detailed structural, and chemical analysis of a clean and reconstructed Si(100) surface and also a Si-Pt silicide surface system. The analysis is conducted via LEED, XPS, and XPD methods.
Chapter 6 investigates the deposition of sub-monolayer silicon onto a Au(110)-surface and the formation of a low-dimensional surface alloy. A structural and

chemical characterization of the clean and reconstructed surface and the Au-Si alloy structure is performed using LEED, XPS, and XPD.

Chapter 7 summarizes the results of chapters 5 and 6, and also provides a short outlook for further measurements on the systems.

Chapter 2

Theoretical background

All solid, liquid, and gaseous matter is composed of atoms. Historically the idea of invisible building blocks from which matter is constructed was already recorded in the 5th century BCE by ancient Greek philosophers. In the last few centuries, improved research methods led to an improved picture of an atom. Yet, physicists found that atoms consist of a nucleus, composed of protons, neutrons, and surrounding electrons, with all three particles building the atomic compounds. Depending on the material, the number of these atomic compounds varies. A finite number of electrons are arranged on energetically different 'shells' around the nucleus (K, L, M, ...), which consist of more 'subshells', which are built from atomic orbitals. Each orbital is occupied by electrons that feature a specific energy. Depending on the element, the specific energies vary.

For a long time, atomic compounds were only considered as particles. Further experiments and quantum mechanical considerations revealed a mix of both, particle-like character and also wave-like nature. Since this mix is contradictory, the postulation of the wave-particle dualism was proposed, which gives a more reasonable description of the nature of atomic compounds. This quantum mechanical theory, developed by Werner Heisenberg, and also Erwin Schrödinger states that electrons exist as standing waves with the wave function Ψ, and the electron spin $s = \pm 1/2$. Each wave function can be characterized by different quantum number (**QN**) states:

QN	name	possible values	example
n	principal	$n \geq 1, \quad n \in \mathbb{N}$	$n = 1, 2, 3, ...$
l	azimuthal	$0 \leq l \leq n-1$	$l(n=3) = 0, 1, 2, ... (\equiv s, p, d, ...)$
m_l	magnetic	$-l \leq m_\mathrm{l} \leq l$	$m_\mathrm{l}(l=2) = -2, -1, 0, 1, 2$
m_s	spin	$-s \leq m_\mathrm{s} \leq s$	$m_\mathrm{s}(s=\frac{1}{2}) = -\frac{1}{2}, +\frac{1}{2}$

Electrons in an atom are divided into two different groups. The core-level electrons from the inner shells belong to the first group and are described by the nomenclature $\mathbf{nl}_j$. For example, a core-level electron state of the silicon atom with $n = 2$, $l = 1$, and a total angular momentum $j = |l \pm s| = 1/2$ is named Si $2p_{1/2}$. Furthermore, interatomic chemical bonds can lead to an overlap of the atomic orbitals. Due to the Pauli exclusion principle, it is impossible for two electrons to have the same values of quantum numbers in an atom or atomic compound. Thus the discrete energy levels split up forming multiple energetically proximal states, building the valence band. Electrons contributing to this continuum are part of the second group. Some materials feature a lack of occupied states leading to a band gap between the last occupied and the first unoccupied band. The first unoccupied band is the conduction band, where the electrons can move freely through the material. In metals, an overlap of the valence and conduction band leads to a high conduction property. In contrast to that, a large band gap in insulators leads to a non-conducting characteristic of the material. Furthermore, there are some materials that feature properties in between conducting and non-conducting states. Those type of materials are called semiconductors. They show both, insulating and conducting properties, depending on different influences like temperature, or doping with foreign atoms as impurities. A representative of this group of semiconductors is silicon.

2.1 Crystal structure

A crystal is composed of a periodic arrangement of atoms or particles. Its unit cell is the smallest unit from whose periodic continuation the crystal can be constructed. The unit cell of a 3D crystal is spanned by the lattice vectors $\vec{a}$, $\vec{b}$, and $\vec{c}$. Depending on the shape and size of the unit cell, and the constituent atoms, different atomic or molecular arrangements can occur. The simplest form of a single atomic arrangement is the simple cubic (**sc**) crystal system with one atom in the unit cell. By supplementing this basic structure with an atom in the middle of the cube a body-centered cubic (**bcc**) system is modeled with two basic atoms in the unit cell. Here, the cubic cell is a supercell and not the smallest building block of the structure. The addition of an atom on each side of the simple cubic system builds the face-centered cubic (**fcc**) structure with 4 atoms in the unit cell. The length of one side of the cube is denoted as lattice constant a, describing the size of the cubic unit cell. Two examples for fcc structures are given in sections 4.2 and 4.3. Beside these main cubic structures,

many variants with additional atom positions or different species on the lattice points exist. In total, 32 point groups exist in the three dimensional specification of crystals. In this work, essentially the fcc and the diamond cubic structure are of importance. Wherein the diamond structure consists of two interpenetrating fcc lattices, shifted by 1/4 along the diagonal of the unit cell. This leads to a number of 8 atoms in the cubic supercell. The orientation of vectors and planes in a crystal can be described
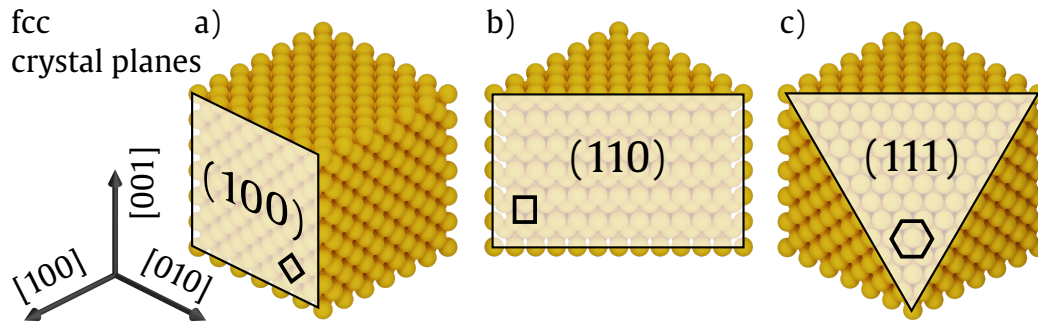

Figure 2.1 Illustration of different crystal surface planes of an fcc oriented crystal. a) displays the (100) orientation, b) shows a cut edge and the resulting (110) direction, and c) with a removed corner the (111) orientation of the crystal. The corresponding unit cell of the surface is displayed in a corner of the planes.

by the Miller indices. This notation uses the syntax of (hkl), where each h, k, and l are integers, proportional to the inverse value of the intersection points of the crystal axes. Negative values are denoted by a horizontal line above the index, for example $(\bar{1}10)$. Coordinates in square brackets describe a direction vector, for example [100], [010], or [001]. Miller indices in parentheses denote a crystal plane, like (100), (110), or (111) as displayed in figure 2.1. Related planes, shifted by the periodicity of the crystal have the same notation. Depending on the cut or growth of a crystal, different planes can be realized as surface plane. Thus, different atomic arrangements can be realized at the sample surface. As shown in figure 2.1 different cuts of an fcc crystal lead to different arrangements of the unit cell at the surface. In figure 2.1 a) the cubic crystal with a quadratic unit cell of the (100) surface is depicted. Cutting one edge of the same crystal as displayed in figure 2.1 b) leads to a (110) orientation of the new surface with a rectangular unit cell and a ratio of the lattice vectors of $\vec{a'} : \vec{b'} = \sqrt{2}$. The (111) orientation of the surface plane with a quasi-hexagonal unit cell at the new surface is achieved by cutting a corner of the cubic crystal as displayed in figure 2.1 c). The explicit unit cells of the surface structures of the materials used in this work are described in more detail in chapter 4.

2.2 XPS - x-ray photoelectron spectroscopy

The x-ray photoelectron spectroscopy (**XPS**), former called electron spectroscopy for chemical analysis (**ESCA**) [20], is a powerful tool in matters of nondestructive surface examination. Through the irradiation of a sample with x-rays electrons are excited. By analyzing the energy of these photoelectrons, information can be obtained about which species are present in the material and about the chemical bonding of the states. XPS allows the detection of all elements except hydrogen and helium. The information depth reaches several nanometers, because the inelastic mean free path (**IMFP**) of the photoelectrons ranges from $40 - 2500\,\mathrm{eV}$, thus XPS is extremely surface sensitive. As a common method for chemical analysis, it provides information individually or in combination with other methods. The chemical analysis is based on the fact that each element has its own spectral fingerprint. [21]

2.2.1 The photoelectric effect

The photoelectric effect is the fundamental principle of XPS. The effect is based on the impact of electromagnetic radiation on a sample, which may induce the emission of electrons. If the photon energy $h\nu$ of the incoming radiation is larger than the binding energy E_{bind} of an electron in the material, the electron may gain enough energy via absorption of the photon to leave the solid, causing a hole state. The principle process is depicted in figure 2.2. Exemplary three core-level states are displayed beside the much broader valence band states which include a wide range of binding energies. If an electron is excited from the solid, the conservation of energy applies, so the remaining energy from the photon is transformed into kinetic energy E_{kin} of the photo-released electron, called photoelectron, with

$$E_{\mathrm{kin}} = h\nu - E_{\mathrm{bind}} - \Phi. \tag{2.1}$$

An additional energy loss occurs in form of the work function Φ of the material. In order to improve measurement accuracy, the sample and the spectrometer should be at the same potential. This leads to an alignment of the Fermi levels [1], with $E_{\mathrm{kin}} = h\nu - E_{\mathrm{bind}} - (\Phi_{\mathrm{sample}} + \Phi_{\mathrm{spectrometer}} - \Phi_{\mathrm{sample}})$ [22]. If this condition is fulfilled, the measured kinetic energy is determined by the work function of the spectrometer $\Phi_{\mathrm{spectrometer}}$, which is an apparative constant that can be estimated from calibration

---

[1]If the sample is charged which appears at insulating samples or with poorly grounded samples, the Fermi levels are not aligned and an energy shift may occur.
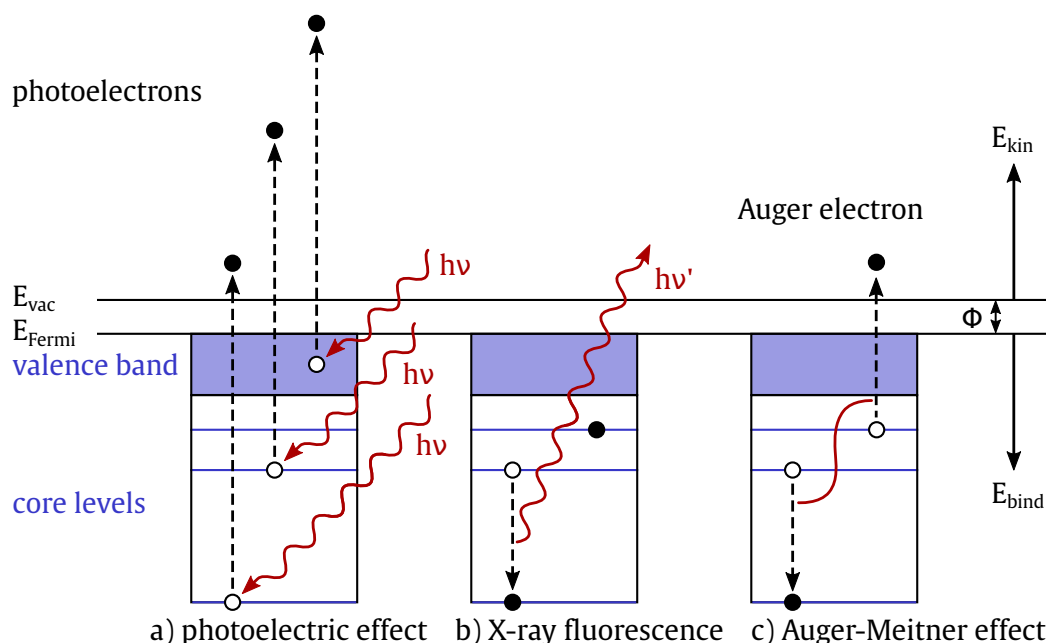
photoelectrons

E_{kin}

Auger electron

$h\nu$

$h\nu'$

E_{vac}

E_{Fermi}

valence band

Φ

$h\nu$

$h\nu$

core levels

E_{bind}

a) photoelectric effect   b) X-ray fluorescence   c) Auger-Meitner effect

Figure 2.2 Schematic view of a) photoelectric effect from different core-levels and from the valence band, b) relaxation process by fluorescent emission of another photon, and c) relaxation process by the Auger-Meitner effect.

measurements. Since the photonenergy $h\nu$ is monochromatic, the binding energy can be estimated from the value of the measured kinetic energy, which depends on the element, the orbital, and the bonding state of the exciting atom. After the electron is ejected, there are multiple ways to de-excite the atom and fill the remaining hole state. For example, the hole can be filled by an electron of a higher state as displayed in figure 2.2 b). The energy difference between the states can cause the emission of a photon with the excess energy $h\nu'$. This process is called x-ray fluorescence. Another effect that can occur as a result of the photoelectric excitation is the Auger effect[2], as displayed in figure 2.2 c). After emission of a primary photoelectron, a secondary electron from a higher state can fill the vacancy. The energy that is released during this relaxation process is high enough to excite another electron. These so-called Auger electrons hold an element-specific, constant energy, as their releasing energy results from the energetic difference between the energetic states.

---

[2]The effect named after the french physicist Pierre Victor Auger (1899-1993) is also known as Auger-Meitner effect, as it was former described by Lise Meitner (1878-1968) [23].
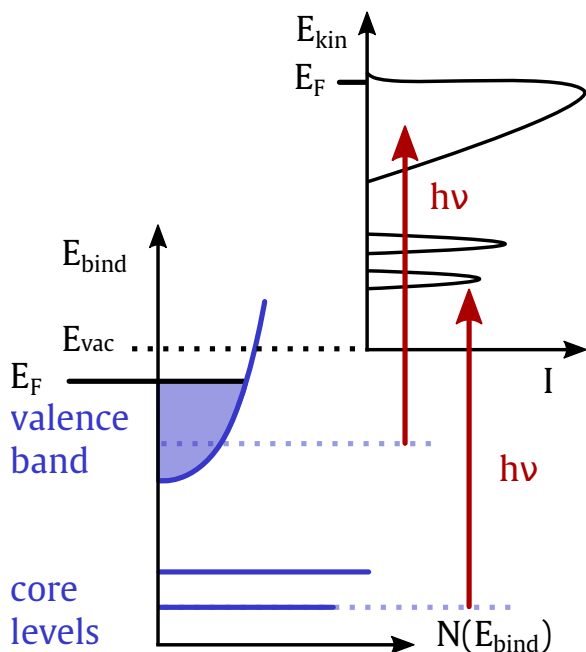
E_{kin}

E_F

$h\nu$

E_{bind}

E_{vac}

E_F

valence band

$h\nu$

I

core levels

$N(E_{bind})$

Figure 2.3 Schematic illustration of a photo-electron spectrum (top right) resulting from a particular density of states (bottom left).

Hence, the measured signal position is independent of the photon energy $h\nu$. The photo-emitted electrons are counted according their kinetic energy, as schematically shown in figure 2.3. Here, the excitation of photoelectrons from two core-level states and also the valence band and the resulting spectrum are displayed exemplary[3]. The red arrows display the excitation of electrons with monochromatic photons with the energy $h\nu$. Core-level excitation results in a sharp peak, while the broadly distributed states in the valence band lead to a broad signal in the spectrum. Because of the element-specific binding energy of electrons from different core-levels, different materials are identified by their characteristic spectral lines.

A comparison with former measurements in databases [24] enables an identification of the spectrum. Furthermore, it provides information about the chemical environment of single atoms in the material. Additionally, quantity of the present elements or bonds can be estimated by comparing the present signal intensities [21]. In order to perform XPS measurements, different irradiation sources may be used. The sample can either be excited with soft x-rays from an x-ray tube[4] or with synchrotron radiation.

Synchrotron radiation   has several advantages compared to conventional x-ray sources which makes it popular for XPS measurements. It is of a rather high brilliance and intensity, which is more than three orders of magnitude higher, compared to other sources like x-ray tubes, which enables a faster measurement [21]. Another great advantage is its tunability of the photon energy which for example allows the variation

---

[3]The common representation is a 90° rotated view of the upper right spectrum. For simplicity, all background effects have been omitted here.

[4]X-ray tubes often utilize K_{α} radiation from Mg with $h\nu = 1253.6\,\text{eV}$ or from Al with $h\nu = 1486.6\,\text{eV}$.

of measured layers. Synchrotron radiation is generated as charged particles are deflected from their trajectory. The deflection causes electromagnetic radiation which is used for the measurements, the so-called bremsstrahlung. For synchrotron radiation, multiple deflections are realized with undulators or wigglers that contain permanent magnets to curve the trajectory of the charged particles. To select a single energy from the resulting spectrum, a monochromator is used. A detailed description of a setup for the generation of synchrotron radiation is found in section 3.1.

2.2.2 Photoionisation cross-section

The generation of photoelectrons depends on material parameters like the type of element, the orbital number, and the excitation energy. The probability that a photoelectron is excited, is proportional to the cross-section $\sigma(\omega)$. The cross-sections of the elements with $1 \leq Z \leq 103$ have been calculated by Scofield [25]. The signals feature the highest value at the particular ionization point. In the XPS measurement, the different cross-sections lead to a variation of the line profile and intensity of the same measurement at different excitation energies. Therefore, the differential cross-section $d\sigma/d\Omega$ must be taken into account when selecting the photon energy. Furthermore, for a quantitative comparison of signals that origin from different elements, the differential cross-sections must also be considered.

2.2.3 IMFP - inelastic mean free path

As an electron is emitted its probability of reaching the surface falls with increasing depth of the emitting atom under the crystal surface, since the electron interacts with matter via elastic and inelastic scattering processes. Inelastic scattering causes energy losses of the electron. Even though the penetration depth of soft x-rays into the surface is rather high, the energy loss of the escaping electrons is limiting the escape depth to a few nanometers. Thus, XPS is a surface sensitive method including only the top-most layers of the sample. The inelastic mean free path (**IMFP**) λ_{in} is a quantitative indicator for the average distance an electron travels trough the crystal until the energy loss is below $1/\mathrm{e} \approx 37\,\%$. Thus, the energy loss can be expressed by the intensity $I(d)$ of an electron bunch with initial intensity I_0 after passing a distance d in the crystal:

$$I(d) = I_0 \mathrm{e}^{-d/\lambda_{\mathrm{in}}}, \tag{2.2}$$

which is similar to the Beer–Lambert–Bouguer law that describes the attenuation length of light, traveling through matter [26]. For the electron, the IMFP λ_{in} is independent of the angle of light-incidence, but primary depends on the kinetic energy of the electron, hence the photon energy, and also on the type of element. Several ways to describe the IMFP are described in the following.

The 'universal curve', established by Seah and Dench [27] represents an empirical estimated IMFP of multiple elements as function of the photoelectron energy. The IMFP λ_{SD} is described by

$$\lambda_{\mathrm{SD}} = \frac{538\,a}{E_{\mathrm{kin}}^2} + 0.4\,a^{0.75}E_{\mathrm{kin}}^{0.5}. \tag{2.3}$$

For $E_{\mathrm{kin}} > 100\,\mathrm{eV}$ the term $\frac{538a}{E_{\mathrm{kin}}^2}$ can be neglected. The parameter a describes the mean atomic distance with

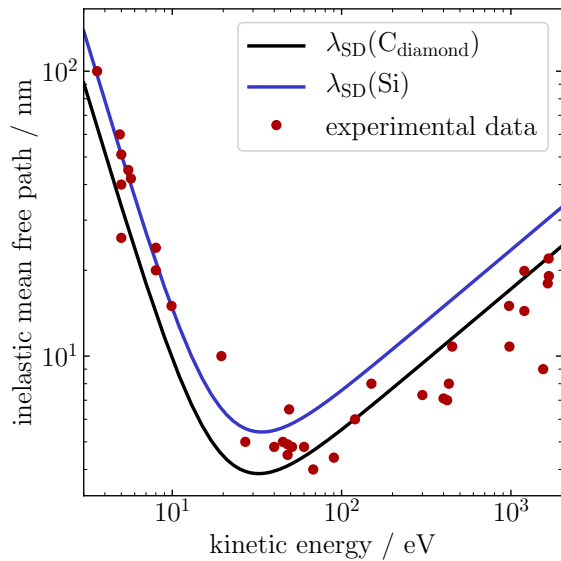$$a = \left(\frac{M}{\rho N_{\mathrm{A}}}\right)^{1/3}. \tag{2.4}$$

Here, M is the atomic mass, ρ the material density, and N_{A} the Avogadro constant. The 'universal curve' yields the IMFP in the right order of magnitude, and represents a good estimate for most materials. In figure 2.4 the 'universal curve' is displayed exemplary with measurements of several different elements in red and calculations for silicon and carbon in blue and black line color, respectively [28]. The minimum of the curve is at approximately $50\,\mathrm{eV}$. As indicated in figure 2.4 a difference between the theoretical curves of different elements occurs. For some data points, the measured values deviate by up to 50% from the theoretical predictions. Especially at high energies, the agreement with current theoretical calculations is no longer given, and the estimation is no longer accurate. [21, 29]

Figure 2.4 The 'universal curve' for the inelastic mean free path of electrons in solid samples.

The TPP-2M equation by Tanuma, Powell, and Penn [28, 30] gives a more detailed and element-specific method for estimating the IMFP. The expression describes the IMFP λ_{in} for kinetic energies between 50 and 2000 eV:

$$\lambda_{\text{in}} = \frac{E_{\text{kin}}}{E_{\text{p}}^2 \left[\beta ln(\gamma E_{\text{kin}}) - (C/E_{\text{kin}}) + (D/E_{\text{kin}}^2) \right]} \tag{2.5}$$

with

$$\beta = -0.10 + 0.944(E_{\text{p}}^2 + E_{\text{g}}^2)^{-0.5} + 0.069\rho^{0.1}, \qquad C = 1.97 - 0.91U,$$
$$\gamma = 0.191\rho^{-0.5}, \qquad\qquad\qquad\qquad\qquad D = 53.4 - 20.8U,$$
$$U = N_\nu \rho/M = E_{\text{p}}^2/829.4, \qquad\qquad\qquad E_{\text{p}} = 28.8(N_\nu \rho/M)^{0.5},$$

and E_{kin} as kinetic energy of the electrons, E_{p} as free-electron plasmon energy, E_{g} the band gap energy for non-conductors, ρ as material density, N_ν as number of valence band electrons per atom, and M as atomic unit weight. The IMFP calculated for different elements can be derived from databases like [31]. From the IMFP, the surface sensitivity can be estimated for XPS and XPD measurements.

2.2.4 Angle dependent surface sensitivity

The sensitivity of electron spectroscopy to bulk- or surface-atoms can mainly be varied by two effects.

First, the variation of the photon energy leads to a variation in the IMFP of the photoelectrons, thus the escape depth (**ED**)[5] of the photons and simultaneously the information depth (**ID**)[6] changes. Thus, at high kinetic energies, the bulk sensitivity is enhanced while at low kinetic energies a surface sensitive measurement is emphasized.

Second, a variation of the angle of incidence Θ yields in a surface sensitive measurement as displayed in figure 2.5. At measurements of $\Theta = 0°$, corresponding to normal emission, the ID equals the ED and reaches 5λ into the crystal considering 99% of the signal. Though the ED remains unchanged by variation of the angle, the ID in the sample gets smaller. This effect allows to enhance the surface sensitivity at angles

---

[5]ED denotes the effective length from which the electrons can escape from the sample [29].

[6]ID indicates the layer thickness from which a certain percentage of the measured signal originates. Based on an exponential decay of the signal, the ID can be estimated by 5λ [21].

of $\Theta \gg 0°$. While comparing a bulk sensitive measurement with a surface sensitive spectrum, the proportion of different chemical components provides information about the position depth of the atoms located in the sample.
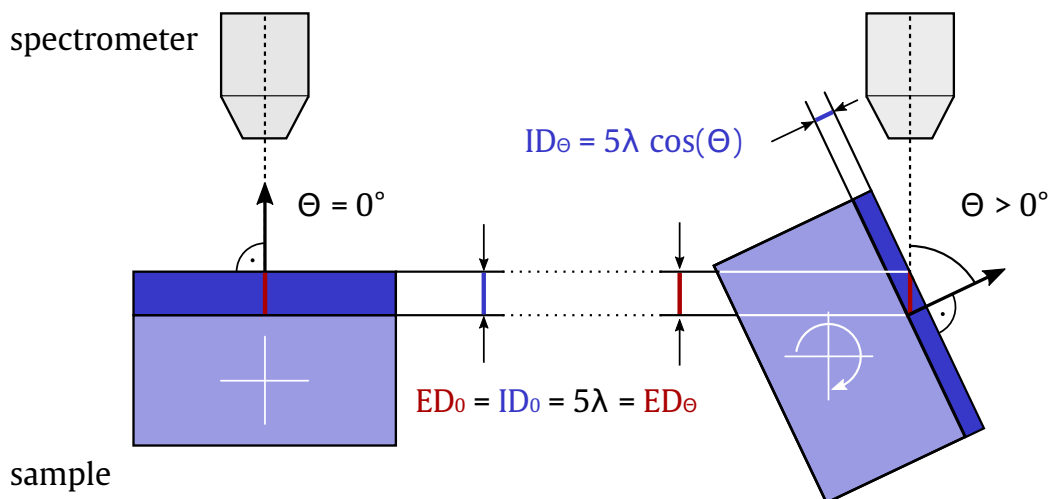

spectrometer

$ID_\Theta = 5\lambda \cos(\Theta)$

$\Theta = 0°$

$\Theta > 0°$

$ED_0 = ID_0 = 5\lambda = ED_\Theta$

sample

Figure 2.5 Illustration of the emission angle dependence of photoelectron spectroscopy measurements. The escape depth is 5λ considering 99% of the signal.

2.3 Processing of XPS data

For a general identification of the elements contained in the material measured, a survey spectrum over a wide energy range can be recorded. In the core region, with binding energies of $E_{\text{bind}} \geq 30\,\text{eV}$, different chemical environments lead to overlapping peaks originating from distinct chemical states. Each element has its own unique composition of energetic positions in the spectrum. In the spectrum a composition of elements is approximately the sum of the single element lines. An identification of composed elements is achieved by comparing the measured binding energies to reference data like the NIST x-ray photoelectron spectroscopy database [24]. In a detailed analysis applying a careful curve fitting procedure to measured high-resolution core-level XPS spectra, information about the elemental and chemical states of the sample may be obtained. Since the total number of counts in the spectrum measured is not important for this type of data analysis, the spectra are normalized. Furthermore, the electron background from inelastic scattering has to be removed from the experimental data, as described in section 2.3.1. The binding energies of the various components in a spectrum reveal the sample's chemical composition and their binding

states. The relative peak area to signals of different elements provides information on the sample's chemical composition. In this work, all high-resolution core-level XPS spectra are fitted using the software UNIFIT 2020 [32] which provides a simultaneous modulation of background and peak shape during the fit procedure, finding a local minimum. For a successful procedure it is important to start the fit with a good initial guess depending on sample and experimental properties. Sometimes a fit procedure may lead to a result corresponding to no real physical structure of the sample. Therefore, the initial set of start-parameters must be carefully chosen. The fit quality was checked and confirmed by applying to obtained results from a fit to known reference samples. The fit procedure contains different characteristics which are described in the following section. [33]

2.3.1 Background modeling

An important processing step is the background determination. For the background of XPS spectra several methods have proven to be useful separating[7] the so-called extrinsic electrons from the pure photoelectron signals. Simple methods for the background estimation of spectra from primary unscattered surface electrons are a constant, a linear, or a polynomial background of low order. In the measurement of electrons of buried layers and interfaces, a crucial effect contributing to the formation of the background is the energy loss of electrons. Excited photoelectrons collide inelastically with atoms or molecules, losing a continuous amount of energy, generating the inelastically-scattered electron background, forming a 'stepped' function towards lower kinetic energies of the peaks. If the kinetic energy of the excited photoelectrons is high enough, they can excite secondary electrons from the core or valence levels. This contributes in a secondary electron cascade background, appearing at low kinetic energies in the spectrum. The combination of those effects results in a continuous background in the spectrum which is shifted towards lower kinetic energies. Therefore, a constant or linear background is not sufficient for a proper fit of the data [32–34]. For a better representation of the background in the fit procedure, the function can be described by

$$F(E) = \int_E^{E_{\max}} K_{\mathrm{j}}(E' - E) I'(E') \mathrm{d}E', \tag{2.6}$$

---

[7]After separation the background can be removed from the main spectrum. This work refrains the removal of the background for comparability and verification of the shape.

with $I'(E)$ as the spectrum at energy E and K_j an inelastic energy loss cross-section function [34]. Depending on the loss function K_j different background shapes can be modeled.

The Shirley-background function is exemplary displayed in figure 2.6. It was introduced by D. A. Shirley [34, 35] and is an iterative method with the assumption of the proportionality between the intensity of the background at a given energy E and the total intensity at higher kinetic energies:

$$F_\mathrm{S,i}(E) = k \int_E^{E_\mathrm{max}} (I(E') - F_\mathrm{S,i\text{-}1}(E')) \mathrm{d}E'. \tag{2.7}$$
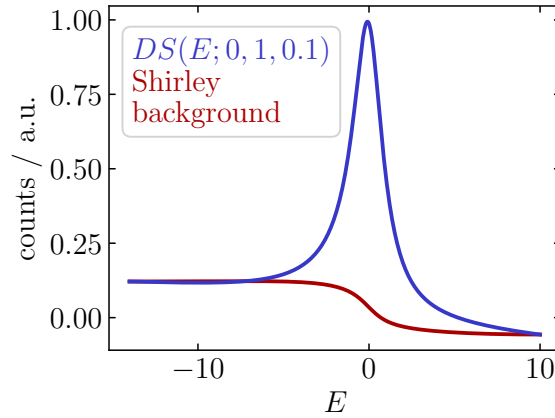
Figure 2.6 Shirley-background function fitted to a Doniach-Sunjic lineshape.

The iterative Shirley-background calculation can be approximated using the inelastic energy loss cross-section function K_S with the loss energy $T = E' - E$:

$$K_\mathrm{S}(T, B_\mathrm{S}, C_\mathrm{S}) = \frac{B_\mathrm{S}}{C_\mathrm{S} + T^2}, \tag{2.8}$$

where the first approximation of the Shirley-background function $F_\mathrm{S,0}(E)$ is a constant background [36]. By the assumption of $F_\mathrm{S,i,min} = I_\mathrm{i,min}$ the parameter k is determined. B_S and C_S are Shirley parameters, which are optimized during the fitting procedure. The Shirley method is a good approximation and more precisely than a simple linear background. For asymmetric shapes, an alternative calculation was established [32, 35].

The Tougaard-background function is a closely related method and a more detailed description of the background, introduced by S. Tougaard [37, 38]. The three-parameter background algorithm uses the energy dependent loss function K_T for equation 2.6:

$$K_\mathrm{T}(T) = \frac{B_\mathrm{T}T}{(C_\mathrm{T} + T^2)^2 + D_\mathrm{T}T^2}, \tag{2.9}$$

with B_{T}, C_{T}, and D_{T} as material depen-
dent Tougaard parameters. The cross-
section compromises inelastic scatter in
the sample and also the scattering in-
teraction in multiple layers with differ-
ent cross-sections [34, 38]. In comparison
to the other presented background cal-
culations, the Tougaard function is the
physically most accurate method for the
description of the background function.
To account for double to triple scatter-
ing processes it is recommended that the
spectrum is extended over a range of at
least 50 eV [32, 37, 39].
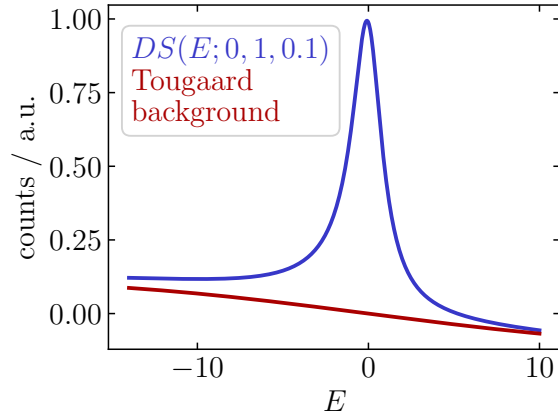
Figure 2.7 Tougaard-background function fitted to a Doniach-Sunjic lineshape.

2.3.2 Line profiles

This section presents the commonly used line profiles for XPS peaks. For the correct analysis of a spectrum consisting of a single or of multiple components, a correct mathematical model for peak modeling is crucial. The composition of multiple peaks in a spectrum can be described as the sum of single peaks. In the peak fitting process the line profiles of the components are characterized by multiple parameters. The main position, the FWHM, the area, and a Lorentzian-parameter can be attributed to each peak. Additionally, a Gaussian-parameter and a value for an asymmetric character of the line profile can be applied.

The Lorentzian function (also Cauchy distribution) defines the 'natural linewidth' of a peak and originates from the finite lifetime of a core-level hole state. As an electron escapes from its core-level, the refilling of the state happens within a characteristic time delay Δt. This effect is caused by the uncertainty principle, postulated by Heisenberg $\Delta E \Delta t \gtrapprox \hbar/2$. This results in a broadening of a peak with:

$$L(E, E_0, \sigma_{\mathrm{L}}) = \frac{1}{\pi} \frac{\sigma_{\mathrm{L}}}{(E - E_0)^2 + \sigma_{\mathrm{L}}^2}. \tag{2.10}$$
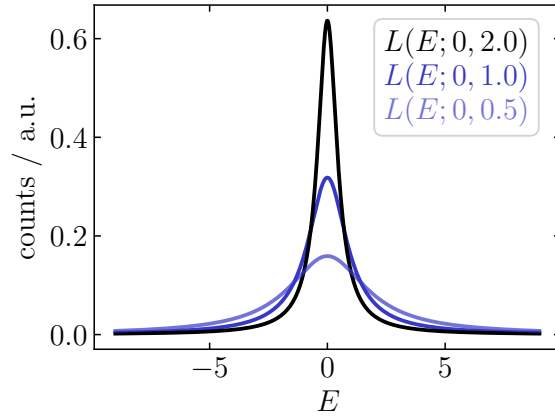
Figure 2.8 Lorentzian function $L(E, E_0, \sigma_L)$ with varied parameter σ_L.

Here, E_0 is the central energy of the peak and σ_L is the Lorentzian FWHM. The Lorentzian function is displayed exemplary in figure 2.8 for $E_0 = 0$, and varied σ_L. The peak shape is a symmetric broadening around the center. An increase of lifetime broadening can be observed at higher binding energies, thus for deeper core-levels. A common approximation of the effective line profile of the measured XPS signals is realized with a combination of Lorentzian and Gaussian-distribution [33].

The Gaussian function, displayed exemplary in figure 2.9, can be described by:

$$G(E, E_0, \sigma_G) = \frac{1}{\sigma_G \sqrt{2\pi}} \exp\left(-\frac{(E - E_0)^2}{2\sigma_G^2}\right). \qquad (2.11)$$
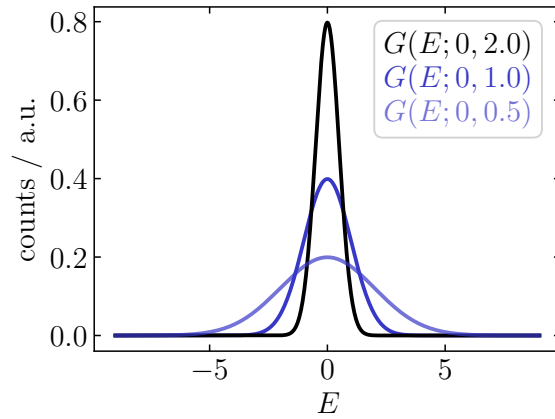
Figure 2.9 Gaussian function $G(E, E_0, \sigma_G)$ with varied parameter σ_G.

Here, E_0 is the central energy and σ_G is the Gaussian-standard deviation. One of the main instrumental parameters with a great impact on the shape and resolution of the signal is the pass energy (**PE**) of the spectrometer. The measurement accuracy of the spectrometer has a major influence on the Gaussian broadening of the peak. Another effect with impact on the peak shape is the coupling of the XPS process with phonon vibrations which is temperature dependent. In compound samples like oxides and carbonates optical phonons with high energies dominate the process. In metallic samples the phonons appear with acoustic nature, with a rather low energy. This causes pure metal signals to have a narrower peak shape with a large Lorentzian ratio and compounds with a more Gaussian char-

acter [33]. Furthermore, chemical, structural, and electronic influences can lead to a Gaussian-broadening, too.

The Voigt function is the convolution of the Lorentzian and the Gaussian function[8] and a frequently used function for fitting XPS spectra. It combines both, the sample and experimental broadening of the line profiles:

$$V(E, \sigma_G, \sigma_L) = L(E) * G(E) = \int_{-\infty}^{+\infty} L(E', \sigma_L) G(E - E', \sigma_G) dE' \qquad (2.12)$$

Exemplary Voigt functions are displayed in figure 2.10 with varied Lorentzian and Gaussian-parameters σ_G and σ_L. The ratio of Lorentzian and Gaussian-components varies, depending on the material composition. For metallic samples the Lorentzian-component has a major impact. An effect that typically occurs in XPS spectra of metallic samples which is not considered by the Voigt function is an intrinsic asymmetry of the signal. This originates from the band structure of the material. Further impacts leading to an asymmetric character of the signal can be the response function of the spectrometer. It should be noted that the degree of asymmetry of the peak can vary, depending on the background calculation method. Some calculations, including the Shirley function already consider an asymmetry in the spectrum. For a linear or a Tougaard-background the asymmetry has to be included in the line profile. One possible solution is to add an exponential tail to the Voigt function which however may reduce the flexibility of modeling the line profile. Another solution is to include an asymmetry factor in the line profile. [33, 39]
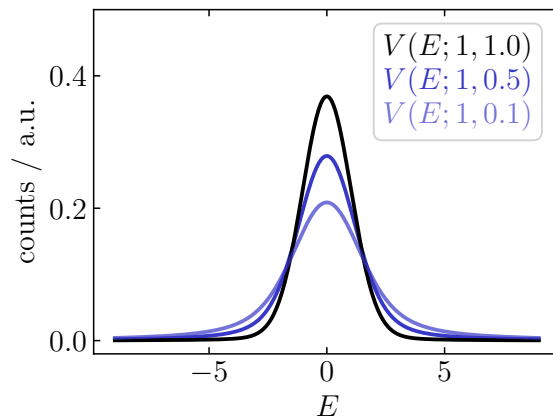

Figure 2.10 Voigt function $V(E, \sigma_G, \sigma_L)$ with varied parameter σ_L.

---

[8]For XPS fitting also sum (GLS) and product (GLP) functions of Gaussian and Lorentzian functions have been used, so-called pseudo-Voigt functions.

The Doniach-Sunjic function is composed of a Lorentzian-profile, where an asymmetric shape of the peak is considered:

$$DS(E, E_0, \alpha, \beta) = \frac{\cos\left[\frac{\pi\alpha}{2} + (1-\alpha)\tan^{-1}(\frac{E-E_0}{\beta})\right]}{[(E-E_0)^2 + \beta^2]^{\frac{1-\alpha}{2}}}, \qquad (2.13)$$

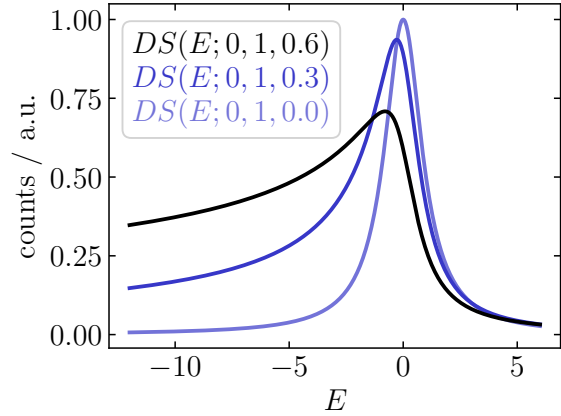with β related to the FWHM and α as asymmetry parameter. In figure 2.11 exemplary Doniach-Sunjic profiles with a fixed E_0 and asymmetry parameter α, and a varied parameter β are displayed. For an asymmetry of $\alpha = 0$ the function possesses a Lorentzian-like shape. While using the Doniach-Sunjic function for peak fitting, care should be taken in spectra with an extended exponential tail. If further components are included in this tail, their signal can be suppressed by the tail of the main component [40]. For the XPS peak fitting procedure commonly a convolution of the Doniach-Sunjic and a Gaussian function is applied:

Figure 2.11 Doniach-Sunjic function $DS(E, E_0, \alpha, \beta)$ with varied parameter β.

$$V_{\mathrm{DS,G}}(E) = V(DS(E) * G(E)) = \int_{-\infty}^{+\infty} DS(E', \alpha, \beta)G(E - E', \sigma_{\mathrm{G}})\mathrm{d}E', \quad (2.14)$$

This supplements the Lorentzian-component with the Gaussian-shape and also provides the possibility of modeling an asymmetric lineshape.

2.3.3 Spin-orbit coupling

For electrons in an s orbital with the momentum QN $l = 0$ only one peak component appears. For $l > 0$ (p, d, and f levels) the so-called spin-orbit coupling separates the component into a doublet. The angular momentum QN j of electrons from a certain level can occupy two different states with $j = |l \pm s|$, with parallel or anti-parallel ordering of orbital angular momentum and spin. Due to this interaction of the magnetic moments of the electrons, the spectrum can be divided into a pair of two neighboring peaks. Table 2.1 describes the ratio of the degeneracies (2j+1). Here,

the magnitude of the spin-orbit separation depends on the atomic number and on the distance to the nucleus. With increasing Z the distance of the doublets gets larger. The area ratio of the doublet components depends on the orbital as shown in table 2.1. [39]

Table 2.1 Spin-orbit split parameters.

Orbital	j-values	area ratio
s	1/2	
p	1/2, 3/2	1 : 2
d	3/2, 5/2	2 : 3
f	5/2, 7/2	3 : 4

2.3.4 Chemical shift

In a sample, atoms from the same element can be located in different chemical environments. These different chemical environments of the core-level electrons cause a modification in the effective charge potential[9], leading to a modified binding energy termed 'chemical shift'. A shift to higher and also to lower binding energies is possible, depending on the electronegativity, the proton affinity or thermodynamic data [39]. Thus, the binding energy of the components is an indicator of the chemical environments present in the sample. Furthermore, different chemical environments can lead to a changed peak shape and peak width, and also to a modified appearance of the valence band. Additionally, satellite signals may occur. The peak areas to the different components in the spectrum and their ratio can provide information on the quantity of the chemical environments. Since chemically shifted peaks often overlap each other and different fit models may be suitable, it is recommended to compare their binding energies to literature or to databases [24].

2.3.5 Further features

In the XPS spectrum, further features can appear due to different processes. Some of the most important effects and signals are outlined in the following.

Valence band spectra typify the density of states of the electrons in the valence band. Different structural arrangements also exhibit different valence band states, thus using high-resolution valence band spectra, it is possible to distinguish between different structures. Because of the broad overlap of peaks in the spectrum, a decomposition to individual components requires an extensive analysis. At the end of a full

---

[9]Further effects include screening and relaxation, see section 3.2.3 in reference [21].

energy range spectrum at high kinetic energies, the valence band spectrum shows a sharp edge after the overlap of peaks. This Fermi edge can be used for calibrations of the binding energy range. [21]

Plasmon loss peaks occur mainly in materials with a high electron density around the Fermi level. After the photoelectric effect, a core-hole is filled with an electron from the 'Fermi-sea' which causes a density shift. As compensation reaction, the remaining free electron gas causes collective oscillations of the electrons in the conduction band. Due to these collective lattice vibrations, the excited photoelectrons feature discrete energy losses. The plasmon features can appear as bulk and also as surface plasmons. The signals are shifted in discrete distances towards lower kinetic energies in relation to the main photoelectron peaks. Extrinsic and intrinsic plasmon vibrations originate from the stimulation by electrons and core-holes, respectively. Plasmon loss peaks in a XPS spectrum can be seen as indicator for a clean surface. [21]

Shake-up signals are further features, which an XPS-signal can be accompanied. Immediately after the photoelectron process ionized atoms remain in the sample. Some of those ions can remain in an excited state, a few electron volts above the ground state. In this shake-up process, the kinetic energy of the excited photoelectron is reduced by the discrete energy difference between those states. The number, strength and energy shift of the satellite peaks depends on the material. [21]

The Auger-Meitner effect is described in section 2.2. The vacancy of a photoemitted electron is filled by another electron from a higher shell. The relaxation process causes the emission of a secondary electron. The notation is, for example, (KL_1M) for a primary photoelectron of the K shell, a filling electron from the L shell, and a secondary electron from the M shell. [41]

2.4 XPD - x-ray photoelectron diffraction

The basic principle of the x-ray photoelectron diffraction (**XPD**) is an angle-resolved measurement of high-resolution core-level XPS spectra. When a core-level electron is emitted with a photon energy $h\nu$, the process can be described as spherical electron wave around the emitter atom. As the primary electron wave $\Psi_0(\vec{k})$ propagates
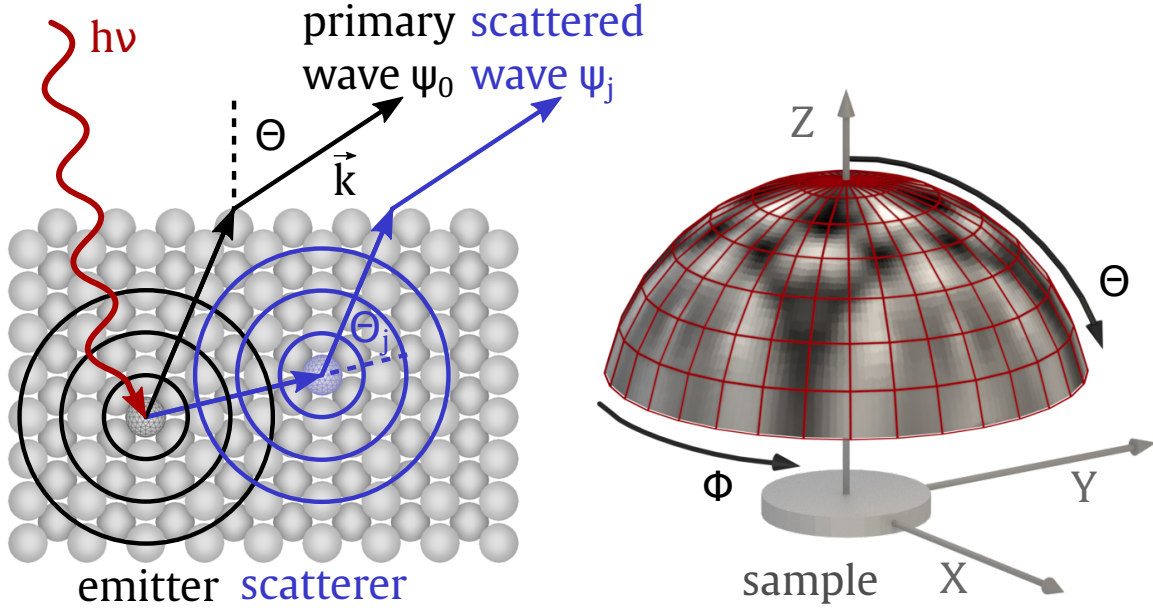
Figure 2.12 Simplified theoretical principle of photoelectron diffraction, reproduced from [42]. The incoming beam with the energy $h\nu$ causes a primary electron wave. As the primary wave propagates through the material, it is scattered at secondary atoms, here displayed in blue. The interference of primary and scattered waves causes an angle dependent modulation, as displayed on the right.

through the material as shown on the left in figure 2.12, the wave function can be described by:

$$\Psi_0(\vec{r}) \propto \frac{e^{i\vec{k}|\vec{r}|}}{|\vec{r}|}, \tag{2.15}$$

with r as distance to the emitting atom and the wave vector $\vec{k}$ which depends on the kinetic energy and on the direction of propagation. In the photoemission process the parallel component remains with $\left|\vec{k}_{||}\right| = \sqrt{\frac{2m}{\hbar^2}E_{\text{kin}}} \cdot \sin(\Theta)$. As the amplitude decays with $1/r$, the technique is rather sensitive to the local environment of the emitter atoms. The emitted photoelectron can be scattered elastically at neighbor atoms, thus generating a secondary wave $\Psi_j(\vec{k})$. The superposition between both waves leads to angle dependent constructive or destructive interference. Thus the path difference depends on the location and element of the neighboring atoms of the emitter atom. Considering multiple scattering at different neighbor atoms j, the final-state wave function consists of the initial wave and the sum over all scattered waves [43]:

$$I(\vec{k}) = |\Psi_0(\vec{k}) + \sum_j \Psi_j(\vec{k})|^2 \tag{2.16}$$

The photoelectrons experience an additional diffraction at the transition between solid and vacuum due to the inner potential of the solid V_0 with:

$$\frac{\sin(\Theta_{\text{sol}})}{\sin(\Theta_{\text{vac}})} = \sqrt{\frac{E_{\text{kin}} + V_0}{E_{\text{kin}}}}, \tag{2.17}$$

here Θ_{sol} and Θ_{vac} are the polar angles in the solid and in the vacuum, respectively. XPD measurements can be taken either by variation of the photon energy at a fixed angle, or by variation of the angle, while keeping the photon energy constant. In the latter mode, the polar angle or azimuthal angle are varied in a line scan or in a full hemispherical scan as displayed on the right in figure 2.12. A more detailed but more time-consuming method is the variation of both, Θ and Φ angles, generating a 2π diffraction pattern above the sample [43]. Therefore, this method is used in this work. For a proper structure determination with adequate measurement time, it is necessary to record between 4000 and 6000 spectra for a single XPD pattern. In order to obtain information about the structural arrangement of a surface structure measured by XPD, the experimental XPD pattern is compared to a simulated pattern.

2.5 Processing and simulation of XPD data

This section describes the processing of the measured XPD pattern and the subsequent simulation routine using cluster models. The simulations are performed using the GeneticEVA program [44]. The packages included and important parameters are presented below.

2.5.1 XPD data processing

The experimental XPD pattern of the hemispherical measurement of the sample consists of 4000-6000 individual XPS spectra. For the analysis and simulation of the XPD pattern, the measured data of the XPD pattern must be processed in several steps. An example of data processing is shown in figure 2.13 for a Si $2p$ XPD pattern of a Pt covered Si(100) surface. The raw data mostly consists of several measurements, with different amount of background. Since the background is also recorded during the measurement, it can be removed. While the intensity of the synchrotron radiation decreases during the measurement, a sudden increase in intensity can be observed
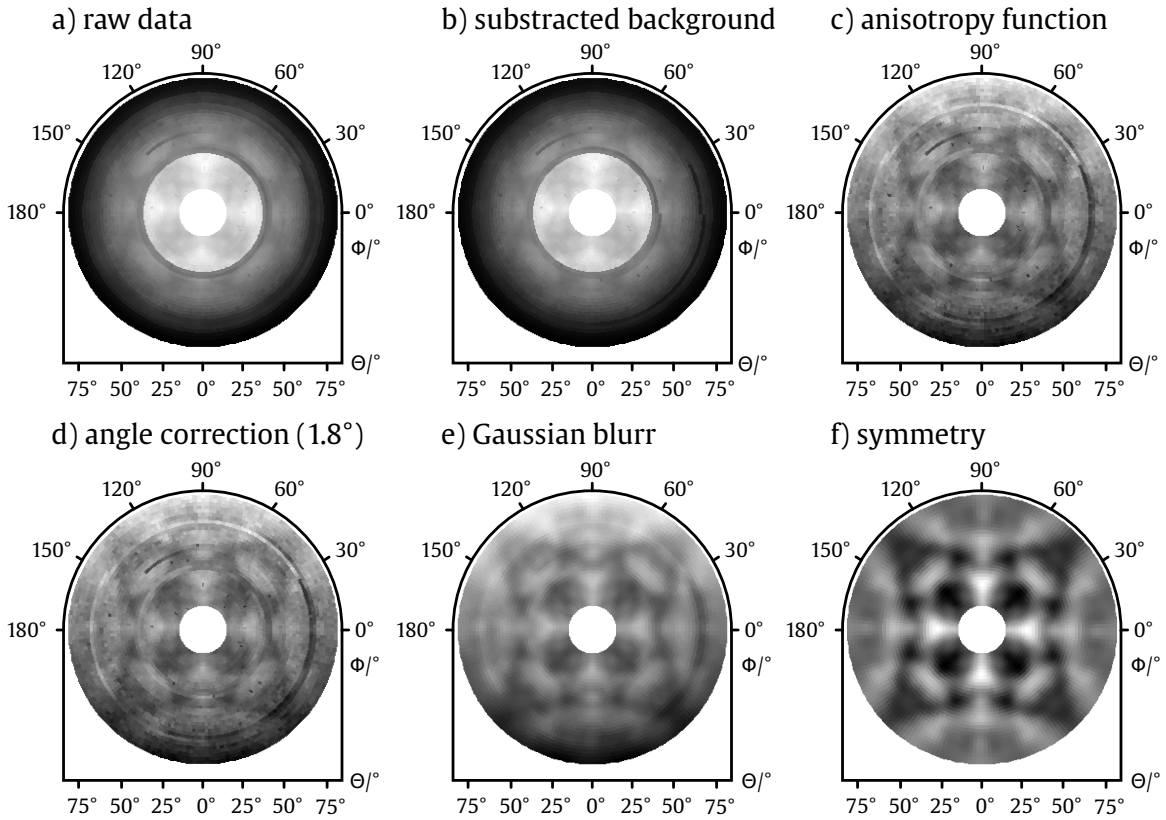
Figure 2.13 Data processing steps of a Si $2p$ XPD pattern of sub-monolayer Pt on Si(100). Pattern a) with raw data, b) with substracted background, c) after application of the anisotropy function, d) after an angle correction of $\Delta\Theta = 1.8°$, e) with a small Gaussian-filter with r= 2, f) after the applying a mirror symmetry and 4-fold rotational symmetry.

after an injection. In order to compensate these effects, an anisotropy function is applied to the data:

$$X(\Theta, \Phi) = \frac{I(\Theta, \Phi) - I(\Theta)}{I(\Theta)}. \tag{2.18}$$

To avoid the sudden step from one polar angle Θ to the next, a step removal is applied. If the pattern is not aligned in the right direction, an angle correction can be made for a horizontal or vertical alignment. Minor statistical noise can be compensated by a small Gaussian-filter. Finally, if symmetry is present, mirroring and also 2-, 3-, or 4-fold rotational symmetry can be applied to the pattern.

2.5.2 XPD simulation

In order to draw conclusions from the measured data on the surface structure, a simulation of the XPD pattern was performed. The simulation steps are described in the following and displayed schematically in figure 2.14. Based on literature, an initial model strucutre of the sample was generated. If the structural arrangement of the surface or interface atoms is completely unknown, an initial guess of the atom locations must be made. For the simulation, the atoms of the unit cell are set as emitter atoms. The region in which the photoelectrons are possibility involved in the scatter processes is the emitter radius. Typical values of the scatter radius are 1.5 and 2.0×IMFP for simulations with the EDAC [45] and the MSPHD [46] package, respectively. Single atom locations or groups of atom locations may be modified within the simulation by a translation, a cluster scaling, and a rotation. The result of the simulation has to be compared to the measured pattern. If the accordance is rather poor, a variation is applied to the cluster atom positions again. For calculating the diffraction patterns two different simulation packages which each include multiple scattering were used. A detailed comparison of the XPD-simulation packages is presented in [47].

The MSPHD package   - full multiple scattering code for low energy photoelectron diffraction (**MSPHD**) is used for patterns at low kinetic energies, i.e. energies from 30 to 100 eV. The calculation of multiple scattering, including inelastic scattering effects is based on a matrix inversion method. The dimension of the matrix being calculated within the simulation package is related to the maximal angular momentum l, thus the matrix dimension depends on the kinetic energy of the photoelectrons. At large kinetic energies the computational effort, hence the computing time becomes rather large. [46]

The EDAC package   - electron diffraction in atomic clusters for core level photoelectron diffraction simulations (**EDAC**) package can be used for high, and also low kinetic energies with energies above 50 eV. Based on the multiple scattering theory, EDAC also takes inelastic scattering effects into account. The computational method is based on a modified recursion algorithm which reduces the computing time. [45]

The reliability-factor (**R-factor**) is a quantitative indicator for the accordance of the measured and simulated pattern. The R-factor is defined as:

$$R = \frac{\Sigma_{\Phi,\Theta}\big[\chi_{\text{sim}}(\Phi,\Theta) - \chi_{\text{exp}}(\Phi,\Theta)\big]^2}{\Sigma_{\Phi,\Theta}\Big[\chi_{\text{sim}}^2(\Phi,\Theta) + \chi_{\text{exp}}^2(\Phi,\Theta)\Big]}, \tag{2.19}$$

with the anisotropy functions $\chi_{\text{sim}}(\Phi,\Theta)$ and $\chi_{\text{exp}}(\Phi,\Theta)$ of simulated and experimental pattern, respectively. The anisotropy function has values between 0 and 1. While comparing each pixel of the measured to the simulated XPD pattern, $R = 0$ stands for a perfect correlation, $R = 1$ indicates no correlation and $R = 2$ means total anticorrelation. Various strucutre modifying techniques can be applied in order to minimize the R-factor, and one method has proven to be particularly effective in terms of computing time and also in preventing the convergence into local minima.

The genetic algorithm is used for the variation of parameters in the simulation process. It is designed to prevent the structure-search from running into a local minimum. The simulation process using a genetic algorithm is depicted schematically in figure 2.14. From a given start structure with defined set of emitter atoms, a new structure model is randomly generated within the previously defined variation limits. After the simulation of an XPD pattern, the experimental and simulated pattern are compared by the R-factor. The set of best structures is saved. If a set of best structures is already existing, and a comparison reveals better R-factors, the set is updated. If a prior defined termination criterion is fulfilled, a final structure is found. A termination criterion could be a good R-factor close to zero or a finishing of a defined number of cycles in the simulation. If the criterion is not yet fulfilled, further optimization of
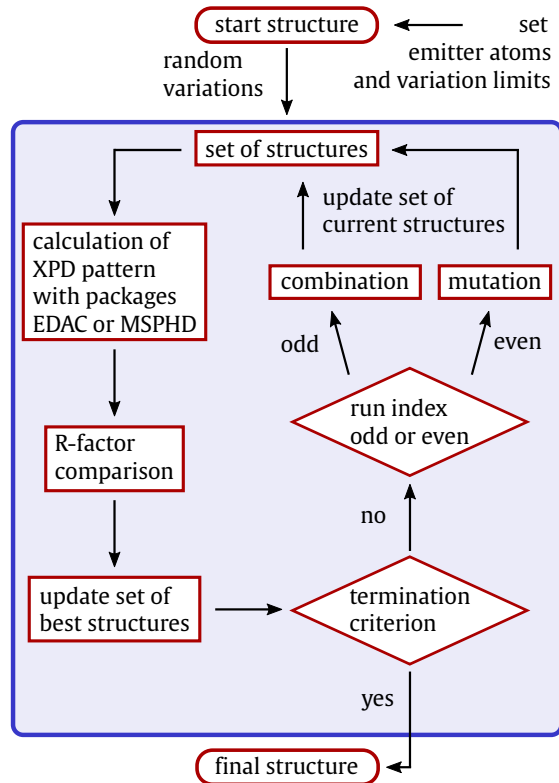

Figure 2.14 XPD simulation steps using a genetic algorithm. Image reproduced from [44].

the cluster is applied by combination and mutation of the structure models. The combination selects a structure with the best R-factor out of three randomly chosen clusters from both, the set of current and the set of best structures. In this manner a pair of parental genes are selected and a new structure is generated from their parameters. For a mutation, the parameters of the best structures are varied randomly within the defined limits, generating a new set of structures. The choice for a combination or mutation of the structures is chosen by the odd or even number of the run index, respectively. The new set of structures is set as start structures for the next simulation cycle. This method, based on biological evolution is designed to enable the achievement of a global minimum. [44, 48, 49]

2.5.3 Decomposition

In a sample with atoms in different chemical states or various structural environments, the recorded XPD pattern is the sum of the individual diffraction patterns. For the further analysis the XPD pattern can be decomposed in some cases, which means that the individual signals of the components are extracted from the measured pattern. For this purpose, each XPS spectrum is decomposed into its components, based on the fit to the high-resolution XPS spectrum. The separated data will then result in two or more individual decomposed XPD pattern. As the new patterns originate from the measured pattern, the decomposed patterns contain statistical noise as the original pattern, the processing steps as described in section 2.5.1 must be carried out again. Each of the decomposed pattern can be used within a simulation to identify the chemical origin. Therefore, a single atom or groups of atoms which have a similar local environment in the unit cell are set as emitter atoms. In order to find the appropriate allocation, several groups of atoms should be tested in the simulation.

2.6 LEED - low-energy electron diffraction

The low-energy electron diffraction (**LEED**) technique is a frequently used method in surface science for structure determination and characterization of the first layers of crystalline samples. To obtain structural information, low-energy electrons with 30 to 300 eV [50, 51] are accelerated onto the sample. The electron waves are scattered at the sample surface. Thus, the information depth of the technique depends on the IMFP of the electrons. If the sample proposes a well ordered periodic structure, a diffraction pattern with distinct spots can be obtained on a fluorescent screen.

Thereby, only elastically scattered electrons contribute to the pattern. Electrons that suffered an energy loss are rejected. According to de Broglie, who postulated the electron wave properties in 1924, the electron beam can be described as a plane wave with:

$$\lambda = \frac{h}{\sqrt{2mE_{\text{kin}}}}.$$

(2.20)

Here, h is the Planck constant, m the particle mass and E_{kin} the kinetic energy of the particle. Hence, for low energy electrons the wavelength is a few angstrom which is in the magnitude of the atomic distances of the investigated structure. One of the two main requirements for diffraction at the surface is energy conservation with $\left|\vec{k}_{\text{in}}\right| = \left|\vec{k}_{\text{out}}\right| = k$. The Laue condition states the relation of incident and reflected waves in the diffraction process at a crystal lattice. With $\vec{G}_{\text{hk}}$ as reciprocal lattice vector in two dimensions, a condition for constructive interference of the electron waves is:

$$\vec{k}_{\text{out}} = \vec{k}_{\text{in}} + \vec{G}_{\text{hk}}.$$

(2.21)

Here, $\vec{k}_{\text{in}}$ and $\vec{k}_{\text{out}}$ are the incident wave vector and the scattered wave vector, respectively. Furthermore, $\vec{G}_{\text{hk}}$ is a vector of the reciprocal lattice:

$$\vec{G}_{\text{hk}} = h\vec{a}^* + k\vec{b}^*,$$

(2.22)

with the primitive reciprocal translation vectors $\vec{a}^*$ and $\vec{b}^*$. For a better understanding of the formation of the LEED spots, the Laue condition can be illustrated by the Ewald sphere. [52]

The Ewald sphere is a model which helps visualizing the requirements for constructive interference for scattering processes at crystal lattices. Furthermore, it enables the derivation of the crystal structure from the diffraction reflections of the LEED-pattern. An illustration of the two-dimensional Ewald construction is shown in figure 2.15. Here the constructions of the sphere for two different energies at the same direction of incidence are displayed in blue and red. For the construction of the Ewald sphere, the points of a two-dimensional reciprocal lattice are represented by lattice rods perpendicular to the surface [50]. A sphere with radius k is constructed with its center around the origin of k_{in}. Each intersection point of the sphere with the lattice rods depicts a spot of constructive interference in the LEED-pattern. A variation of the wavelength has a direct impact on the wave vector k with $k = 2\pi/\lambda$.
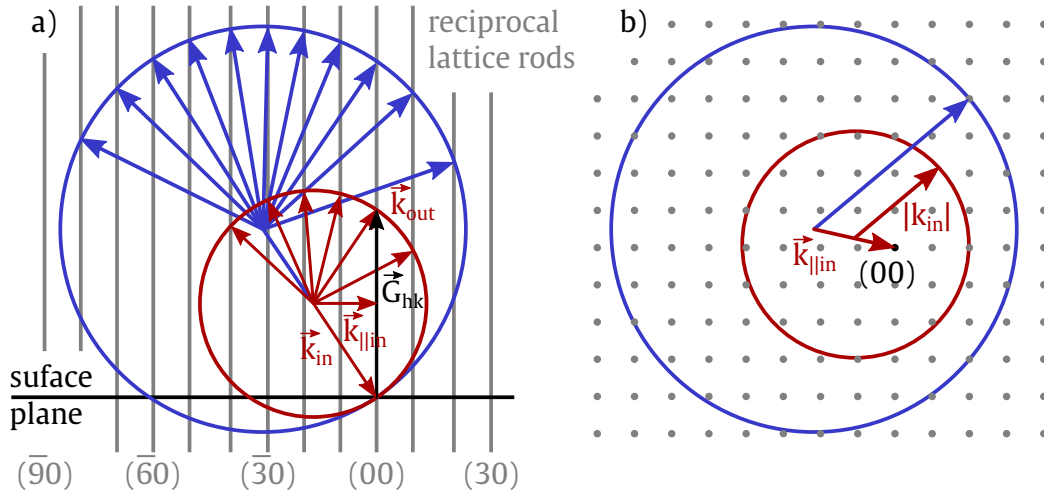
Figure 2.15 Illustration of the Ewald sphere a) parallel and b) perpendicular to the surface at two different energies, displayed in blue and red. Image reproduced from [50].

This leads to a scaling of the sphere as indicated in red in figure 2.15. In the LEED experiment, the (00)-rod is the direction of the scattered electron beam. In this case, the Ewald sphere is centered over the (00) spot, and the LEED-spots scale around the center of the pattern as the kinetic energy is varied. The analysis of the spot intensity throughout variation of the kinetic energy can give quantitative and qualitative information about the surface arrangement. The shape of the spots is an indicator for the quality of the sample surface. Imperfections in the crystallographic arrangement can lead to broadening, smearing, or weakening of the spots. Thus, sharp spots indicate a well-ordered surface [52]. The arrangement of the spots in the pattern can give information about the alignment, geometry and periodicity of the surface structure. Additionally, the pattern can feature another symmetry than expected just from the simple cluster atom arrangement, because of superposition of different domains. For the analysis of the LEED pattern, a given structural arrangement can be calculated using LEEDpat [53]. The experimental setup of the LEED system is found in section 3.3.3. [51, 54]

Chapter 3

Experimental setup

One requirement for surface science investigations of low-dimensional formations is the ability to prepare atomically clean surfaces. Under normal atmospheric conditions, a chemically clean surface gets contaminated through oxidation and adatoms or other impurity effects immediately. To avoid this process, all measurements are performed under ultra-high vacuum (**UHV**) conditions. Therefore, an experimental chamber with a base pressure of $p_{\mathrm{base}} < 1 \times 10^{-10}\,$mbar is used. This requirements are complied with the UHV-chamber at Beamline 11 at **D**ortmunder **EL**ek**T**ronen-Speicherring-**A**nlage (**DELTA**), which is described in the following section. After a description of the components for sample preparation, various analysis tools of the setup are characterized.

3.1 DELTA

The favored sources used for x-ray photoemission experiments are synchrotron radiation sources. Although the generation of x-rays requires more effort, this type of source has numerous advantages in application. Because of the broad energy spectrum and a selectable monochromatic wavelength, photoemission measurements at different specific energies are possible. Furthermore, synchrotron radiation sources feature a high brilliance and a high photon flux intensity. The synchrotron radiation used in this work is generated at the electron storage ring DELTA, which is operated with an electron beam energy of $1.5\,$GeV [55]. A schematic illustration is depicted in figure 3.1. The synchrotron light source consists of three main sections. In a linear accelerator (**LINAC**) [56] free electrons are generated from thermal emission. These electrons are pre-accelerated by a static electromagnetic field and then speed up to $80\,$MeV via a $3\,$GHz high-frequency. The second part is the booster-synchrotron
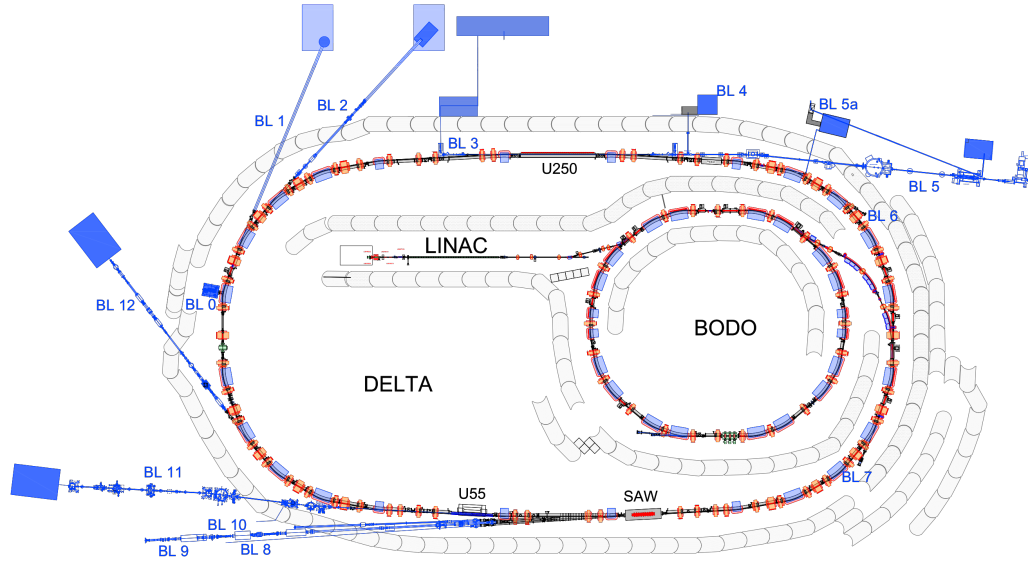
Figure 3.1 Schematic view of the Dortmunder electron storage ring DELTA. The setup includes a linear accelerator, a synchrotron, and a storage ring with 1.5 GeV. 12 beamlines provide synchrotron radiation for different experiments. Image reproduced from [55].

(**BoDo**). A 500 MHz cavity [57] boosts the energy of the electrons up to 1.5 GeV via a high frequency magnetic field. At this energy the electrons nearly reach the speed of light while the electron beam is held on a stable trajectory using magneto-optic components. With an circumference of 115.2 m the ring also consists of alternately arranged dipole and quadrupole magnets. The magnet systems are again used to bend the electron trajectory and to focus the electron beam. At different locations in the system several magnetic structures like wigglers and undulators offer hard and soft synchrotron radiation [58] with a high intensity and a broad energy range. For measurements in the soft x-ray range, beamline 11 (**BL11**) is connected to the undulator 55 (**U55**). The U55 consists of two rows of permanent magnets arranged in alternating orientation with a period length of 55 mm. As a bunch of electrons passes the undulator, it is deviated and forced on an oscillating trajectory. The deflection causes a change of the electrons momentum vector which results in the emission of bremsstrahlung, so-called synchrotron radiation. This linear polarized radiation provides high intensity and offers narrow energy bands. The gap of the undulator in combination with a plane-grating monochromator (**PGM**) in beamline 11 allows to

select monochromatic radiation in the range of $55 - 1500\,\text{eV}$. A focused beam spot at the sample's surface covers an area of approximately $70 \times 30\,\mu\text{m}$ [59, 60].

The UHV-setup for sample investigation which is attached to beamline 11 is described in the following section.

3.2 UHV-chamber

All measurements are conducted in the UHV-chamber at beamline 11. It consists of μ-metal for magnetic shielding of all components and is heatable to a temperature of $230\,^{\circ}\text{C}$ to avoid residual gas contamination. Since some components are temperature sensitive, bake-out temperatures up to $150\,^{\circ}\text{C}$ are used. The chamber is built in three main levels A-C. A multi-stage pumping system, located under the chamber provides a base pressure of $p_{\text{base}} \approx 1 \times 10^{-10}\,\text{mbar}$. The pumping system contains two scroll pumps as prepumps to two turbomolecular pumps for continuous operation. Additionally, an ion-getter pump and a titan-sublimation pump are attached to the UHV-system. The lowest level contains a sample transfer system, consisting of a load-lock which allows a relatively fast sample transfer. In level B different evaporators are available, and a quadrupole mass analyzer is positioned here. Level A, the upper plane, is the primary plane for sample analysis and preparation. A sputter gun and an evaporator can be used for surface preparation. The LEED system and a hemispherical spectrometer are attached for sample analysis. The top level provides a window flange for an optical pyrometer. A manipulator on top of the chamber enables a sample transfer between the different levels. All major components used in this work have been described previously [19, 44].

3.3 Analysis tools

For the analysis of the sample and monitoring of the preparation process, various components are attached to the chamber which are described below.

3.3.1 Pyrometer

Temperature monitoring is done with an pyrometer IMPAC IGA 6/23 Advanced from *LumaSense Technologies*. The temperature of a body can be measured via the intensity of emitted radiation. The power of the radiation can be described by the

Stefan-Boltzmann law and depends on the temperature T, the area A, and the specific emissivity ϵ of the body. The equation for the thermal irradiance E_e is the radiant flux per unit area:

$$E_\text{e} = P/A = \epsilon \sigma_\text{SB} T^4, \tag{3.1}$$

with σ_{SB} as Stefan-Boltzmann constant. The thermal radiation is focused onto a detector inside the pyrometer. Depending on the settings of the pyrometer, the temperature range is approximately $150\,°\text{C} \leq T \leq 1800\,°\text{C}$ with an uncertainty of 0.3%. The pyrometer operates with a peak intensity wavelength of $\lambda_\text{pyro} = 2.3\,\text{µm}$. The correct temperature measurement depends on the emissivity ϵ of the sample which can vary depending on the material and its surface properties like roughness and also on the temperature of the sample. Therefore, the emissivity can be adjusted in the pyrometer with settings of $\epsilon = 5\% - 100\%$ in steps of 0.1%. The pyrometer is mounted outside the chamber and measures through a glass window flange which also modifies the emissivity setting of the pyrometer.

3.3.2 Quartz crystal microbalance

The evaporation rate is initially checked with a QO 40A1 quartz crystal microbalance (**QCM**) from *PREVAC* with a $TM14$ thickness monitor as an oscillator. The evaporated material is deposited on a quartz crystal resonator. The initial frequency of the quartz crystal is $f_0 = 6\,\text{MHz}$. Under the condition that the deposited mass is much smaller than the mass of the crystal, the additional mass Δm changes the frequency f of the resonator according to [61]

$$\Delta f = -\frac{2 f_0^2}{\rho_\text{qc} v_\text{tr} A} \Delta m. \tag{3.2}$$

Here, ρ_qc is the density of the quartz crystal with the surface area A, and v_tr the transversal wave velocity. The deposition rate is estimated via

$$\Delta d = \frac{\Delta m}{\rho_\text{ads} A} = -\frac{\rho_\text{qc} v_\text{tr}}{\rho_\text{ads} 2 f_0^2} \Delta f, \tag{3.3}$$

with ρ_ads as density of the evaporated material [61]. The determination of the evaporation rate was recorded in an external chamber.

3.3.3 Low-energy electron diffraction system

For structural observation between the preparation steps a low-energy electron diffraction (**LEED**) system from *SPECS GmbH* [62] is attached to the chamber, schematically shown in figure 3.2. The theoretical background of this method is described in section 2.6. The construction of the LEED system is designed as reverse view or back view electron optics, where the diffraction pattern is observable through the window flange. The four grid system allows additional Auger electron spectroscopy measurements. Due to thermal emission, electrons are emitted from a thoria coated iridium
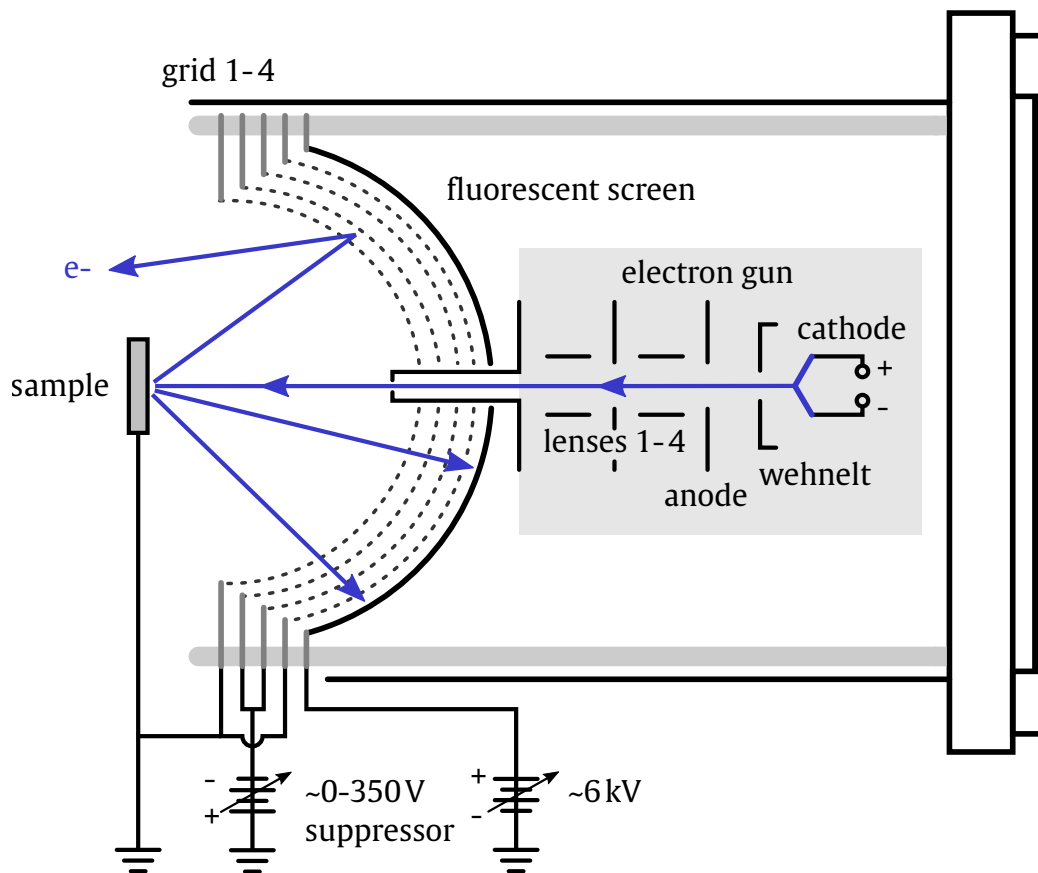
Figure 3.2 Schematic principle of a 4-grid low-energy electron diffraction system. The electron paths are indicated as blue lines. Image reproduced from [50].

hairpin cathode inside the electron gun. From the cathode the beam is accelerated by the positive potential of the anode. A Wehnelt cylinder is installed as potential shield between the cathode and the anode, focusing the beam. Further, the beam is collimated by four electrostatic lenses and accelerated onto the sample surface. The backscattered electrons are selected by four hemispheric, concentric grids that work as

retarding field analyzer and thus only let electrons pass that were scattered elastically. All other electrons, especially inelastically scattered electrons, are suppressed.

On a transparent glass screen coated with ITO[1] and P43[2] the k-space image of the measured surface is observed. Therefore, a high voltage of $5 - 7\,\mathrm{kV}$ is applied to the screen. As the compact electron gun covers only a small part of the pattern, the measurement is recorded via a camera behind the window flange. Analyzing the LEED pattern, the size and shape of the unit cell can be determined in relation to the substrate unit cell. A commonly used program for the simulation of LEED pattern is LEEDpat [53, 62].

3.3.4 Hemispherical analyzer

The beamline 11 end-station is equipped with a CLAM IV hemispherical analyzer (**HSA**) from *VG Microtech* for energy dependent photoelectron detection, as schematically shown in figure 3.3. The spectrometer consists of three main parts, a lens system, the hemispherical analyzer, and the detection unit. Initially, the emerging photoelectrons are focused via an electrostatic lens system and decelerated by an opposing electrical field. Adjusting the minimum energy of the entering electrons helps improving the energy resolution $\Delta E / E_{\mathrm{kin}}$ which depends on the kinetic energy. By tuning the deceleration, electrons of different kinetic energies can be measured. An entry slit selects electrons from a narrow angle of the source region. Here, a remaining angle dependence can lead to a spherical aberration in the detection area. The main part of the spectrometer, consisting of two concentric hemispheres, works like a spherical capacitor. The outer shell is at a negative potential while the inner shell is held at a positive potential. The radial electromagnetic field of the hemisphere allows focusing in two dimensions, resulting in a point being mapped back to a point [20]. The advantage of the hemispherical setup is that also electrons arriving transversely to the central circular trajectory reach the exit slit after passing through the analyzer. The charged particles are decelerated or accelerated, and thus sorted according to their kinetic energy. The median ray r_0 passing through the spectrometer can be adjusted to a certain pass-energy E_{pass}, where only electrons with $E_{\mathrm{kin}} = E_{\mathrm{pass}}$ are selected for the measurement. All other electrons with more or less kinetic energy are deflected onto the outer or inner hemispheres, respectively, and thus not measured. Though the electrons should be monoenergetic, the focus is not perfect. Therefore, an

---

[1]Indium tin oxide (ITO) is used as a transparent conductive oxide layer coating [63].

[2]P43 (Gd_2O_2S:Tb) is a cadmium free phosphor material [64].
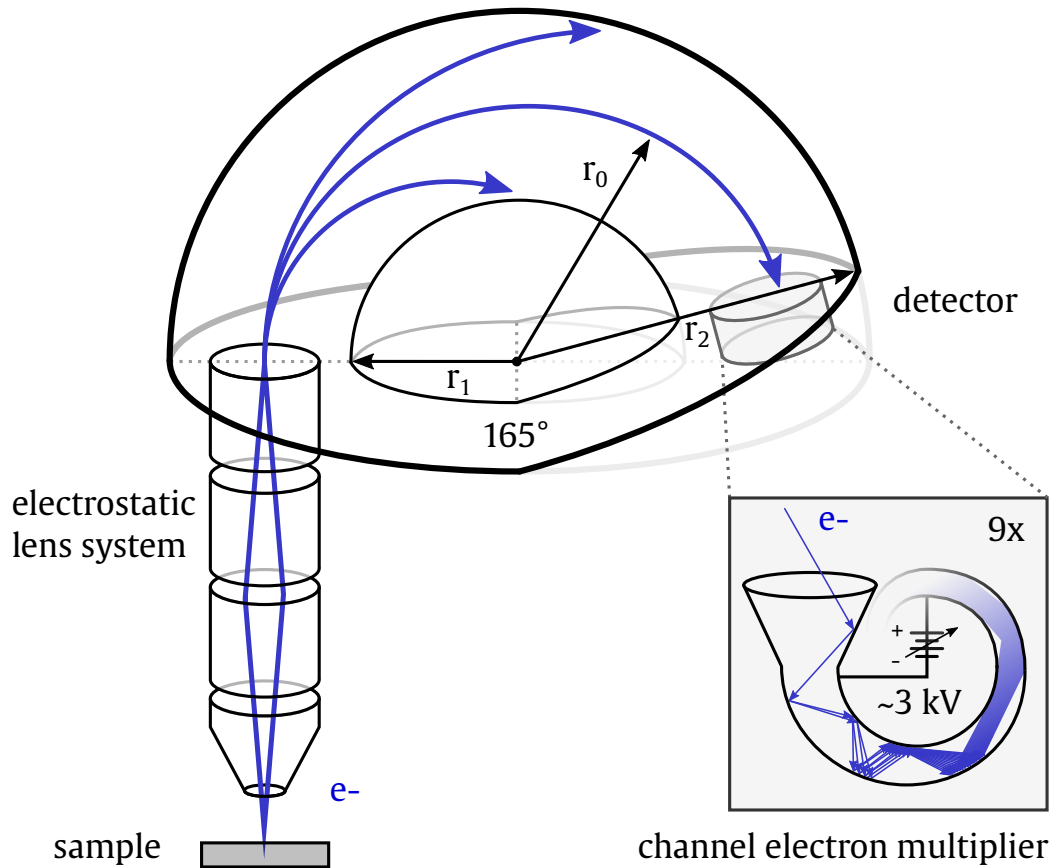
Figure 3.3 Illustration of the hemispherical analyzer (**HSA**) CLAM IV. The setup contains a focusing and retarding lens system, a hemispherical spectrometer and a 9 channel electron multiplier to amplify the signal by several orders of magnitude. Image reproduced from [65].

additional slit after the hemisphere enables a further reduction of the energy width, with the function of a band pass filter. The analyzer is not a full hemisphere, but possesses a sector angle of $\alpha = 165°$, with a mean radius of $r_0 = 150\,\text{mm}$, and an extend of $r_2 - r_1 = 74\,\text{mm}$. Subsequently, the signal of the electrons can be amplified and detected using a 9 channel electron multiplier (**CEM**). This type of continuous dynode multiplier, which is good for pulse counting, has the advantage of a small size and an increased sensitivity by using multiple CEMs. The 9 tubes, shown in the enclosed frame in figure 3.3 consist of a glass funnel coated with highly emissive, semi-conducting material. Incoming electrons are accelerated by a potential difference of $2 - 4\,\text{keV}$ and collide with the tube walls. Each collision causes a secondary emission of electrons, amplifying the signal up to a gain of $10^6 - 10^8$. The tubes are curved

to improve the number of collisions and prevent ionic feedback. Thus, the generation of ions amplifies the signal through further secondary emissions, its behavior is very sensitive to the amount of residual gas, thus to pressure variations. Therefore, ionization in the system should be avoided. A cone at the tube entrance improves the electron acceptance area. By tuning the energy range, the emerging electrons can be counted, depending on their kinetic energy. The resolution of a measured peak can be quantified by the FWHM. [22]

Chapter 4

Material background

This chapter deals with the characteristic properties and structural arrangements of the materials investigated in this work. Initially, the pure elements silicon, platinum, and gold are presented, followed by an introduction to the process of surface reconstruction at specific crystal orientations of the substrates silicon and gold. Finally, two silicon-based nanostructure systems are presented. In particular the systems of sub-monolayer platinum on a Si(100) surface and low-dimensional 2D arrangements of Si-atoms on a Au(110) substrate are characterized.

4.1 Silicon

Silicon is the second most abundant element on earth and the seventh most abundant element in the universe [66]. It appears commonly in the form of sand, quartz or rock crystals. It has been reported to appear in two allotropic phases. As crystal it shows a blue-gray metallic and brittle surface, but also occurs as brown powder. In the periodic table of elements it can be found in group 14 and crystallizes in diamond structure with a lattice constant of $a_{\mathrm{Si}} = 5.43\,\text{Å}$ [67] as shown in figure 4.1. As a metalloid silicon features metallic and also non-metallic properties. It is known to form alloys with other compounds, in combination with oxygen different forms of anions, called silicates, appear. Binary components with other more electropositive materials can lead to the formation of silicides. Silicon is able to donate or share its outer electrons with other atoms, thus it is highly reactive to other materials. At the surface, the top-most
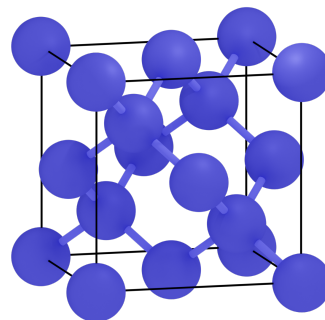
Figure 4.1 The unit cell of the atomic silicon diamond crystal structure.

atoms lack binding partners and free bonds are formed. The unsaturated bonds or dangling bonds can stabilize by saturation or via relaxation and reconstruction processes. To break the strong covalent bonds in the solid, high energy is necessary. Thus, silicon proposes a rather high melting point of $T_{\mathrm{Si|melt}} = 1414\,°\mathrm{C}$ and a boiling point of $T_{\mathrm{Si|boil}} = 3265\,°\mathrm{C}$. Especially, the electronic properties of silicon make it an outstanding material. As semiconductor, its resistivity falls with rising temperature which is contrary to metallic characteristics. This finding opened a door for a wide field of semiconductor applications, such as microelectronics, solar panels, but also in agriculture, cosmetics, and fine chemical industries [68–71].

4.2 Platinum

Platinum has a gray silvery white appearance. It is the 78th element of the periodic table and it is a transition metal of group 10. Pt crystallizes in a face-centered cubic (fcc) structure with a lattice distance of $a_{\mathrm{Pt}} = 3.92\,\text{Å}$ [67] as shown in figure 4.2.
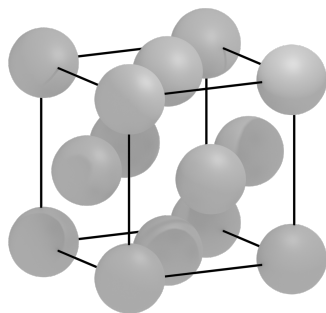
Figure 4.2 The unit cell of the atomic platinum face-centered cubic crystal structure.

Its very good resistance to corrosion, due to its low reactivity to most materials promote the application in fine jewelry and thus it belongs to the noble metals. Though it has already been used as decorative application more than 3000 years ago in ancient Egypt, its prestigiousness was not recognized until the 1800's. Moreover, it features a high temperature stability with a melting point of $T_{\mathrm{Pt|melt}} = 1768\,°\mathrm{C}$ and a boiling point of $T_{\mathrm{Pt|boil}} = 3825\,°\mathrm{C}$. Furthermore, it shows highly reactive behavior in combination with some compounds and has a prevalent application in catalytic converters. Beyond this, there are numerous of other fields of application, such as in medicine or in electronic devices, due to its corrosion resistance and stable electrical properties. Platinum is more ductile, but less malleable than gold.

4.3 Gold

Though there are elements that are more rare, and thus higher in price, gold is still perceived as the most precious material. Its bright, slightly reddish, yellow, metallic appearance made it already attractive more than 5000 years ago in ancient Egypt,

where it was used as material for ornaments and jewelry. As one of the least reactive materials it appears often in free elemental form and belongs to the noble metals. Gold is the 79th element of the periodic table and it is a transition metal of group 11.

Like platinum it arranges in a fcc crystal structure, shown in figure 4.3, with a lattice constant of $a_{\mathrm{Au}} = 4.06\,\text{Å}$ [67]. Together with silver and copper it belongs to the group of coinage metals [72]. Historically it was used as a payment method and it is still used today as monetary medium or investment. It finds main application in jewelry, medicine, and also for electronic devices. As excellent electrical conductor it is used to build capacitors and electrical connectors. Due to its high resistivity to corrosion, applications including gold last longer than for example applications with silver. Furthermore, gold provides a protection against electromagnetic radiation, thus a thin see-trough layer can be used for astronaut helmets. It has a melting point of $T_{\mathrm{Au|melt}} = 1064\,°\mathrm{C}$ and a boiling point of $T_{\mathrm{Au|boil}} = 2970\,°\mathrm{C}$.
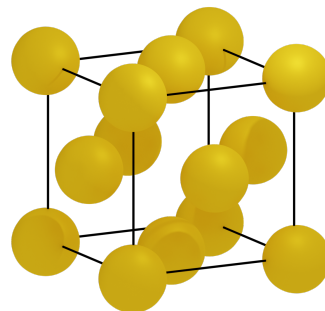
Figure 4.3 The unit cell of the atomic gold face-centered cubic crystal structure.

4.4 Crystal surface reconstruction

In a periodic crystal, the bulk-atoms are stacked in a similar arrangement as long as their surrounding forces stay the same. This periodicity can change at the crystal surface because of a broken translation invariance [73]. To find a stable energetic equilibrium the atom locations of the top-most or even a few layers can be changed. The surface frequently shows the tendency of relaxation with a slight reduction of the normal or lateral distance to the bulk-atoms. Depending on the material also reconstructions like two-dimensional rearrangements, a change in the symmetry, or more complex arrangements including large areas on the crystal are possible. Different arrangements can occur at a clean or under adsorbate coated surfaces. The surface reconstruction arrangements of the substrates used in this work, Si(100) and Au(110), are presented and described below.

4.4.1 Si(100) surface reconstruction

The ideal unreconstructed Si(100) surface features an atomic arrangement of perfect squares as schematically shown on the left side in figure 4.4. On the right, a side view of the structure is shown. The dark blue atoms 1 and 1' represent the top-most silicon layer. The increasing shading of the atom color indicates a deeper location under the surface. The arrangement of this ideal surface would show a twofold rotational symmetry. The direction of the rotation axis depends on the termination of the surface layer. As the top-most layer is removed, the new arrangement is similar to the former structure with a rotation of 90°. Therefore, measurements show a fourfold rotational symmetry due to overlapping domains. The lattice constant of $a_{Si} = 5.43\,\text{Å}$ [67] defines the distance in z or correspondingly in [100] direction between atoms 1 and 5.
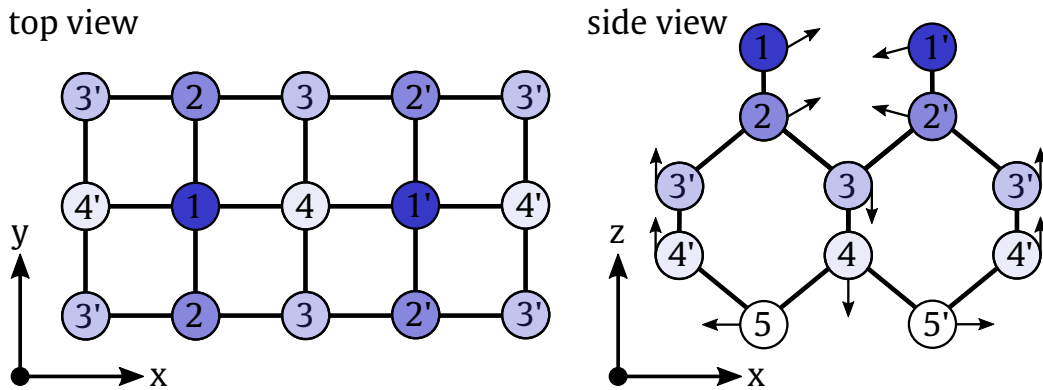
Figure 4.4 Structure model of an ideal Si(100) surface without reconstruction in top view and side view on the right and left side, respectively. The atomic layers are numbered descending from the surface with 1 as top-most layer. The directions of a surface translation due to a reconstruction are indicated by arrows. Image reproduced from [74].

The clean Si(100) surface is known to reconstruct in rows of silicon dimers [75–79]. Due to the substrate symmetry, these rows can be formed in the [010], and also in the [001] direction and usually appear in domains. The Si-atoms of the top-most layer exhibit a pair of dangling bonds. These free bonds without any adatoms at the surface, are unsaturated. A dimer formation of the top-most surface Si-atoms minimizes the free surface energy, and a surface reconstruction is obtained. The direction of translation due to the reconstructions are indicated with arrows in the side view of figure 4.4. The quantity of the atoms' displacements is reported in literature

as determined from various different theoretical and experimental approaches [74, 80, 81]. There exist different structure types depending on the symmetry and on the buckling of the dimers. A symmetric $p(2 \times 1)$ arrangement is often measured in STM studies, but in fact the structure consists of buckled dimers with a skew of about 18° [76] and a charge transfer from the lower to the upper atom [77]. The asymmetric arrangement of the dimers is energetically favorable as reported in calculations [81] and also in experimental results [79]. At room temperature the so-called flip-flop motion of the dimers enables a variable change of upper and lower atoms during STM measurements. For the clean Si(100) surface, different periodic asymmetric arrangements exist, depending on the tilt direction of neighboring dimer groups. In figure 4.5 different types of buckling dimer groups are displayed schematically. One
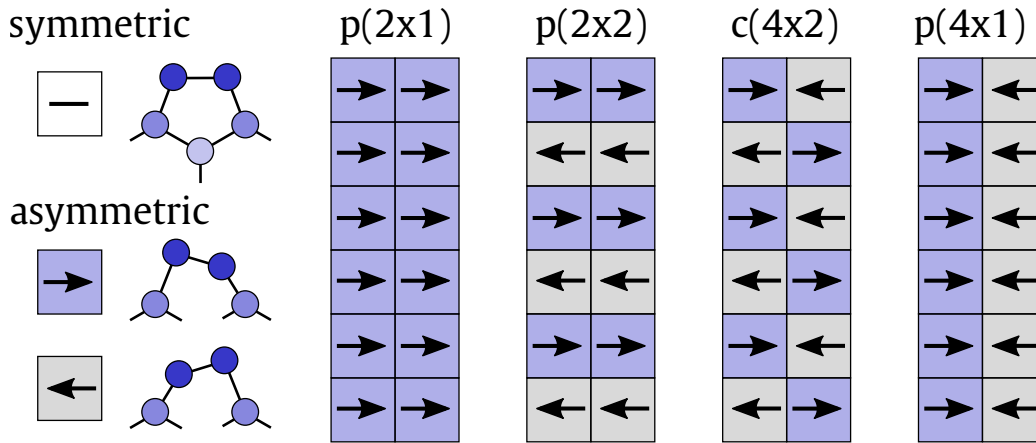
Figure 4.5 Different arrangements of buckled dimers at the clean and reconstructed Si(100) surface. Depending on the asymmetric direction of neighboring dimers, various periodicity phases can occur. Image reproduced from [75].

of the reconstructions is the $p(2 \times 1)$ buckled geometry, where the tilt of the dimers points in the same direction for every dimer group. At temperatures of approximately $T \leq -153\,°\mathrm{C}$ it has been reported that the symmetric structure stabilizes in two other arrangements. It either forms the $p(2 \times 2)$-reconstruction, with alternately buckled dimers, or a $c(4 \times 2)$ with alternately buckling in direction and perpendicular to the rows, respectively [77].

4.4.2 Au(110) surface reconstruction

Cutting a gold crystal in the [110] direction a rectangular unit cell with a ratio of the lattice vectors of $\vec{a'} : \vec{b'} = \sqrt{2}$ emerges. The absence of bonding partners

of the top-most atoms results in a reconstruction of the surface layers. The (110)

Au(110)-(1 x 1) top view

Au(110)-(2 x 1) top view

(1 x 1) side view
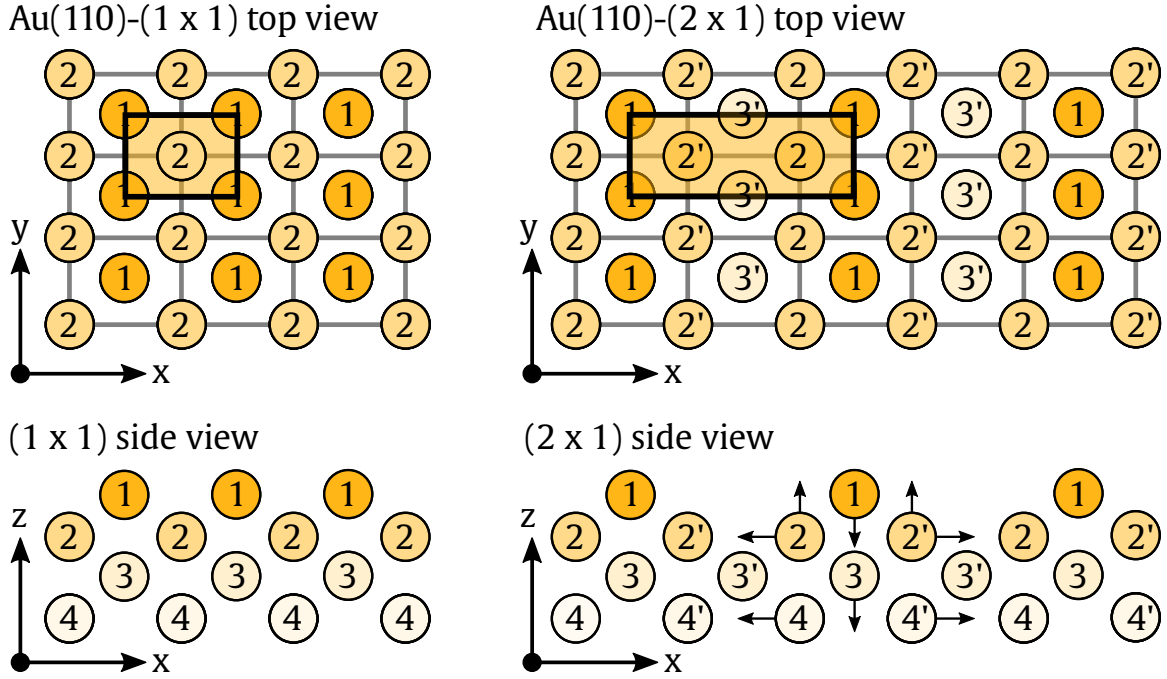
(2 x 1) side view

Figure 4.6 Structure model of a clean and reconstructed Au(110) surface. The (2×1) missing-row reconstruction is displayed in top view (top) and side view (bottom). Image reproduced from [82].

surface of the Au crystal is well known to reconstruct in a so-called missing-row reconstruction [73, 82, 83]. The broken bond symmetry forces the first atom layer to form a row-like structure, where entire rows of Au-atoms are missing. For the Au(110) surface the most stable structure is the (2×1)-reconstruction, where every second row is missing [73, 83]. Another possible, but less stable reconstruction is the (3×1)-reconstruction, where every third row is missing [83]. In the following the (2×1)-reconstruction is described in more detail. The basic arrangement of the unreconstructed Au(110) and the missing-row structure is displayed in figure 4.6 on the left and right side, respectively. The underlying grid spacing of the Au(110) surface in $[1\bar{1}0]$ direction is $a = 2.88\,\text{Å}$ and in the $[001]$ direction $\sqrt{2}a = 4.08\,\text{Å}$. The atoms' distance in $[110]$ direction is $a = 2.88\,\text{Å}$, resulting in a layer distance of $d = 1.44\,\text{Å}$. The reconstruction process causes variations in the atoms' location compared to the periodic bulk arrangement. Besides a compression of the first to the second layer distance a lateral translation is firmed, too.

4.5 Surface alloys and silicide systems

In many technological applications, metallic and semiconducting components are usually found in mixed form as a bi- or multi-system, since the combination of different materials can specifically improve their properties. In contrast to bulk alloys, surface alloys are solely formed in the first few surface layers. This provides the advantage of a fast and flexible preparation as well as the systematic investigation of the properties of mixed materials. For the formation of a surface alloy, one or more guest materials are deposited onto a homogeneous host material and annealed subsequently. Depending on the number of constituent materials and the alloying depth into the surface, the system can be classified in three types [8]. Type I describes a material A that is deposited onto a guest material B and thermally alloyed into the first atomic layer. Type II is defined as diffusion beneath the first layer. For type III, two materials A and B are mixed on a substrate C which features a larger melting point than A and B. In this work the focus is set to binary systems like type I and type II. Thus the preparation process requires conditions that favor the intermixing at the surface without diffusion of atoms into the bulk material. Here, the annealing temperature plays a decisive role.

4.6 Sub-monolayer platinum on Si(100)

The sub-monolayer deposition of Pt-atoms onto the Si(100) surface has been subject of multiple studies [5, 11–13, 84]. Depending on the coverage and annealing temperature, different silicide arrangements, as well as the formation of nano-wires have been reported.

Si-Pt silicide structures have been the subject of several investigations. The Pt/Si(100) surface shows different morphology states, depending on the amount of the deposited Pt and on the annealing temperature during the preparation. Figure 4.7 displays a phase diagram for the different structural arrangements as proposed by Itoh et al. [13]. At low coverage and at low annealing temperatures a (2×4) phase appears predominantly. At annealing temperatures between 550 and 1050 °C along with a coverage of 1/6 to 1/3 ML a combination of $c(4 \times 2)$ and $c(4 \times 6)$ have been reported for examinations by means of LEED measurements [11, 13]. Aditionally, a $c(4 \times 4)$ phase was found at a coverage of 0.1 ML after annealing above 900 °C [11]. For the stable ordered phase with the combination of $c(4 \times 2)$, and $c(4 \times 6)$ dif-

ferent structural arrangements have been proposed. STM measurements revealed that basically two different effects can cause the combination of the stable ordered mixed phases. The base of both systems are periodically arranged Pt-atoms adsorbed on the T3 site, as displayed in figure 4.8. Silicon and Pt-atoms are displayed in blue and gray color, respectively. The unit cells of the different phases are displayed with blue rhombuses. The T3 site, where the Pt-atom is located directly above a Si-atom of the third layer has been reported to be a energetically favorable position for low-dimensional platinum coverage on Si(100) [12]. The adsorption height of the platinum above the top-most silicon layer was found to be 0.5 Å [12].
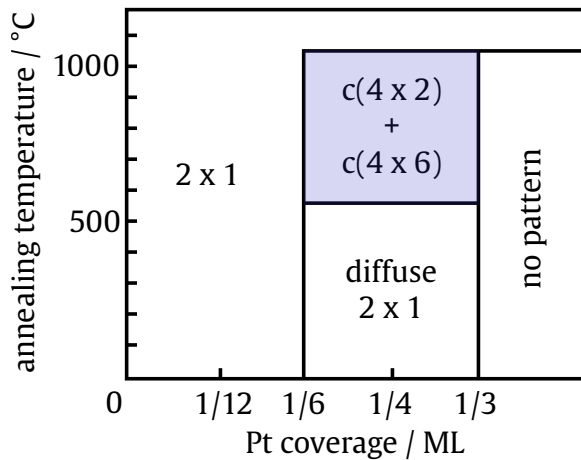
Figure 4.7 Surface phase diagram of the Pt/Si(001) system. Image reproduced from [13]

First, a structural combination of the basic $c(4 \times 2)$, and $c(4 \times 6)$ structures as suggested by several investigations [12, 13, 84] could be the origin of the mixed phase. The atomic arrangement of the $c(4 \times 2)$-structure includes the $c(4 \times 6)$ phase, which can be formed by removing two out of three atoms in the $c(4 \times 2)$ arrangement as displayed in figure 4.8 a). The obtained periodic silicide structure is likely a $c(4 \times 2)$-structure with systematically removed atoms.

Second, a system has been proposed where the basic $c(4 \times 2)$-phase based on Pt-atoms is complemented with a $c(4 \times 6)$ arrangement emerging from missing dimer groups at the surface. Different models based on a missing dimer structure have been proposed by Itoh et al. [85], and Ji et al. [11]. A structure with periodically omitted dimers ist displayed in figure 4.8 b). Depending on the surface morphology other phases occur at low platinum coverages on the Si(100) surface. The phases have been reported to form independent and also intermixed phases and domains [11, 12].

Si-Pt nano-wire structures have been reported to form on a Si(100) surface [14]. A larger length with more than 1 μm could be achieved with a vicinal Si(100)-2° off surface [5]. The unidirectional Pt_2Si nano-wires appear along the step edges favorable in the [011] direction beside a combination of $c(4 \times 6)$ and $c(4 \times 2)$-structured Si-Pt silicide on the terraces. The local density of states indicates a metallic character in

a) combination of c(4x2) and c(4x6) b) missing dimers c(4x2) and c(4x6)

Figure 4.8 Surface structure models of sub-monolayer platinum on a Si(100) substrate. Platinum adsorption sites for a mixed $c(4 \times 2)$ and $c(4 \times 6)$ phase. Structure model a) was proposed by Choi et al. [12] and a system with missing silicon dimers by Ji et al. [11] is displayed in b).

the direction of the nano-wires [14]. A high annealing temperature up to 1200 °C of the system revealed a disaggregation of the nano-wires and the silicide due to diffusion of platinum atoms into the bulk and defect formation on the surface.

4.7 Sub-monolayer silicon on Au(110)

Gold in combination with silicon was the first compound where a metallic glass was established. Using a rapid quenching method, the amorphous liquid phase was solidified from the molten phase [86]. Its properties are similar to those of ceramic glasses, and silicates. The discovery laid the foundation for the estimation criterion of crystallization. The combination of Au and Si can also be fused to a continuous composition. The phase diagram of the binary gold-silicon system reveals an eutectic temperature of $T = (363 \pm 3)$°C, which is comparatively low. As small amounts of silicon are deposited on a gold surface, different structural arrangements were found. Silicide formation and low-dimensional silicon arrangements on a gold surface have also been reported for Au(100) [87], and Au(111) [88], respectively. Sub-monolayer deposition of Si-atoms onto the reconstructed Au(110) surface can lead to different stable ordered phases at the surface. At a coverage of <0.1 ML silicon at the Au(110) surface, a low-dimensional silicon surface alloy begins to form as reported by Enriquez

et al. [7]. Reaching a coverage of 0.3 ML, silicon nano-wires are likely to appear at the surface [6]. Both systems are described in the following.

The Au-Si alloy structure has been reported by Enriquez et al. [7] first. The investigation was performed using LEED, STM, and DFT calculations, and proposed a first structural suggestion. The LEED pattern revealed two overlapping domains that can be described by the matrices $\left(\begin{smallmatrix} 10 & -2 \\ -1 & 4 \end{smallmatrix} \right)$ and $\left(\begin{smallmatrix} 10 & 2 \\ 1 & 4 \end{smallmatrix} \right)$. Further STM and DFT calculations lead to the structure which is displayed in figure 4.9 a) in top, and side view. Yellow spheres depict Au-atoms and blue spheres represent Si-atoms. The base of this calculation is a flat, unreconstructed Au(110) surface with 38 Au-atoms in the top-most layer. From the STM images it can be assumed that the structural arrangement is flat with only a very small buckling or roughness. The STM measurements indicate that due to symmetry considerations an even number of Si-atoms is reasonable.

The unit cell, displayed in black, contains 12 Si-atoms of which eight are arranged in a hollow-position above the top-most Au layer. The remaining 4 Si-atoms changed position with one of the top-most Au-atoms, respectively. Now the Au-atoms are rearranged to a top position 0.1 nm above the Si-atoms. The shifted Si-atoms are indicated by blue circles with a white dot in the top view. The shift of the Si-atoms in [110]-direction is displayed in detail in the side view, with a red line indicating a cut through the cluster. For the structure a thermal stability up to 500 °C was proposed.

The Au-Si nano-ribbon structure has been reported for a silicon coverage above 0.3 ML. There have been chemical and structural studies of the system [6, 17].The combination of structural and chemical investigation via LEED, XPS, and XPD revealed a hexagonal double-row arrangement as shown in figure 4.9 [19]. The Si-atoms coordinate in a two-dimensional arrangement embedded in the [$\bar{1}$10] missing-row structure of the Au(110) surface.
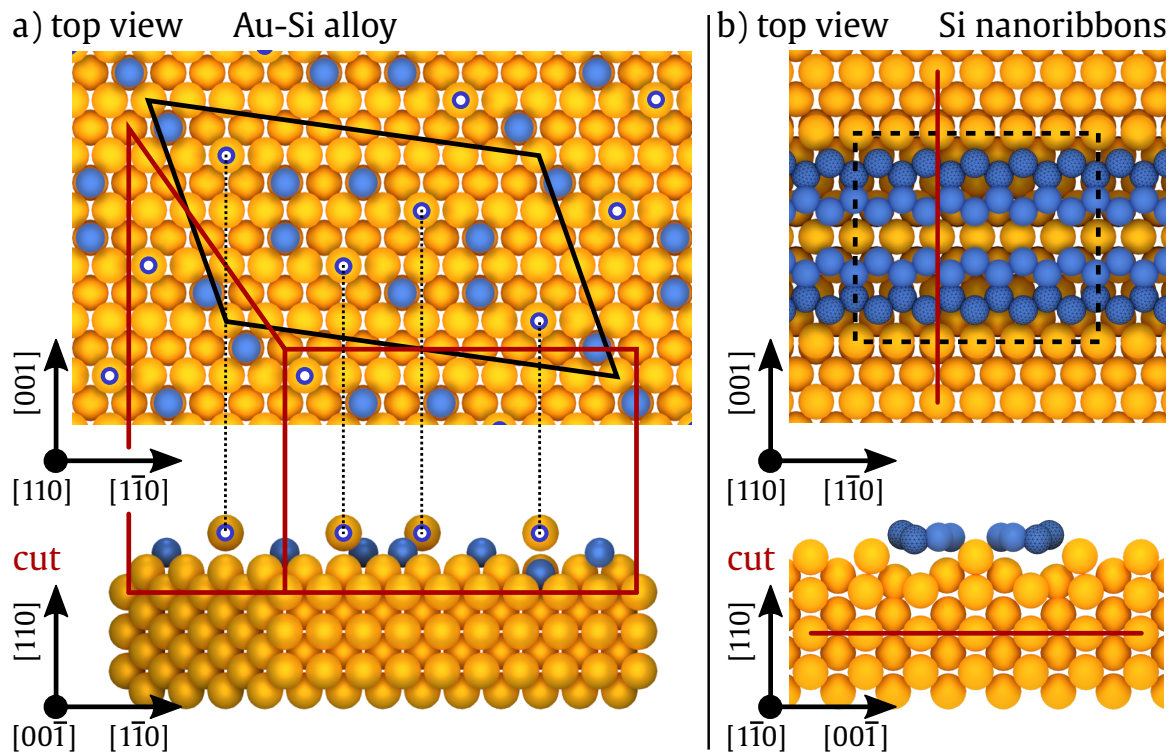
Figure 4.9 Surface structure models of sub-monolayer silicon on a Au(110) substrate. a) displays a low-dimensional Au-Si alloy, as proposed by Enriquez et al. [7]. Image reproduced from [89]. b) shows a structure model of Si nano-ribbons, as proposed by Roese et al. [17]. Image reproduced from [19].

Chapter 5

Si-Pt silicide

This chapter presents a detailed structural and chemical analysis of a sub-monolayer platinum film on a Si(100) sample. In the first section, the clean and reconstructed surface of a Si(100) sample is characterized via LEED, XPS, and XPD investigations. Subsequently, the deposition of 1/6 ML platinum and the formation of a Si-Pt silicide is monitored and analyzed by the previously mentioned measurements. Different reported structure models are analyzed and a new structural arrangement of a Si-Pt silicide phase is introduced. The results of each method are presented and compared to literature.

5.1 Reconstructed Si(100) surface

A rectangular Si(100) wafer with dimensions of 5.9×7.9 mm is used as sample. In a first wet-chemical cleaning process the sample is rinsed to remove potential organic contamination at the surface. Therefore, the wafer is cleaned in an ultra-sonic bath in acetone and afterwards in isopropyl alcohol for 10 min. For surface preparation in UHV, the wafer is mounted onto the sample holder. The silicon surface is highly reactive to hydrogen, oxygen and other adatoms. For the removal of those impurities and the preparation of a pristine reconstructed Si(100) surface, several preparation steps are performed, which are described in the following. To prevent the deposition of foreign atoms on the reactive surface, it is crucial to keep the maximum pressure below $p \leq 2 \times 10^{-9}$ mbar during the whole preparation process. In consideration of this, the sample is degased in alternating cycles of heating and cooling.
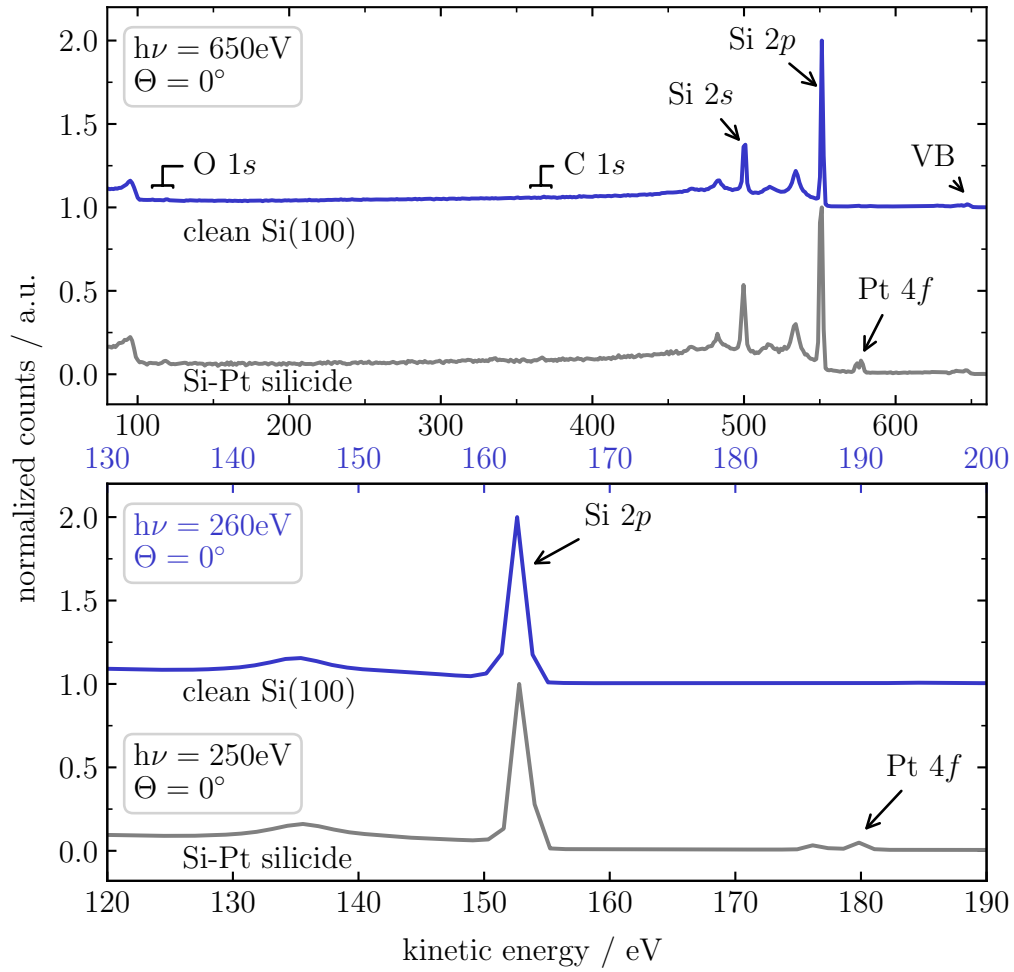
Figure 5.1 Photoelectron survey spectra of clean Si(100) and sub-monolayer Pt on Si(100), displayed in blue and gray, respectively. In the bottom panel, the Si-spectrum is shifted by 10 eV in order to align the Si $2p$-signal at $E_{\mathrm{kin}} = 153\,\mathrm{eV}$.

Direct heating was used for sample preparation. Since silicon is a semiconductor, a certain breakdown voltage has to be reached to make the sample conductive. Therefore, the voltage is increased slowly so that the base pressure is not affected by a sudden pressure surge. For a temperature of $T = 900\,°\mathrm{C}$ at the sample set-up a maximum voltage of $U = 5.8\,\mathrm{V}$ and a current of $I = 6.0\,\mathrm{A}$ were applied. The temperature of the silicon sample is monitored by a pyrometer. For the silicon sample the emissivity value is set to $\epsilon = 65\%$ which corresponds to an emissivity of clean silicon at temperature of $T = 1000\,°\mathrm{C}$ [90]. Initially the sample has to be heated for $t \approx 3\,\mathrm{h}$ at a temperature of $T \leq 800\,°\mathrm{C}$ to degas the whole sample holder. For the formation of a stable ordered reconstruction of the surface, the sample is heated up to a temperature of $T \approx 1000\,°\mathrm{C}$ and subsequently cooled carefully with approximately $2\,°\mathrm{C/s}$. The slow cooling facilitates the arrangement of atoms in a stable ordered phase. As the pressure of the vacuum chamber can be rather high during the heating process and is likely to rise above $p \approx 2 \times 10^{-9}\,\mathrm{mbar}$, repeated flashing of the sample with subsequent pressure stabilization pauses is recommended. The cleanness and reconstruction of the sample is checked using XPS and LEED. In figure 5.1, the XPS survey spectrum of the clean Si(100) surface is displayed in blue, recorded at a photon energies of $h\nu = 650\,\mathrm{eV}$ and $h\nu = 260\,\mathrm{eV}$ at an angle of $\Theta = 0°$ in the top and bottom panel, respectively. The Si $2s$ and Si $2p$-peaks appear at kinetic energies of $E_{\mathrm{kin,Si}\ 2s} = 500\,\mathrm{eV}$ [91] and $E_{\mathrm{kin,Si}\ 2p} = 550\,\mathrm{eV}$ [91], respectively. Each peak is accompanied by energy loss signals, which appear shifted towards smaller kinetic energies. No adatom signals, such as O $1s$ ($E_{\mathrm{kin,O}\ 1s} = 117\,\mathrm{eV}$ [92]) and C $1s$ ($E_{\mathrm{kin,C}\ 1s} = 366\,\mathrm{eV}$ [93]) are observable which indicates a clean surface.

5.1.1 LEED measurements of the reconstructed Si(100) surface

LEED patterns are recorded to confirm the cleanness and reconstruction of the silicon surface. Figure 5.2 a) depicts the LEED pattern of the clean and reconstructed Si(100) surface at a kinetic energy of $E_{\mathrm{kin}} = 60\,\mathrm{eV}$. The arrangement of the spots indicates two well-ordered, symmetric domains at the surface. The blue circles mark the main spots of the bulk signal, while the red circles correspond to the superposition spots of the reconstruction. For comparison a LEEDpat [53] calculation of the (1×1) LEED pattern for the unreconstructed Si(100) is shown in figure 5.2 c). The corresponding real space image is depicted in figure 5.2 e). The unit cell is marked by the vectors $\vec{a}$ and $\vec{b}$ (r-space) with the reciprocal vectors $\vec{a}^*$ and $\vec{b}^*$ (k-space). In figure 5.2 the real space simulation of the bulk structure reveals a quadratic arrangement. In the

a) E_{kin}=60 eV

b) p(2x1) $\begin{pmatrix} 2 & 0 \\ 0 & 1 \end{pmatrix}$
k-space

c) c(1x1) $\begin{pmatrix} 1 & 0 \\ 0 & 1 \end{pmatrix}$
k-space

$\vec{a}'^*$

$\vec{b}'^*$

$\vec{a}^*$

$\vec{b}^*$

d) r-space

e) r-space

$\vec{a}'$

$\vec{b}'$

$\vec{a}$

$\vec{b}$

[001]

[010]
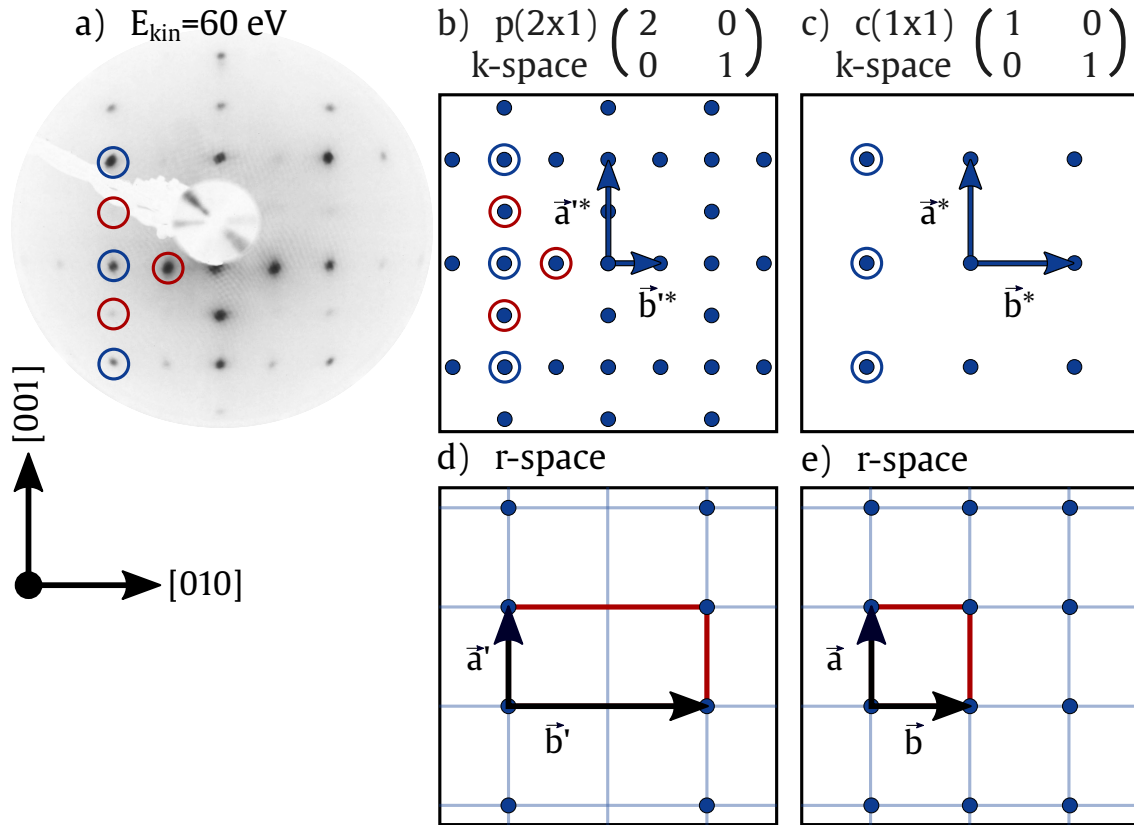
Figure 5.2 a) experimental LEED pattern of reconstructed Si(100), recorded at a kinetic energy of $E_{kin} = 60\,\text{eV}$ showing a p(2 × 1)-structure. LEEDpat [53] simulations of c) the p(1 × 1) Si(100) bulk structure and b) the p(2 × 1)-surface reconstruction structure. e) and d) display the real space images corresponding to the simulated LEED pattern above, respectively. The blue circles mark the bulk spots and the red circles the additional spots of the p(2 × 1)-surface.

reconstructed real space LEEDpat simulation in figure 5.2 b) a p(2×1) arrangement of the spots in the reciprocal space (k-space) is observable. The corresponding simulated real space (r-space) image in figure 5.2 d) reveals the periodicity and size of the unit cell. This originates from single atoms at the surface, rearranging in pairs along the [010], and also in the [001] direction. The dimers coexist in different domains at the surface, thus the additional LEED spots marked with red circles appear in both directions, leading to a new unit cell with r-space vectors $\vec{a}'$ and $\vec{b}'$, which correspond to the reciprocal vectors $\vec{a}'^*$ and $\vec{b}'^*$. The ratio of the vectors is $\vec{a}'/\vec{b}' = \vec{b}'^*/\vec{a}'^* = 1/2$, which relates to the theoretical predicted structure of the p(2 × 1) arrangement

as shown in figure 4.5. Subsequently, to the LEED analysis, XPS measurements are conducted for further chemical analysis.

5.1.2 XPS measurements of the reconstructed Si(100) surface

High-resolution core-level XPS spectra of the reconstructed Si(100) surface are taken as displayed in figure 5.3. The measurements are recorded with a pass-energy of $E_{\text{pass}} = 5.85\,\text{eV}$ and an increment of $\Delta E_{\text{inc}} = 0.123\,\text{eV}$. The spectra of the Si $2p$-signal are recorded at a photon energy of $h\nu = 260\,\text{eV}$ and at emission angles of $\Theta = 60°$ and $\Theta = 0°$ in top and bottom panel, respectively. The corresponding fit parameters are presented in table 5.1. The background and lineshape of the components are fitted by applying the curve fit program UNIFIT [32]. A Shirley-background is used in combination with a Voigt-lineshape as discussed in section 2.3.2. The envelope of the spectra reveals a spin-orbit coupling of $\Delta E_{\text{soc}} = 0.61\,\text{eV}$ between the Si $2p_{1/2}$ ($E_{\text{kin}} = 156.21\,\text{eV}$) and the Si $2p_{3/2}$ ($E_{\text{kin}} = 156.82\,\text{eV}$) component. This is in excellent accordance with literature [19, 94]. Moreover, the spectra reveal 4 components that are chemically shifted. The component Si_{bulk} displayed in dark blue corresponds to the bulk signal as it decreases under a surface sensitive angle of $\Theta = 60°$ from $85\%|_{\Theta=0°}$ to $78\%|_{\Theta=60°}$. The surface component $\text{Si}_{\text{surface}}$ is displayed in light blue with a chemical shift of $\Delta E_{\text{chem}} = 0.35\,\text{eV}$ to the bulk component. The components are of symmetric shape with an asymmetry parameter of $\alpha = 0$ which has been reported in literature [19]. The FWHM at a surface sensitive angle is approximately $0.55\,\text{eV}$ for all four components. Due to a long measuring time oxidation at the surface occurs, depicted in red and light red with a shift of $0.95\,\text{eV}$ and $1.77\,\text{eV}$ for Si^{1+} and Si^{2+}, respectively. Because of the rather fast oxidation of the surface, the sample is cleaned again before the XPD measurement. The cleanness is checked again via a survey spectrum and LEED measurements. To analyze the structural arrangement in detail, XPD patterns are recorded.

Table 5.1 XPS fit parameters of Si $2p$ high-resolution spectra of the clean Si(100) surface at a photon energy of $h\nu = 260\,\text{eV}$. Each spectrum shows a spin-orbit coupling of $\Delta E_{\text{soc}} = 0.6\,\text{eV}$.

$\Theta/°$	Comp.	E_{kin}/eV	FWHM/eV	α	$A_{\text{rel}}/\%$
	Si bulk	156.79	0.55	0.0	78
60	Si surface	157.14	0.56	0.0	15
	Si^{1+}	157.74	0.56	0.0	4
	Si^{2+}	158.56	0.54	0.0	3
	Si bulk	156.82	0.47	0.0	85
0	Si surface	157.17	0.46	0.0	11
	Si^{1+}	157.77	0.44	0.0	3
	Si^{2+}	158.59	0.43	0.0	1
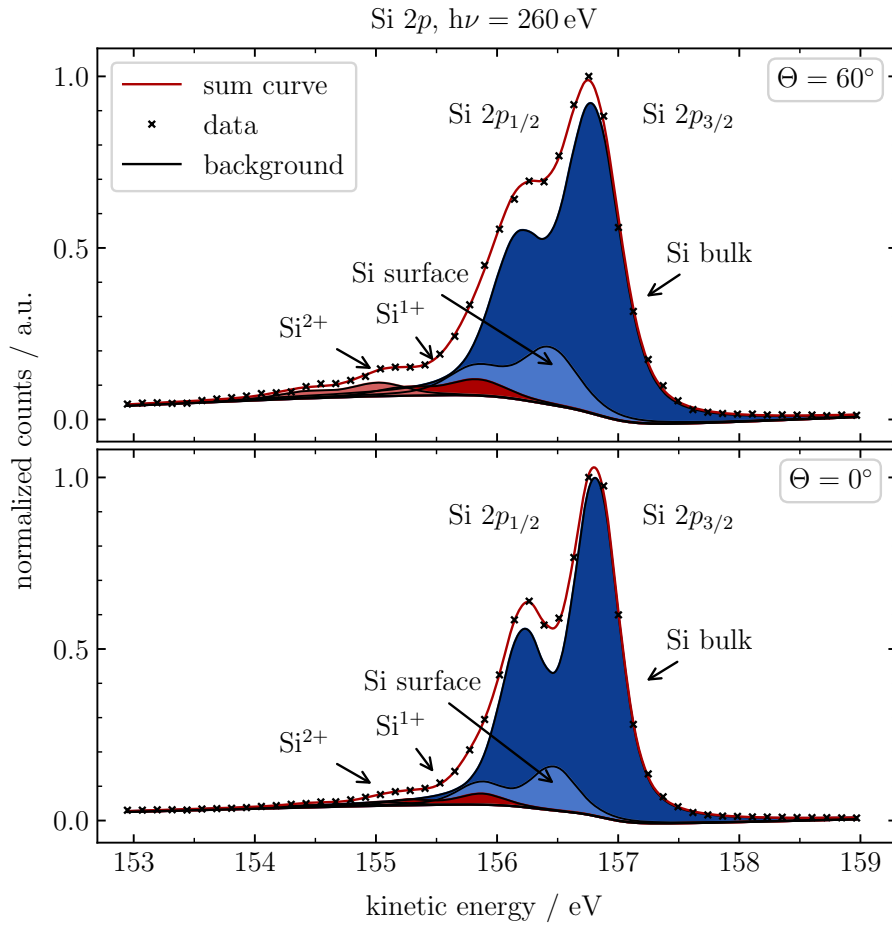
Figure 5.3 High-resolution core-level XPS spectra of the Si $2p$-signal, measured at a clean and reconstructed Si(100) surface. The spectra are recorded at a photon energy of h$\nu = 260\,\mathrm{eV}$ at emission angles of $\Theta = 60°$ and $\Theta = 0°$ in the top and the bottom panel, respectively.

5.1.3 XPD pattern of the reconstructed Si(100) surface

An XPD pattern of the Si $2p$-signal is taken at an energy of h$\nu = 140\,\mathrm{eV}$, a pass-energy of $E_{\mathrm{pass}} = 58.55\,\mathrm{eV}$, and an increment of $\Delta E_{\mathrm{inc}} = 0.615\,\mathrm{eV}$ as displayed in figure 5.4. The polar angle ranges from $20° \leq \Theta \leq 80°$ with increments of $\Delta\Theta = 2°$. A full azimuthal scan is performed with $\Phi = 360°$ and steps of $\Delta\Phi = 1.8°$. A background removal, a step correction, and also the application of an anisotropy function and a Gaussian-filter are applied, as described in section 2.5. As the structure of the p(2×1)-reconstructed Si(100) indicates, the pattern shows a fourfold rotational and also mirror symmetry at $\Phi = 0°$ and $\Phi = 90°$. To remove statistical uncertainties,

a) Si 2p experiment
$E_{kin} = 36.4\,\text{eV}$

b) Si 2p simulation
$E_{kin} = 36.4\,\text{eV}$

R = 0.07
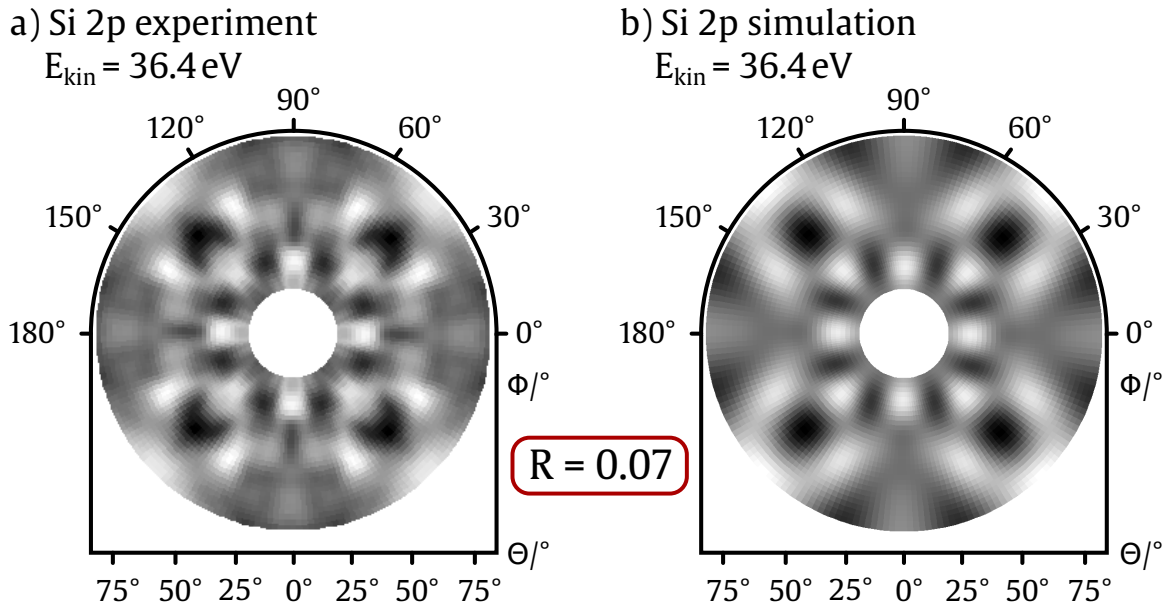
Figure 5.4 Photoelectron diffraction pattern of a clean and reconstructed Si(100) surface. The experimental Si $2p$ pattern, recorded at a photon energy of $h\nu = 140\,\text{eV}$ is shown in a). The XPD pattern is simulated with the EDAC package and shown in b).

these symmetries are applied to the experimental pattern. To reduce the influence of a possible oxide component to the pattern, which can occur during long data acquisition times, only the signal of the main silicon peak is used in the further data analysis.

For a simulation of the clean silicon surface, a cluster model of the Si(100) surface is generated, based on the p(2×1)-phase as reported in literature [81]. 28 atoms from the first 6 layers of the unit cell are set as emitter atoms with an emitter radius of $7.0\,\text{Å}$. The simulation is performed using the EDAC package. Additionally, different dimer arrangements of the reconstruction models in section 4.4.1 are tested. A scaling of the whole cluster of $\pm 0.1\%$ in all three dimensions, and also variations of several groups and also single atoms in the first layers of the unit cell of $0.3\,\text{Å}$ in x-, y-, and z-direction are applied to the simulation. The best simulated pattern is shown in figure 5.4 b) with an R-factor of R = 0.07. The patterns in figure 5.5 a) and b) show the same symmetry, all main features are reproduced, and differences occur predominantly in fine details. The structure model is displayed in figure 5.5 with blue spheres as Si-atoms. The surface-atoms are reconstructed in the p(2×1) alignment with dimer buckling in only one direction.

top view   topmost Si layer
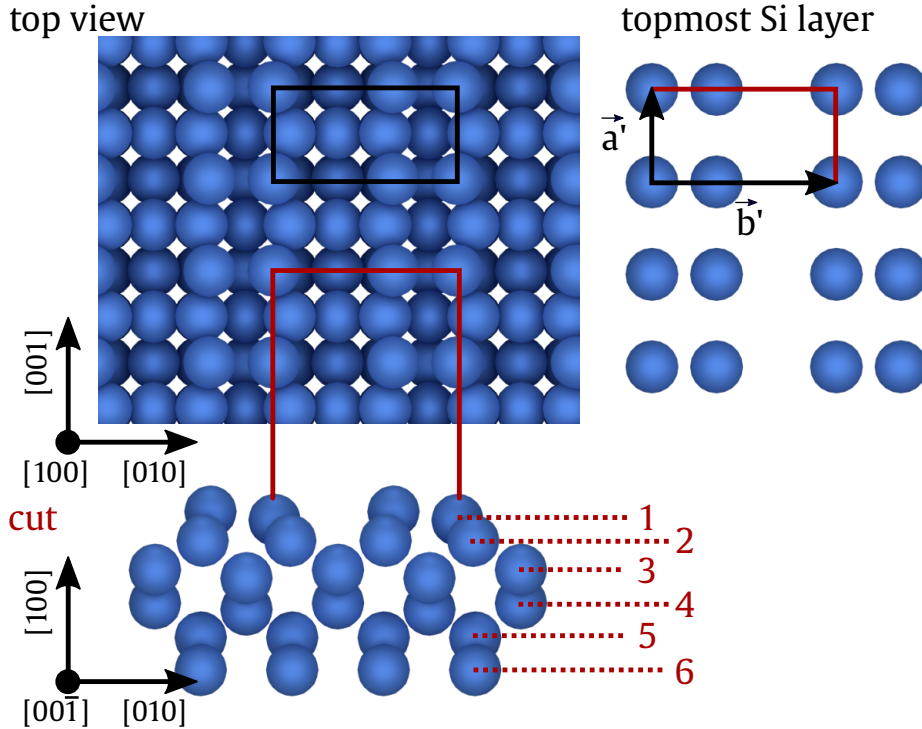
Figure 5.5 Best simulated structure model of a clean and reconstructed Si(100) surface in top and side view with an additional top-most layer view.

5.2 Preparation of Si-Pt silicide

In this section, the preparation process and also the chemical and structural analysis of the Si-Pt silicide are presented. After the cleaning and reconstruction process of the Si(100) sample, a sub-monolayer platinum is evaporated onto the surface by means of electron beam evaporation. As the cleaned silicon surface is highly reactive to atom deposition, the maximum pressure must be kept below 2×10^{-9} mbar during the process. Furthermore, the evaporated platinum must be free from impurities. Therefore, the platinum rod has to be degased before the cleaning process of the silicon surface. As platinum tends to form different phases depending on the stoichiometry and the annealing temperature [13], the silicide formation is observed via XPS and LEED between the preparation steps. The growth rate of 2 Å/h at $P \approx 18$ W was previously estimated via a quartz crystal microbalance as displayed in figure 5.6. A platinum coverage of approximately 1 Å was accomplished after 30 min of evaporation. This corresponds to a thickness of $1/6$ ML[1]. For the formation of Si-Pt silicide, the

---

[1]A monolayer is defined by one layer of silicon at the Si(100) surface.
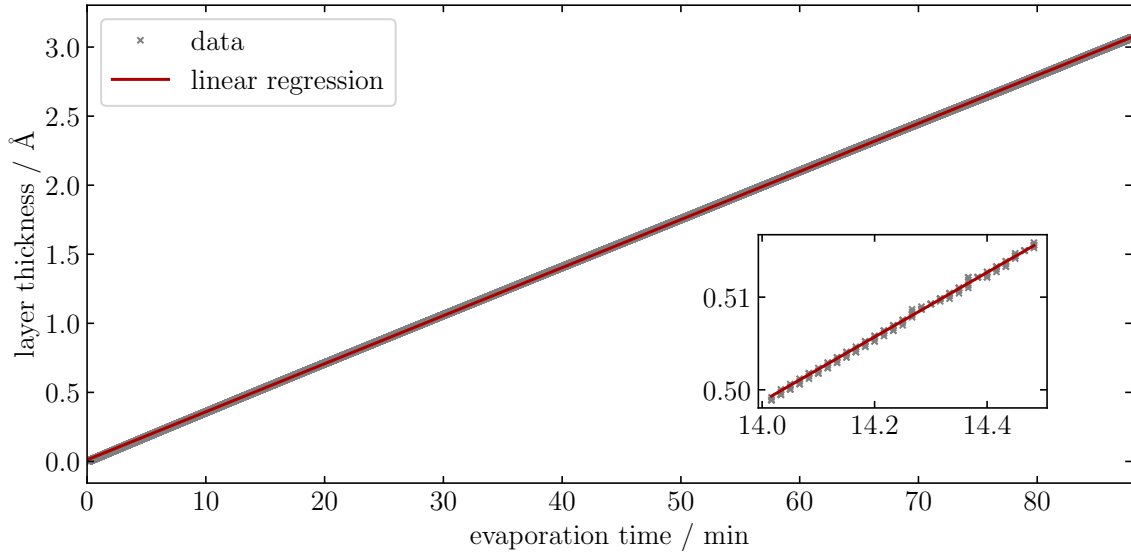
Figure 5.6 Quartz crystal microbalance measurement of platinum evaporation at a power of $P_{Si} \approx 18\,W$ and a deposition rate of $2\,\text{Å/h}$.

sample has to be annealed at temperatures higher than $970\,°C$ [95]. Therefore, the sample is flashed to approximately $1000\,°C$. After the annealing process an XPS survey spectrum is taken, displayed in gray color in figure 5.1. The Pt $4f$-signal arises with a kinetic energy of $E_{kin,Pt\ 4f_{7/2}} = 577\,eV$ [96]. The Pt-signal is also split into two components due to spin-orbit coupling. Furthermore, no additional contamination signals of C $1s$ or O $1s$ arise next to the platinum and silicon signals which indicates a deposited film free of contaminations. After the preparation, the sample is further analyzed via LEED, XPS, and XPD.

5.3 LEED measurements of Si-Pt silicide

LEED measurements of the Si-Pt silicide are performed after the preparation and analyzed using LEEDpat [53]. Figure 5.7 displays a LEED-pattern recorded at a kinetic energy of $E_{kin} = 60\,eV$, revealing a fourfold symmetry and also a mirror symmetry at the [001] and the [010] direction. Additional patterns at different kinetic energies are presented in the appendix in figure A.1. Beside the characteristic p(1×1)-spots of the silicon bulk substructure displayed in blue color, new spots of the Si-Pt silicide are detected, shown in gray. The pattern reveals a combination of a c(4 × 2)-phase and a c(4 × 6) structure as reported by literature [5, 12, 13, 84].
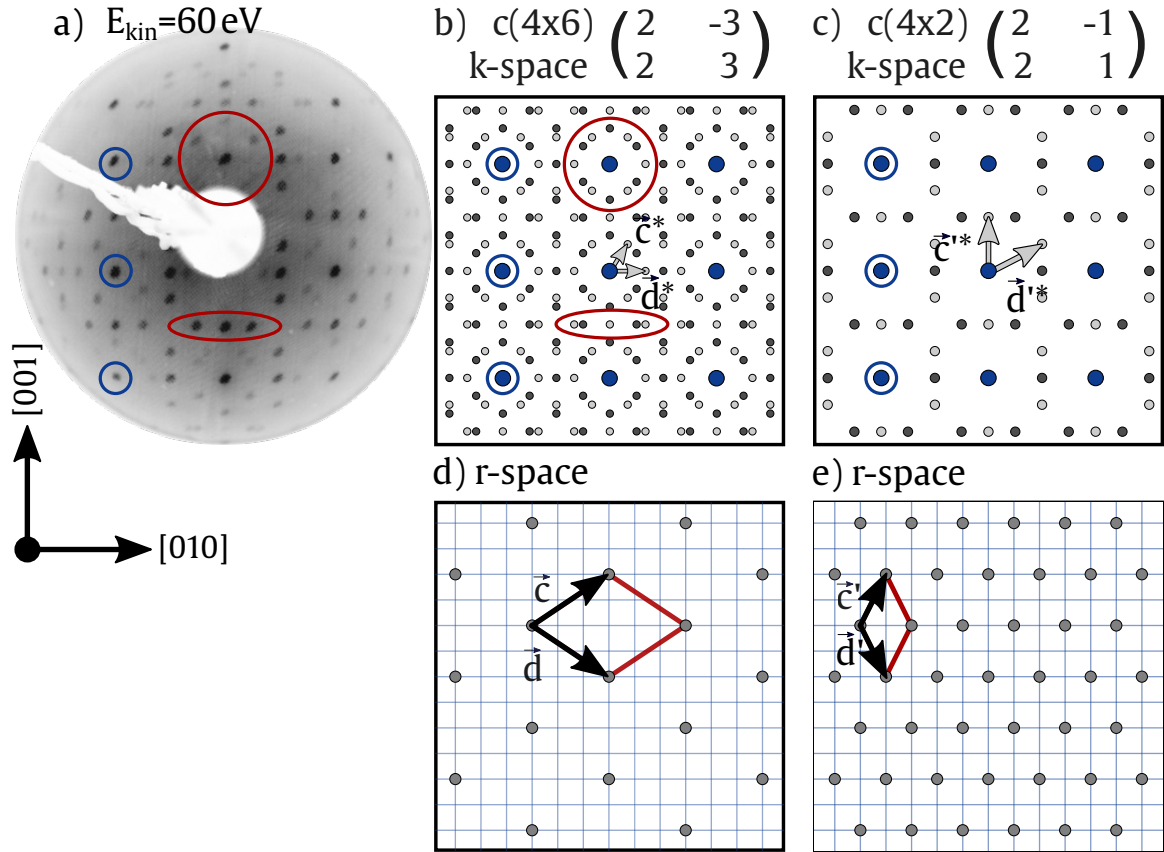
Figure 5.7 a) LEED pattern of Si-Pt, recorded at a kinetic energy of $E_{\text{kin}} = 60\,\text{eV}$ shows a combination of a $c(4 \times 6)$ and a $c(4 \times 2)$-structure. LEEDpat [53] simulations of b) the $c(4\times6)$ and c) the $c(4\times2)$-structure. d) and e) display the real space images corresponding to the simulated LEED pattern above, respectively.

The unit cells of the individual structures can be described by the matrices $\left(\begin{smallmatrix} 2 & -1 \\ 2 & 1 \end{smallmatrix} \right)$ and $\left(\begin{smallmatrix} 2 & -3 \\ 2 & 3 \end{smallmatrix} \right)$. For the $c(4 \times 6)$ and $c(4 \times 2)$-phases the corresponding LEEDpat [53] simulations are shown in figures 5.7 b) and 5.7 c) with their corresponding r-space structures in figures 5.7 d) and 5.7 e), respectively. Here, the blue spots mark the $\text{Si}(100)$ (1×1) bulk structure LEED spots. The small spots in light and dark gray depict the LEED spots of the two appearing domains. The domains are rotated by $90°$. This could be explained by the crystal geometry of the $\text{Si}(100)$ surface. In figures 5.7 d) and 5.7 e) the corresponding r-space structures are shown, where the blue grid in the background represents the silicon bulk structure. Some features occurring in the LEED pattern and in the simulation to the $c(4 \times 6)$ structure are marked by red circles. The new unit cell vectors $\vec{c}$ and $\vec{d}$ to the $c(4 \times 6)$ are shown in figure 5.7 d), with the reciprocal vectors $\vec{c}^*$ and $\vec{d}^*$. The $c(4 \times 2)$-structure is

represented by the r-space vectors $\vec{c}'$ and $\vec{d}'$ with $\vec{c}'^*$, and $\vec{d}'^*$ as reciprocal vectors. For chemical investigations, XPS measurements are performed and displayed in the following section.

5.4 XPS measurements of Si-Pt silicide

After preparation of the Si-Pt silicide high-resolution core-level XPS spectra of the Si $2p$ and Pt $4f$-signals are recorded at hν = 250 eV. The pass-energy is set to $E_{\text{pass}} = 5.85$ eV and the increment is $\Delta E_{\text{inc}} = 0.061$ eV. The theoretical peak ratio of the Si $2p$ doublet is 1:2, as displayed in the experimental data. A careful fit of the spectrum reveals a ratio of the Si $2p_{1/2}$ to the Si $2p_{3/2}$-signal of 0.52. The corresponding fit parameters are displayed in table 5.2. In the spectrum, two chemically shifted components are identified, associated to the Si bulk signal in dark blue and to the SiPt component displayed in light blue. They are separated by $\Delta E_{\text{chem}} = 0.34$ eV. The spectra of the Si $2p$-signal are shown in figure 5.8. The spectra are recorded at emission angles of $\Theta = 60°$ in the top panel, and $\Theta = 0°$ in the bottom panel. The fit has been performed applying UNIFIT 2020 procedure [32] using a Shirley-background and a Voigt-line pro-

Table 5.2 XPS fit parameters of Si $2p$ high-resolution spectra of the Si-Pt silicide surface at a photon energy of hν = 250 eV. Each spectrum shows a spin-orbit coupling of $\Delta E_{\text{soc}} = 0.61$ eV. The dark blue component corresponds to the Si bulk component and the light blue signal originates from a Si-Pt bond.

$\Theta/°$	Comp.	E_{kin}/eV	FWHM/eV	α	A_{rel}/%
60	Si bulk	147.10	0.59	0.0	60
	SiPt	146.76	0.61	0.0	40
0	Si bulk	147.09	0.49	0.0	69
	SiPt	146.75	0.53	0.0	31

file, as described in section 2.3.2. This reveals a split into a Si $2p_{1/2}$ and a Si $2p_{3/2}$ component due to spin-orbit coupling with a separation of $\Delta E_{\text{soc}} = 0.61$ eV which has been reported in literature [94].
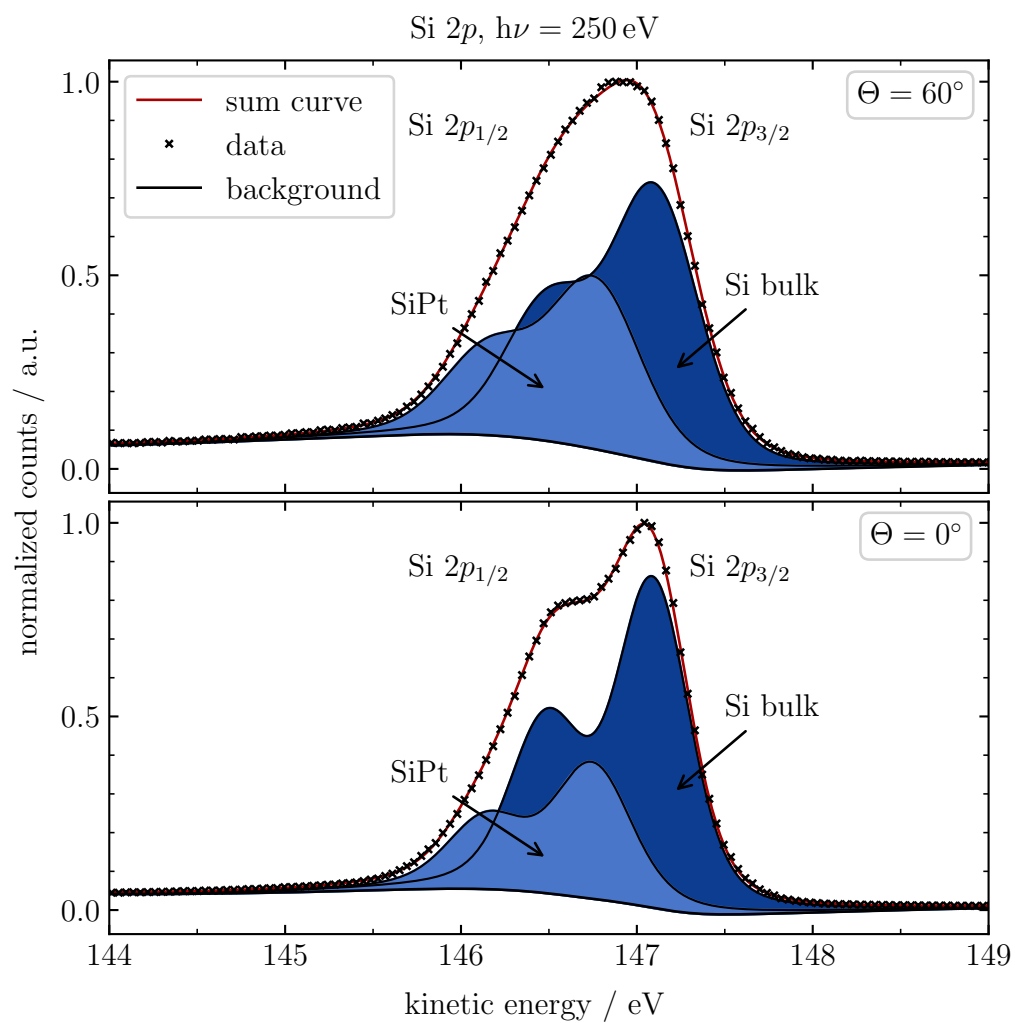
Figure 5.8 Photoelectron high-resolution spectra of Si 2p recorded at a photon energy of h$\nu = 250\,\text{eV}$. The Si 2p core-level spectra are shown at emission angles of $\Theta = 60°$ (top) and $\Theta = 0°$ (bottom).

Both reveal a symmetric peak shape with an asymmetry parameter of $\alpha = 0$ which is in good accordance to literature [94]. The FWHM of the SiPt component is slightly larger. This is likely the effect of slightly variant bonding states of the Si-atoms to the platinum, which results in several overlapping Lorentzian profiles. The dark blue component rises under $\Theta = 0°$ which rises from a relative area of $60\%|_{\Theta=60°}$ to $69\%|_{\Theta=0°}$, indicating that it corresponds to the silicon bulk-atoms. As the component SiPt rises under a surface sensitive angle, it is likely that mainly atoms close to the surface can be assigned to this bond. The silicon surface component in the spectrum of the clean Si(100) surface featured a shift of $0.34\,\mathrm{eV}$ relative to the bulk component. Thus, the origin of SiPt is probably a Si-Pt bond at the surface which is in good accordance to literature [5].

The Pt $4f$ XPS signal, recorded at $h\nu = 250\,\mathrm{eV}$, is shown in figure 5.9. The spectra at emission angles of $\Theta = 60°$ and $\Theta = 0°$ are displayed in top and bottom panel, respectively. The corresponding fit parameters are shown in table 5.3.

Due to the metallic character of the platinum a Tougaard-background is adapted to the data as described in section 2.3.1 [38]. The line profile of the components is modeled with a convolution of Doniach-Sunjic and Gaussian-profiles using one doublet component. The spectrum shows the Pt $4f_{5/2}$ and Pt $4f_{7/2}$-signals at $E_\mathrm{kin} = 170.22\,\mathrm{eV}$ and $E_\mathrm{kin} = 173.54\,\mathrm{eV}$, respectively. The components are separated due to spin-orbit coupling

Table 5.3 XPS fit parameters of Pt $4f$ high-resolution spectra of the Si-Pt silicide at a photon energy of $h\nu = 250\,\mathrm{eV}$. Each spectrum shows a spin-orbit split couple separated by $\Delta E_\mathrm{soc} = 3.32\,\mathrm{eV}$.

$\Theta/°$	Comp.	$E_\mathrm{kin}/\mathrm{eV}$	FWHM/eV	α	$A_\mathrm{rel}/\%$
60	Pt	173.54	0.99	0.03	100
0	Pt	173.54	0.99	0.03	100

by $\Delta E_\mathrm{soc} = 3.32\,\mathrm{eV}$, as reported in literature [97]. The FWHM of the Pt $4f$ component is $0.99\,\mathrm{eV}$ and the asymmetry parameter $\alpha = 0.03$. As the platinum signal shows only one doublet component, it confirms the conclusion that all Pt-atoms are located at the surface and in similar chemical environments. Moreover, there are no additional components present that could indicate a diffusion of platinum into silicon or surface defects as reported by Lim et al. [5]. Neither oxidation components appear, which indicates a saturation of the dangling bonds due to the adsorption of platinum. For further structural analysis of the Si-Pt silicide, XPD measurements are performed.

Figure 5.9 Photoelectron high-resolution spectra of the Pt $4f$-signal of Pt on a Si(100) surface recorded at a photon energy of h$\nu = 250\,\text{eV}$. The Pt $4f$ core-level spectra were taken at emission angles of $\Theta = 60°$ and $\Theta = 0°$.

5.5 XPD measurements of Si-Pt silicide

XPD measurements of the Si-Pt silicide are performed with a photon energy of $h\nu = 250\,\text{eV}$ for the Si $2p$ and also for the Pt $4f$-signal. Both patterns are recorded with a pass-energy of $E_{\text{pass}} = 58.55\,\text{eV}$, an increment of $\Delta E_{\text{inc}} = 0.615\,\text{eV}$, and at a polar angle range of $20° \leq \Theta \leq 80°$, and a full $\Phi = 360°$ scan with increments of $\Delta\Phi = 1.8°$ and $\Delta\Theta = 2°$. As displayed in figures 5.10 a) and 5.10 c), both signals reveal a fourfold rotational symmetry and also a mirror symmetry along the $\Phi = 0°$ and $\Phi = 90°$ direction. After background subtraction, a step removal, and the application of an anisotropy function the symmetry operations are applied to the patterns. Further, to remove statistical fluctuations, a Gaussian-blur with radius 2 is used. The resulting XPD patterns for Si $2p$ and Pt $4f$ are displayed in figure 5.10 a) and figure 5.10 c), respectively. To approximate the surface structure of the Si-Pt silicide, both patterns are simulated using different cluster models. To find a proper structural model, former measurements are taken into account. The LEEDpat simulations in figure 5.7 propose two related models composed of overlapping domains, and a combination of a $c(4 \times 6)$ and a $c(4 \times 2)$-phase. Finally, the best resulting structure of the Si-Pt silicide is likely a combination of both surface arrangements.

The real space atomic arrangement of the $c(4 \times 2)$-phase includes the atomic structure of the $c(4 \times 6)$ phase arrangement as shown in figure 4.8. Therefore, a combination of the two systems is achieved by systematically removing single Pt-atoms in the real space structure of the $c(4 \times 2)$-phase, which is done in the following. Multiple structural arrangements of Pt-atoms on the silicon surface are generated, displayed in figure 5.11. Here, the blue and gray circles denote the Si and Pt-atoms, respectively. The blue grid beneath the structures displays the substrate structure. The removed Pt-atoms are indicated by empty circles in the figure. The resulting unitcells are highlighted in blue color. Additionally, different adsorption sites of the Pt-atoms are tested including T3 and T4, which have been reported to be favorable adsorption sites of metals on the Si(100) surface [12, 98]. Here, the adsorbed atoms are positioned in a top position above an atom of the third and fourth layer, respectively. Variations in x-, y-, and z-direction of 0.15 Å and a scaling of the whole cluster of $\pm 0.5\%$ in all three dimensions are applied to each cluster. For the Pt $4f$ simulation, all Pt-atoms within the unit cell are set as emitter atoms, while for the Si $2p$ simulation 120 Si-atoms in the unit cell within the first 5 layers beneath the surface are considered as emitter atoms.
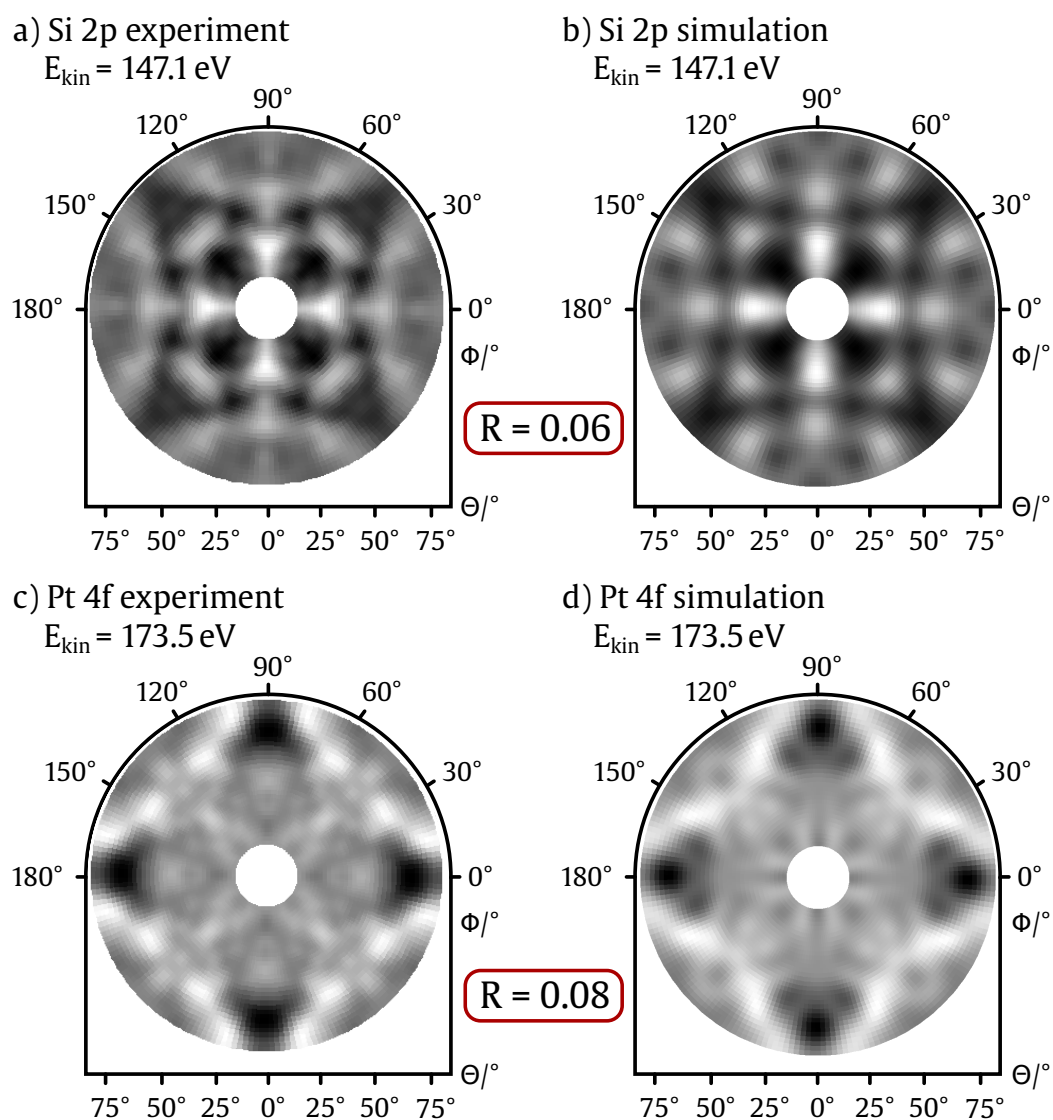
Figure 5.10 Photoelectron diffraction patterns of Si $2p$ and Pt $4f$ recorded at a photon energy of h$\nu = 250$ eV displayed in a) and c), respectively. The corresponding simulated XPD patterns are shown in b) and d). The simulations are performed using the EDAC package.
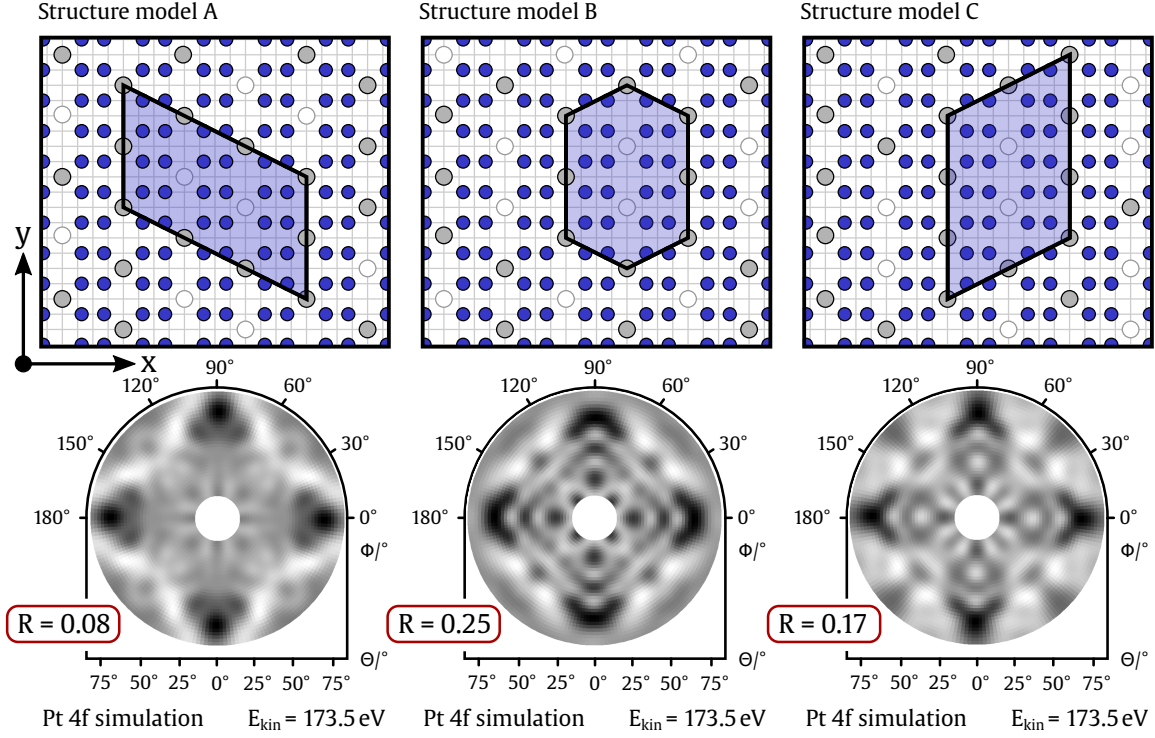
Figure 5.11 XPD simulations of different structural Pt/Si(100) arrangements based on a combination of a c(4 × 6) and a c(4 × 2)-phase. A systematically removal of single Pt-atoms generated new periodic structures. The corresponding XPD patterns are displayed in the bottom panel.

Emitter radii of $r_{Si} = 9.77\,\text{Å}$ and $r_{Pt} = 6.48\,\text{Å}$ are applied for Si $2p$ and Pt $4f$, respectively. This corresponds to 1.5×IMFP as required for simulations via EDAC. A simulation for each cluster and for both Si $2p$ and Pt $4f$ patterns is performed. For the simulation, different proposed structure models [11–13], modifications, and combinations of these are tested. The simulations of platinum and silicon are performed in an iterative procedure, converging to the best fitting model. As shown in figure 5.11 for the Pt $4f$ simulation, structure models B and C reveal R-factors of R = 0.25 and R = 0.17, respectively. This indicates that the structure models are close to the expected measurement, but not sufficiently good. The simulations for B and C to the Si $2p$-signal reveal better results. For both the Pt and the Si simulation structure model A reveals the best result. The best simulated pattern for Si $2p$ is shown in figure 5.10 b) with an R-factor of R = 0.06. In figure 5.10 d) the Pt $4f$ pattern with an R-factor of R = 0.08 reveals an excellent agreement between measurement and simulation. The corresponding structure model is depicted in detail in figure 5.12 in top and side-view. Additionally, an image of the segregated top-most silicon layer

with the adsorbed Pt-atoms is shown on the right side of the image. The blue spheres depict the silicon substrate atoms, while the Pt-atoms are shown in gray. The unit cell of the structure is described by the matrix $\left(\begin{smallmatrix} 3 & -6 \\ 4 & 0 \end{smallmatrix}\right)$. Its extend is determined to be 23.07 Å and 15.36 Å in the [010], and [001] direction, respectively. The structure is visualized with 10 Pt-atoms arranged in a rhombus structure, as shown in figures 5.11 and 5.12. The periodicity of the structure indicates that one unit cell contains 4 Pt and 24 Si-atoms in the top-most layer. This corresponds to a stoichiometry of Pt/Si = 1/6. Each Pt-atom is located in a valley bridge position in a T3 adsorption state. Thus, it is located directly above an atom of the third layer, which has been reported to be the favorable state for platinum adsorption on Si(001) [12]. The Pt-atoms are located 0.58 Å above the top-most layer of Si-atoms which agrees very well with values reported in literature [12]. The Pt-atoms reveal a buckling of approximately 0.55 Å which is in excellent accordance to literature [12]. This could be an indicator for the enlarged FWHM of the Pt $4f$ component in the XPS spectrum due to slightly variant bonding states of the Pt-atoms. The fact that only one doublet component is present in the Pt $4f$-signal indicates one single SiPt bond without any further Pt-Pt bond at the surface. In accordance with LEED measurements, the periodicity of the platinum atoms shows a combination of the c(4×2) and the c(4×6) structure. In contrast to the dimer structure at the clean and reconstructed surface, the Si-atoms rearrange in a cross-like structure between the Pt-atoms. Here, the Si-atoms reveal a buckling of 0.60 Å which is in the order of magnitude of the clean Si(100) dimer buckling.

top view

topmost Si layer

[001]

[100] [010]

cut

1
2
3
4
5
6
7
8

[100]

[00$\bar{1}$] [010]
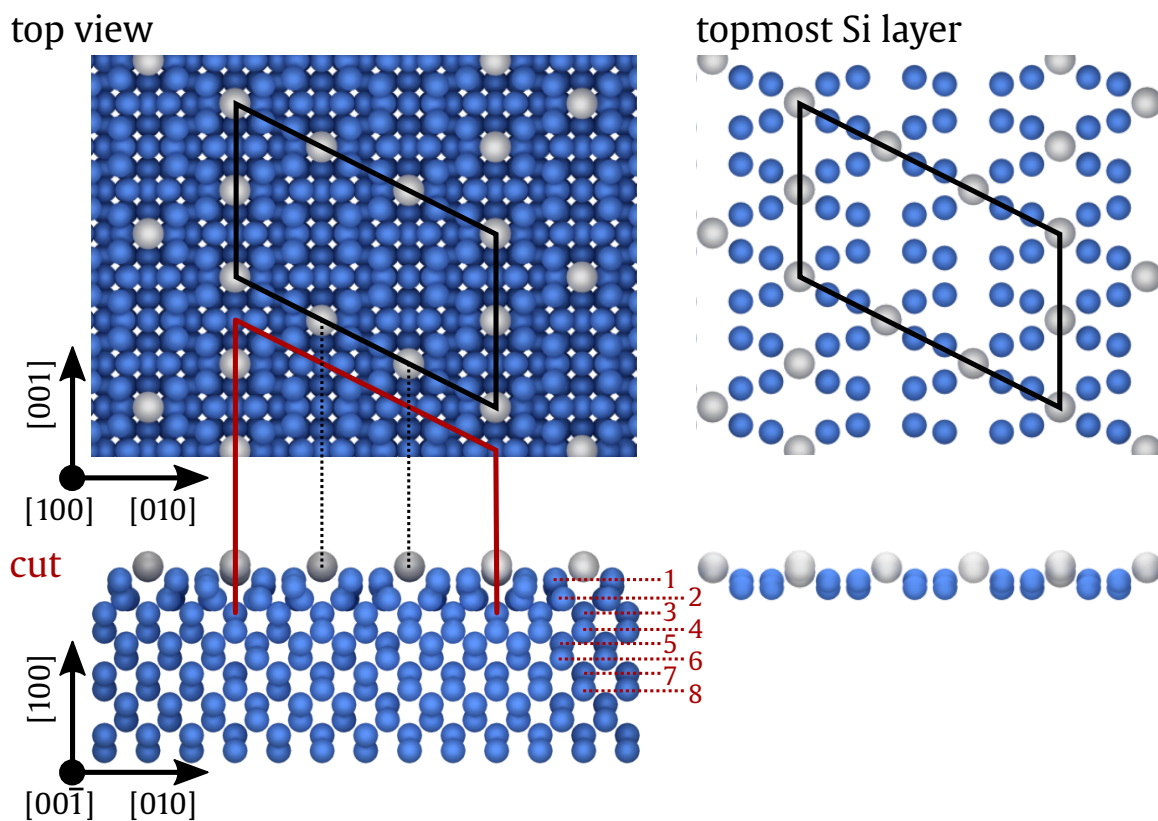
Figure 5.12 Structure model of the Si-Pt silicide surface in a top and a cut side view along the red line. The blue spheres represent Si-atoms and the gray spheres denote Pt-atoms. On the right side, the arrangement of Pt-atoms between the top-most Si layer is displayed.

Chapter 6

Au-Si alloy

In this chapter, the preparation process for a clean Au(110) surface and the formation of a low-dimensional Au-Si alloy is presented. Furthermore, a detailed chemical and structural investigation of both systems is carried out using LEED, XPS, and XPD measurements. The first section deals on the clean and reconstructed Au(110) surface. The results are compared to a former detailed analysis using the same methods as presented in [19]. In the second section, the preparation and analysis of the Au-Si alloy structure is presented. The results of this section are compared to similar studies [7] and are published in [89].

6.1 Reconstructed Au(110) surface

The preparation process from a gold crystal up to the Au-Si alloy starts by preparing a clean and well reconstructed sample surface. A polished Au(110) crystal with a diameter of $10\,\mathrm{mm}$ and $99.999\,\%$ purity is mounted to the molybdenum base plate and transferred into the UHV-chamber. The pristine gold surface is disordered, and due to its storage at ambient pressure, presumably covered with an oxide layer or other adatoms which must be removed. To prevent re-oxidation of the sample, good vacuum conditions are maintained throughout the preparation and measurement procedure. For the preparation of the surface, the first steps are the removal of any kind of contamination and the formation of a (2×1)-reconstruction of the Au(110) surface. Therefore, the sample is processed by repeated cycles of sputtering and annealing. Using a sputter gun, ionized Ar^+ atoms are accelerated onto the Au(110) crystal under an incidence angle of 45°, with a kinetic energy of $E_{\mathrm{sputter}} = 800\,\mathrm{eV}$.
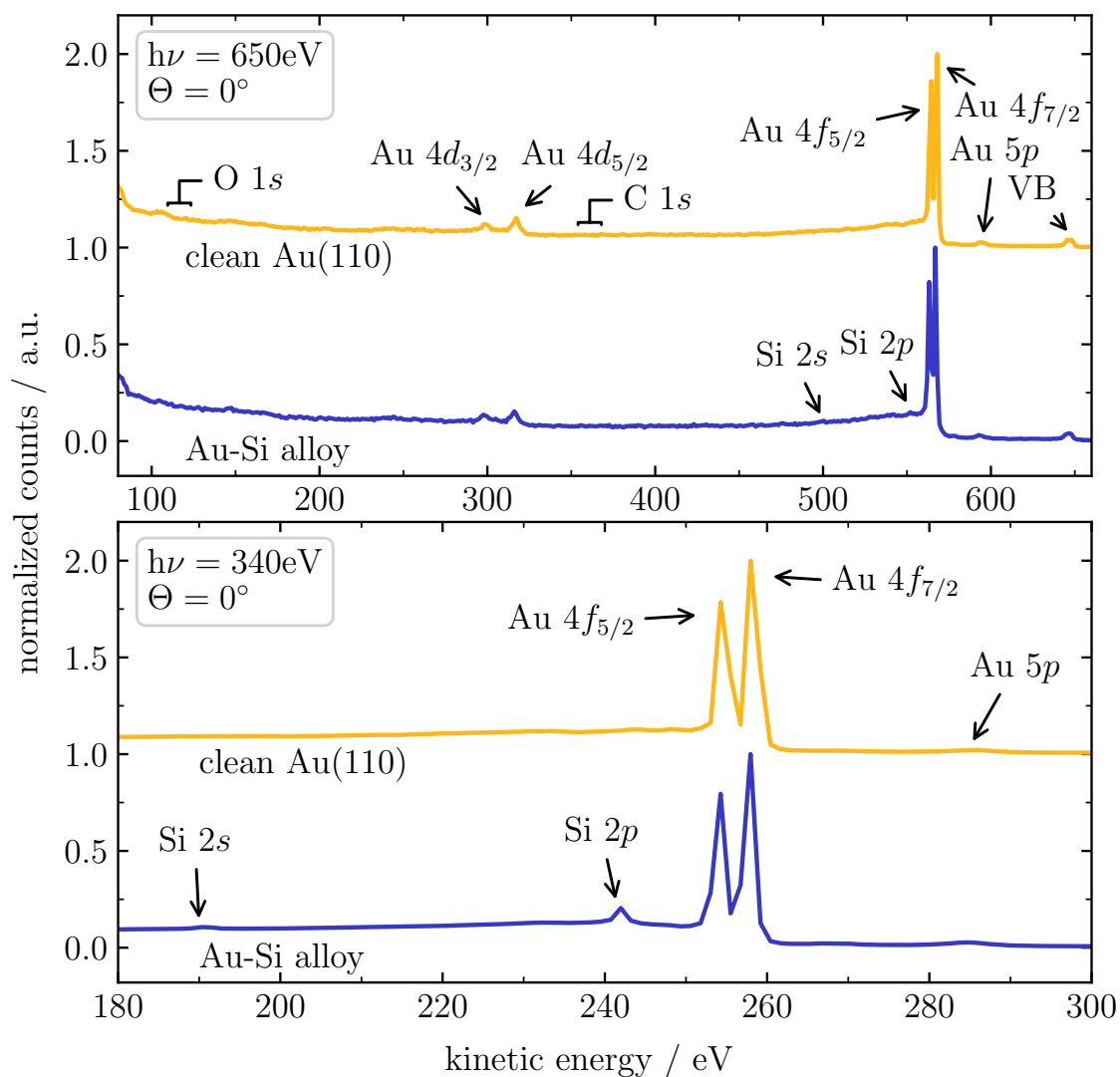
Figure 6.1 X-ray photoelectron survey spectra recorded at photon energies of $h\nu = 650\,\text{eV}$ (top) and $h\nu = 340\,\text{eV}$ (bottom) at an emission angle of $\Theta = 0°$. The clean and (2×1)-reconstructed Au(110) surface spectrum is displayed in yellow and the spectra corresponding to the Au-Si alloy are shown in blue. Image reproduced from [89].

In order to rearrange the surface-atoms of the sputtered surface the sample is heated via resistive heating and annealed for approximately 30 min at $T_{\mathrm{anneal}} \approx 450\,°\mathrm{C}$. After several sputter and annealing cycles, the sample is cooled to room temperature with $20\,°\mathrm{C/min}$. The cleanness of the sample, especially the absence of adatoms like O, C, and N is checked via XPS survey spectra between the preparation steps. Subsequently, LEED measurements were performed to verify a well (2×1)-reconstructed Au(110) surface, as described in the next section 6.1.1. After approximately 30 cycles of sputtering and annealing a clean and reconstructed sample surface is obtained. The survey spectra confirmed a clean surface, as displayed in yellow in figure 6.1. The spectra are recorded at an emission angle of $\Theta = 0°$ and energies of $h\nu = 650\,\mathrm{eV}$ in the top panel, and $h\nu = 340\,\mathrm{eV}$ in the bottom panel. The signals of Au $4d$, Au $4f$, and Au $5p$ are detected with kinetic energies of $E_{\mathrm{kin,Au}\ 4d_{5/2}} = 317\,\mathrm{eV}$, $E_{\mathrm{kin,Au}\ 4f_{7/2}} = 568\,\mathrm{eV}$ [96], and $E_{\mathrm{kin,Au}\ 5p} = 595\,\mathrm{eV}$ [99], respectively. The signals are split into two components, due to spin-orbit coupling as described in section 2.3.3. The absence of the O $1s$ ($E_{\mathrm{kin,O}\ 1s} = 117\,\mathrm{eV}$ [92]) and C $1s$ ($E_{\mathrm{kin,C}\ 1s} = 366\,\mathrm{eV}$ [93]) signals indicates a clean surface.

6.1.1 LEED measurements of the reconstructed Au(110) surface

The LEED pattern as displayed in figure 6.2 a) was recorded at a kinetic energy of $E_{\mathrm{kin}} = 52\,\mathrm{eV}$. It confirms the presence of a well (2×1)-reconstructed surface as reported in literature [82]. The bulk structure spots of the Au(110) surface are marked by yellow circles. A simple bulk signal would reveal a (1×1)-structure in the LEED pattern. The additional spots of the reconstruction in (2×1)-structure are, marked by yellow squares. The LEEDpat [53] simulation in figure 6.2 b) shows the reciprocal lattice of the (2×1)-reconstruction. Again, the yellow circles indicate the bulk signals and the yellow squares depict the spots originating from the (2×1)-reconstruction. In figure 6.2 c) the corresponding periodicity of the r-space lattice is shown. The yellow grid depicts the Au bulk structure beneath the surface spots, where every second row of Au-atoms in the $[00\bar{1}]$ direction is missing. This behavior is typical for the (2×1)-reconstructed missing-row structure. The reciprocal unit cell vectors $\vec{a}*$ and $\vec{b}*$ correspond to the real space unit vectors $\vec{a}$ and $\vec{b}$. The latter describe the dimensions of the surface unit cell. The ratio of the vectors is $\vec{a}/\vec{b} = \vec{b}*/\vec{a}* = \sqrt{2}$ as expected from the dimensions of the unit cell of the substrate. For further chemical investigations, XPS measurements are performed and described in the following section.

a) E_kin=52 eV

b) k-space

c) r-space
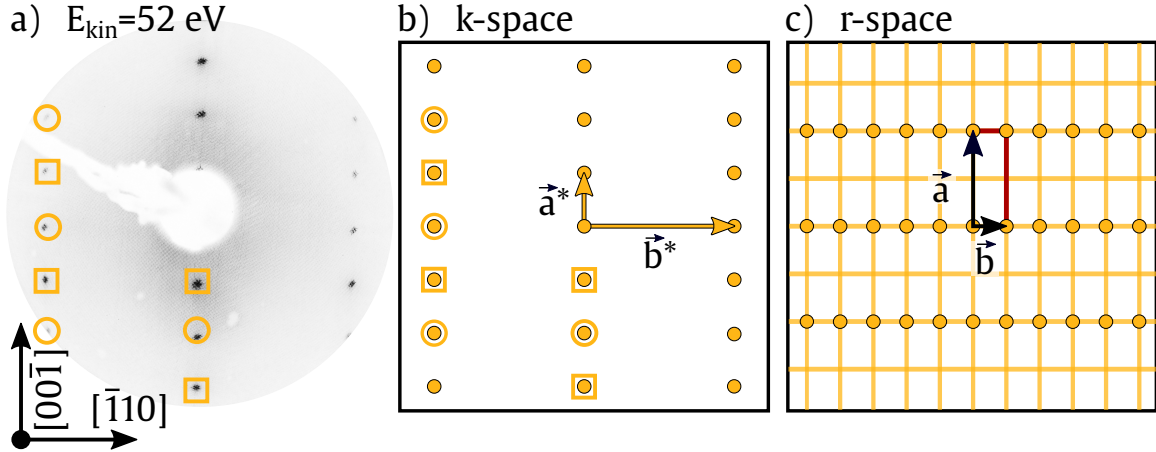
Figure 6.2 LEED pattern of the clean (2×1)-reconstructed Au(110) surface displayed in a) for a primary electron energy of $E_{\mathrm{kin}} = 52\,\mathrm{eV}$. The yellow circles mark the Au(110) bulk structure, while the yellow squares depict the additional (2×1)-reconstruction spots. b) shows the k-space LEEDpat [53] simulation for the clean Au(110) pattern and c) the corresponding r-space simulation. Image reproduced from [89].

6.1.2 XPS measurements of the reconstructed Au(110) surface

High-resolution core-level XPS spectra of the (2×1)-reconstructed Au(110) surface are recorded at a photon energy of $h\nu = 180\,\mathrm{eV}$, a pass-energy of $E_{\mathrm{pass}} = 5.85\,\mathrm{eV}$, and an increment of $\Delta E_{\mathrm{inc}} = 0.123\,\mathrm{eV}$. The Au $4f$ XPS spectra are fitted using UNIFIT 2020 [32] as displayed in figure 6.3. The fit parameters are listed in table 6.1.

For comparison, further spectra were recorded at a photon energy of $h\nu = 340\,\mathrm{eV}$. They are shown in the appendix in figure A.2, and those were fitted with the fit parameters in table A.1, giving similar results. The spectra are taken at normal emission $\Theta = 0°$ shown in the bottom panel, and at $\Theta = 60°$ displayed in the top panel. The asymmetric line shape of the gold sample indicates a metallic character. Therefore, the background is fitted using the Tougaard-background function [37], as described in sec-

Table 6.1 XPS fit parameters of Au $4f$ high-resolution spectra of the clean Au(110) surface at a photon energy of $h\nu = 180\,\mathrm{eV}$. Each spectrum shows a spin-orbit coupling of $\Delta E_{\mathrm{soc}} = 3.67\,\mathrm{eV}$.

$\Theta/°$	Comp.	E_{kin}/eV	FWHM/eV	α	A_{rel}/%
60	Au bulk	92.26	0.49	0.03	62
	Au surface	92.62	0.46	0.03	38
0	Au bulk	92.26	0.49	0.03	69
	Au surface	92.62	0.48	0.03	31

tion 2.3.1. The curve fit is processed with Doniach-Sunjic profiles [40] convoluted with a Gaussian-profile as shown in section 2.3.2. The spectra are split due to spin-orbit coupling with a shift of $\Delta E_{\mathrm{soc}} = 3.67\,\mathrm{eV}$ between the Au $4f_{5/2}$ and the Au $4f_{7/2}$ peak which is in excellent accordance to literature [100].
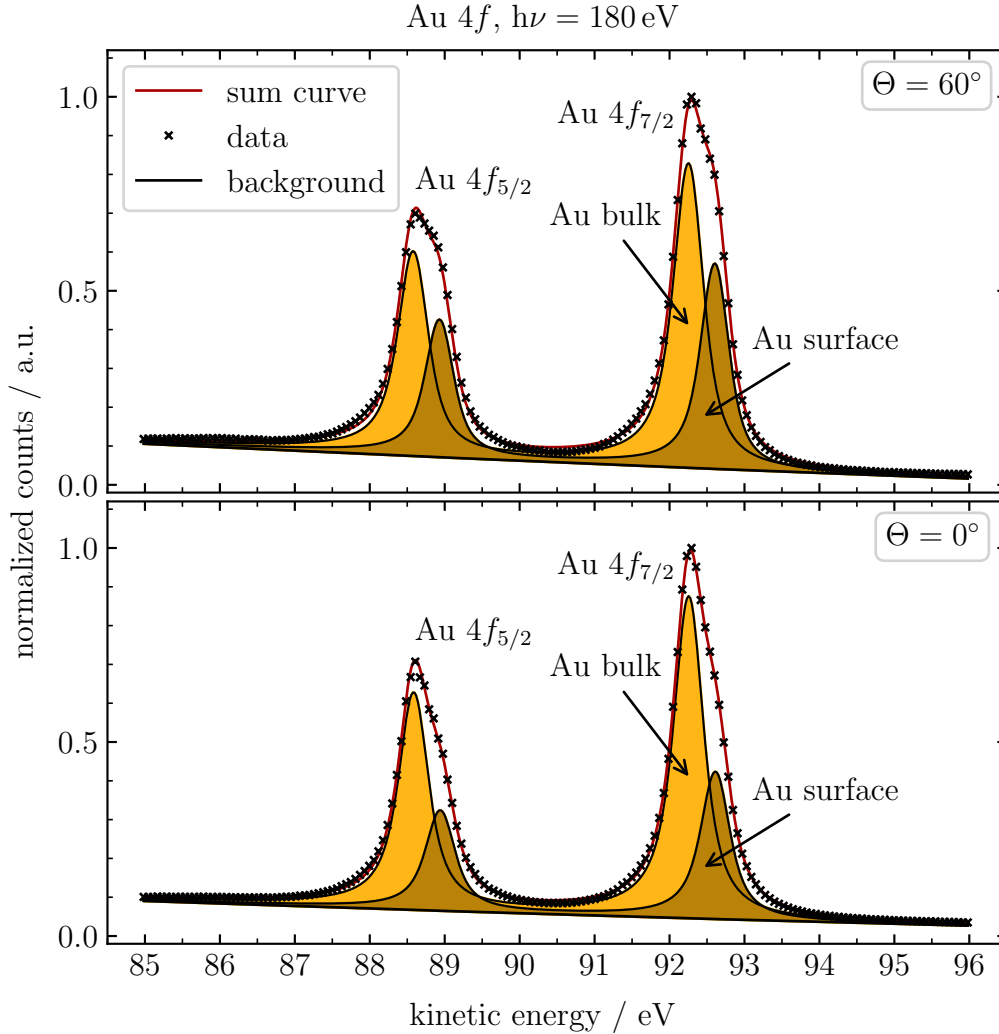
Figure 6.3 High-resolution XPS spectra of the clean Au(110) surface recorded at a photon energy of $h\nu = 180\,\mathrm{eV}$. The Au $4f$ core-level spectra are shown at emission angles of $\Theta = 60°$ and $\Theta = 0°$ in top and bottom panel, respectively. The signal is chemically split into two components.

Each component can be separated into two components due to different chemical environments. A smaller component, displayed in brown, appears with a shift of $\Delta E_{\mathrm{chem}} = 0.35\,\mathrm{eV}$ towards higher kinetic energies relative to the main component

in yellow. At an angle of $\Theta = 60°$ with enhanced surface sensitivity the smaller signal rises from a relative area of $31\%|_{\Theta=0°}$ to $38\%|_{\Theta=60°}$. There is no hint of any contamination at the surface in the survey spectra in figure 6.1. Furthermore, the missing-row reconstruction is expected to give rise to a surface component, as already described by Roese et al. [19]. This can be seen in the behavior of the brown component, so it presumably origins from the top-most Au-atoms on the Au(110) surface. The signals show an asymmetry of $\alpha = 0.03$ and a FWHM of approximately $0.48\,\text{eV}$ which is also in accordance to literature [17]. An increase of the FWHM under a surface sensitive angle is observable.

6.1.3 XPD measurements of the reconstructed Au(110) surface

After the preparation of the (2×1)-reconstructed surface an XPD pattern is recorded. The Au $4f$-signal is measured at a photon energy of $h\nu = 180\,\text{eV}$[1].
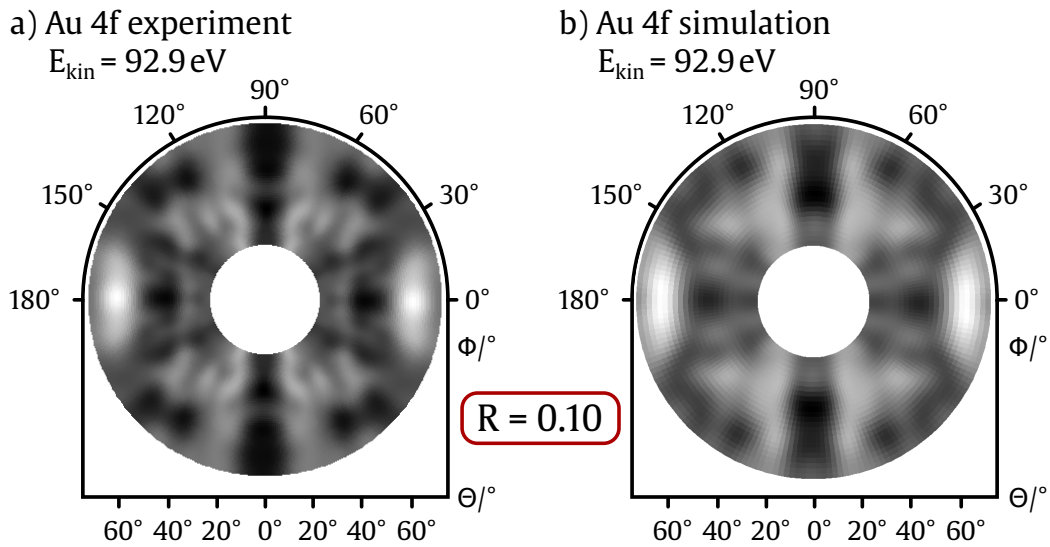
Figure 6.4 The experimental x-ray photoelectron diffraction pattern of the clean and (2×1)-reconstructed Au(110) surface recorded at a photon energy of $h\nu = 180\,\text{eV}$ for the Au $4f$-signal is shown in a). The simulated pattern of the (2×1)-reconstruction is displayed in b).

The XPD pattern is measured with increments of $\Delta\Phi = 1.8°$ and $\Delta\Theta = 2°$ at a polar angle range of $24° \leq \Theta \leq 70°$ and a full $\Phi = 360°$ scan. The pass-energy is set to $E_{\text{pass}} = 23.42\,\text{eV}$ and an increment of $\Delta E_{\text{inc}} = 0.492\,\text{eV}$. In the pattern, a two-fold

---

[1]A detailed XPD analysis of a (2×1)-reconstructed Au(110) XPD pattern recorded at a photon energy of $h\nu = 340\,\text{eV}$ is presented in [19].

rotational symmetry and a mirror planes at $\Theta = 90°$ are visible, as seen in figure 6.4 a). Both symmetries are applied to the raw data after subtracting the background, removing the step, applying an anisotropy function, and a Gaussian-blur with radius 2 as described in section 2.5.2. The crystal structure of the reconstructed Au(110) surface indicates a twofold rotational symmetry as well as a mirror symmetry with horizontal and vertical axes. This is also shown in the XPD pattern as displayed in figure 6.4 a). For simulation of the XPD pattern a cluster of the reconstructed
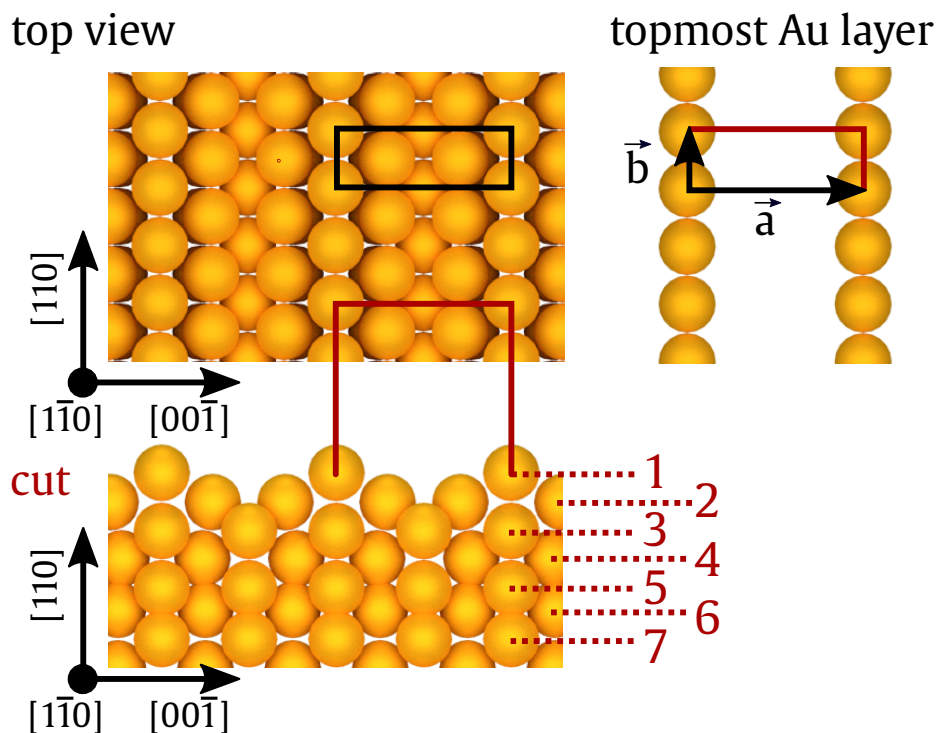
Figure 6.5 Simulated structure model of a clean and reconstructed Au(110) surface in top and cut view with an additional top-most layer view. The red digits number the atomic layers.

Au(110) surface is modified by a relaxation of the top 6 layers. The top-most 18 atoms from the first 5 layers of the unitcell are set as emitter atoms with an emitter radius of 6.0 Å. The simulation is performed using the MSPHD package in combination with the genetic algorithm, as described in section 2.5.2. A scaling of $\pm 1.0\%$ and variations of 0.3 Å in each x-, y-, and z- directions are applied. The best simulated pattern with an R-factor of R = 0.10 is shown in figure 6.4 b). The agreement between experimental and simulated pattern confirms the reconstruction of the surface on an atomic scale. The variation of the atoms' distance are nearly the same compared to

values reported in literature [19, 82].The simulated structure is displayed in figure 6.5 with yellow spheres as gold atoms.

6.2 Preparation of the Au-Si alloy

For the preparation of the Au-Si alloy, pure silicon is deposited onto the surface via physical vapor deposition. Similar to the preparation of a clean Si surface, the pressure of the UHV-chamber is of great influence on the cleanness of the silicon. Thin layers of silicon on Au(110) form no ordered structures at room temperature, so the heating of the sample is crucial [101]. The sample is held at a temperature of approximately $T = 400\,°C$ during the evaporation process, via the tungsten filament at a power of $11.2\,W(4.0\,V, 2.8\,A)$. The temperature is monitored with a pyrometer. For Si evaporation, the silicon plate in the evaporator is heated up to approximately $1000\,°C$ with a power of $64\,W(4.7\,V, 13.6\,A)$. Prior to this, the growth rate was estimated to be approximately $1\,Å/h$ via a quartz crystal microbalance as displayed in figure 6.6. Thus, a total silicon coverage of approximately $1.0\,Å$ is reached after $60\,min$ evaporation time, corresponding to 0.2 ML coverage[2]. Again, the formation process is monitored via XPS and LEED measurements. In figure 6.1, the XPS survey spectra of the Au-Si alloy are recorded at energies of $h\nu = 340\,eV$ and $h\nu = 650\,eV$ in blue in the top and bottom panel, respectively. In addition to the gold signals, new signals of Si $2s$ and Si $2p$ arise at energies of $E_{\text{kin,Si } 2s} = 500\,eV$ [91], and $E_{\text{kin,Si } 2p} = 550\,eV$ [91]. The absence of O, N, or C signals indicates a clean silicon deposition without any contamination.

---

[2]The definition of one monolayer Si on the Au(110) surface relates to the coverage of one layer silicon with the reference of the hexagonal arrangement at the Si(111) surface $(1.0\,Å \approx 0.2\text{ML})$.
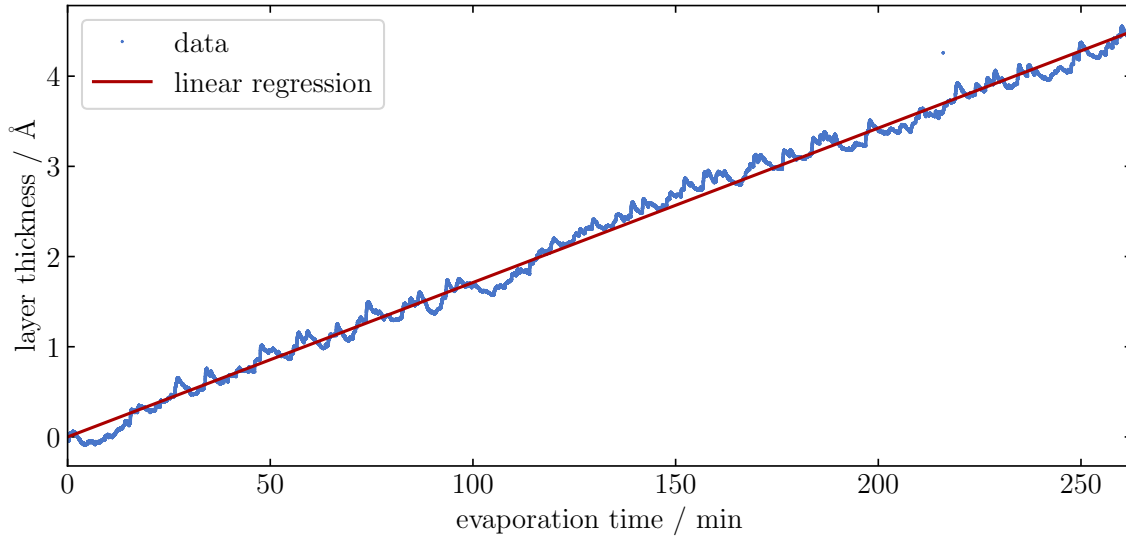
Figure 6.6 Quartz crystal microbalance measurement of silicon evaporation at a power of $P_{Si} = 63\,W$.

6.3 LEED measurements of the Au-Si alloy

For the determination of the geometric properties of the structure and its unit-cell, low-energy electron diffraction (LEED) patterns of the Au-Si alloy are recorded and analyzed using LEEDpat [53]. The resulting pattern recorded at an energy of $E_{kin} = 52\,eV$ is displayed in figure 6.7 a). The pattern shows a twofold rotational and also a mirror symmetry along horizontal and vertical axes. The yellow circles mark the remaining (1×1)-substrate superstructure. In comparison to the pattern of the clean Au(110) surface in figure 6.2 a), the missing-row reconstruction vanishes, as the corresponding spots disappeared in the pattern. The blue squares indicate the missing (2×1)-reconstruction spots. In figure 6.7 b) the arrangement of the LEED spots is reproduced by a LEEDpat simulation. The simulation reveals two overlapping domains described by the matrices $\left(\begin{smallmatrix} 10 & -2 \\ -1 & 4 \end{smallmatrix}\right)$ and $\left(\begin{smallmatrix} 10 & 2 \\ 1 & 4 \end{smallmatrix}\right)$. This was also obtained for a successfully prepared Au-Si alloy by Enriquez et al. [7]. The LEEDpat simulation revealed a unit cell shown in the real space image in figure 6.7 c). The blue spots indicate the periodicity of the silicon structure. The yellow grid beneath the blue spots displays the substrate (1×1) bulk-atom positions. While comparing the LEED pattern of the Au-Si alloy to the pattern of the clean Au(110) surface, it is noticeable that the reconstruction spots vanished. The silicon nano-ribbon system at a higher silicon coverage as described in section 4.7 shows a missing-row structure under the
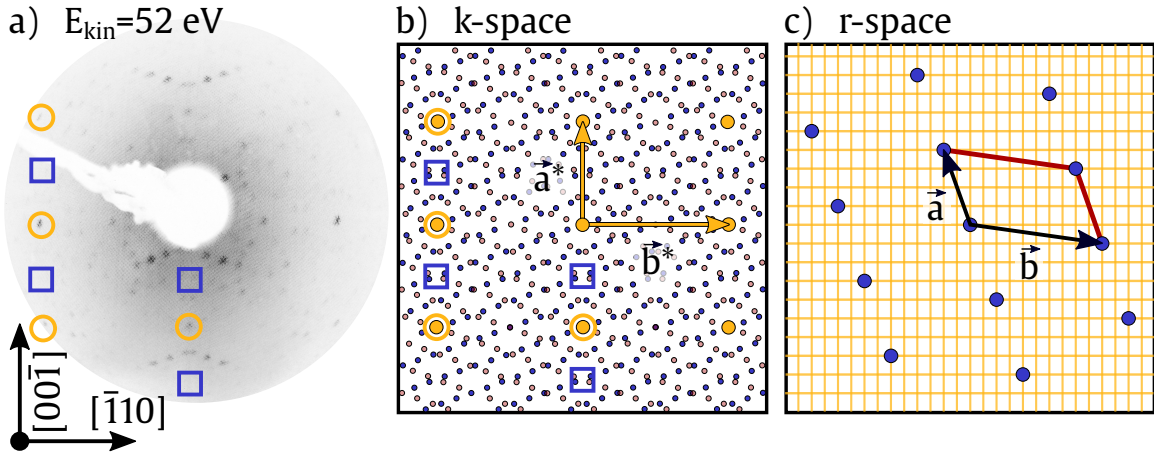
Figure 6.7 LEED pattern of the Au-Si alloy structure at a deposition of 0.2 ML silicon onto the Au(110) sample for a primary electron energy of $E_{\mathrm{kin}} = 52\,\mathrm{eV}$ displayed in a). Yellow circles indicate spots to the Au(110) (1×1) bulk structure. The blue squares mark the missing (2×1)-spots in the Au-Si alloy structure. In b) the k-space LEEDpat simulation for the Au-Si alloy structure shows two overlapping domains with the matrices $\left(\begin{smallmatrix} 10 & -2 \\ -1 & 4 \end{smallmatrix}\right)$ and $\left(\begin{smallmatrix} 10 & 2 \\ 1 & 4 \end{smallmatrix}\right)$ in blue and red, respectively. This has been reported by Enriquez et al. [7]. The real space unit cell to the first matrix is displayed in c). Here, the periodicity of the Au(110) bulk structure is displayed as yellow grid. Image reproduced from [89].

Si-atoms [17] again. This could indicate a rearrangement of the top-most gold atom layer during the preparation process. In the Au-Si alloy the top-most gold atoms of the row structure are likely rearranged between the Si-atoms without forming ordered rows.

6.4 XPS measurements of the Au-Si alloy

For a detailed chemical analysis of the Au-Si alloy, high-resolution core-level XPS spectra are taken under emission angles of $\Theta = 60°$ and $\Theta = 0°$. The pass-energy is set to $E_{\mathrm{pass}} = 5.85\,\mathrm{eV}$ and the increment to $\Delta E_{\mathrm{inc}} = 0.061\,\mathrm{eV}$. The XPS spectra are shown in figure 6.8 for the Au $4f$ and in figure 6.9 for the Si $2p$ region with the fit parameters listed in tables 6.2 and 6.3, respectively. The fit was performed using the UNIFIT program [32]. The Au $4f$-signal is recorded at a photon energy of $h\nu = 180\,\mathrm{eV}$. Further spectra supporting these fit results were recorded at a photon energy of $h\nu = 340\,\mathrm{eV}$, and are shown in the appendix in figure A.3. The corresponding fit parameters are presented in table A.2.

Alike the spectrum of the clean Au surface, the Au $4f$ component is split by $\Delta E_{\text{soc}} = 3.67\,\text{eV}$ due to spin-orbit coupling. The Au-Si system reveals three different chemical components. The yellow component is the dominant contribution with relative peak areas of $65\%|_{\Theta=0°}$ and $53\%|_{\Theta=60°}$. As the signal decreases significantly when recording at a surface sensitive angle, the component can be assigned to Au bulk-atoms. It appears at a kinetic energy of $E_{\text{kin,Au bulk}} = 91.58\,\text{eV}$. The brown Au surface component of the

Table 6.2 XPS fit parameters of Au $4f$ high-resolution spectra of the Au-Si alloy at a photon energy of hν = 180 eV. Each spectrum shows a spin-orbit separation of $\Delta E_{\text{soc}} = 3.67\,\text{eV}$.

$\Theta/°$	Comp.	E_{kin}/eV	FWHM/eV	α	$A_{\text{rel}}/\%$
	Au bulk	91.59	0.52	0.04	53
60	AuSi$_1$	90.91	0.67	0.04	28
	AuSi$_2$	91.20	0.51	0.04	19
	Au bulk	91.58	0.52	0.04	65
0	AuSi$_1$	90.91	0.66	0.04	21
	AuSi$_2$	91.20	0.52	0.04	14

clean Au spectrum in figure 6.3, which is shifted towards higher kinetic energies vanishes. Beside the bulk signal two components arise, shifted towards smaller kinetic energies marked in blue. This indicates a changed chemical environment of several Au-atoms due to silicon adsorption. At higher surface sensitive angles both components rise with a nearly constant peak ratio of AuSi$_1$/AuSi$_2$ = 3/2. Thus, both components might be assigned to bonds between gold and silicon located at the surface.

The component AuSi$_1$ in light blue shows a chemical shift of $\Delta E_{\text{chem}} = 0.67\,\text{eV}$ relative to the bulk component. A shift of $\Delta E_{\text{chem}} = 0.63\,\text{eV}$ has been reported in XPS measurements of silicon nano-ribbons on Au(110) [19].

Compared to the spectra of the nano-ribbons, a smaller shift could be obtained in the dark blue component AuSi$_2$ with $\Delta E_{\text{chem}} = 0.38\,\text{eV}$. This indicates a strong bond between silicon and gold in the AuSi$_1$ component. The FWHM for the bulk and the AuSi$_2$ component are determined to be approximately 0.52 eV. For the AuSi$_1$ component the FWHM is slightly larger with 0.67 eV, indicating a different chemical environment of the involved atoms.

Table 6.3 XPS fit parameters of Si $2p$ high-resolution spectra of the Au-Si alloy at a photon energy of hν = 140 eV. Each spectrum shows a spin-orbit coupling of $\Delta E_{\text{soc}} = 0.61\,\text{eV}$.

$\Theta/°$	Comp.	E_{kin}/eV	FWHM/eV	α	$A_{\text{rel}}/\%$
60	Si$_1$	36.47	0.27	0.12	67
	Si$_2$	36.65	0.26	0.12	33
0	Si$_1$	36.47	0.28	0.12	66
	Si$_2$	36.65	0.26	0.12	34
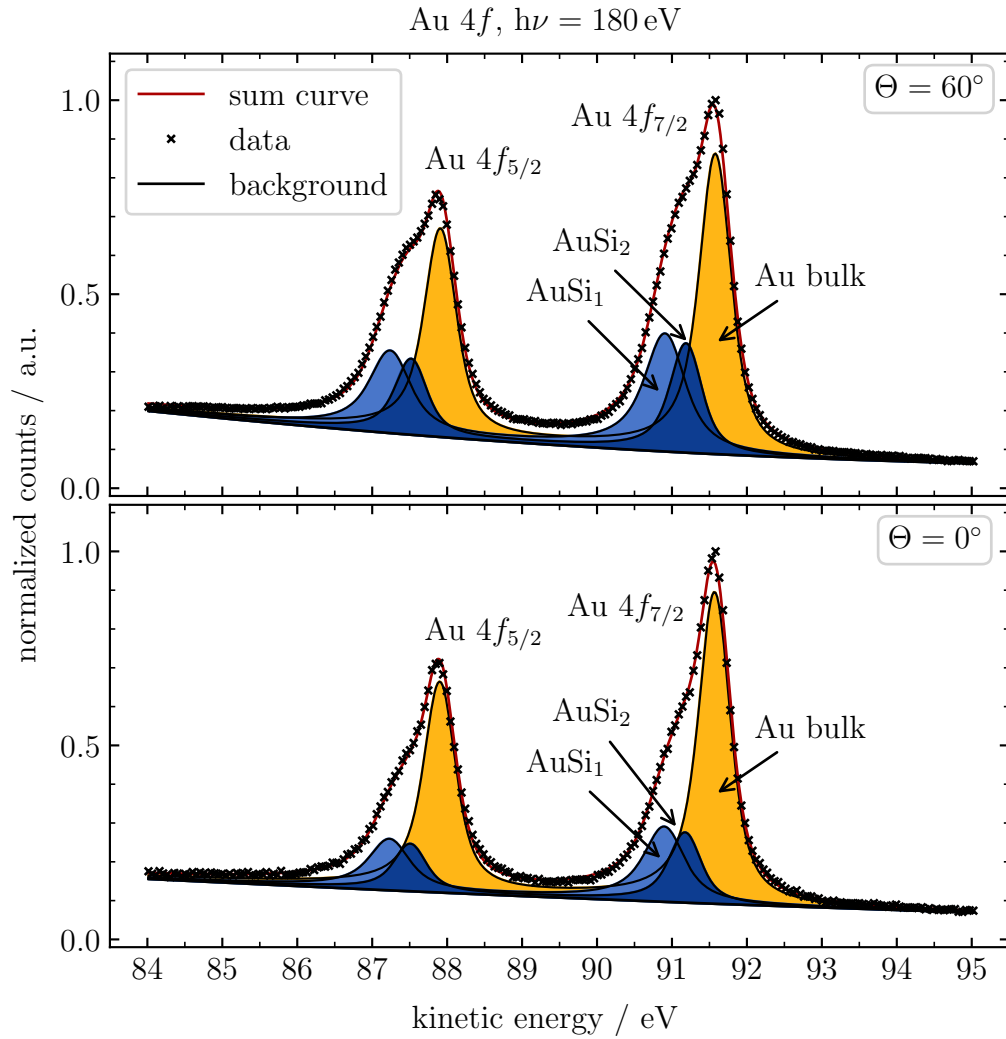
Au $4f$, h$\nu = 180\,\mathrm{eV}$

Figure 6.8 High-resolution spectra of the Au-Si alloy recorded at a photon energy of h$\nu = 180\,\mathrm{eV}$. The Au $4f$ core-level spectra are shown at emission angles of $\Theta = 60°$ and $\Theta = 0°$ in top and bottom panel, respectively. Besides the Au bulk signal (yellow), two AuSi components arise, shifted towards lower kinetic energies, displayed in blue. Image reproduced from [89].
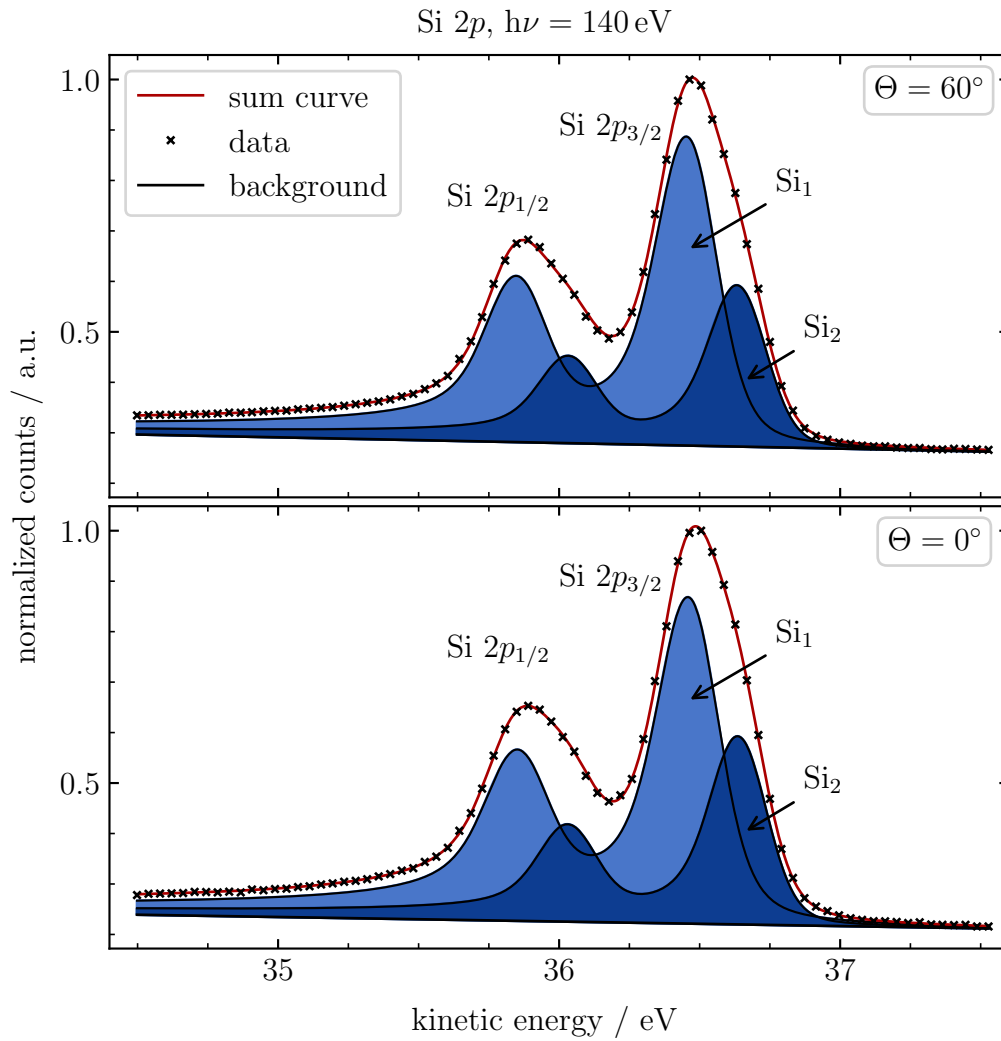
Figure 6.9 High-resolution XPS spectra of the Si $2p$-signal of the Au-Si alloy, recorded at a photon energy of $h\nu = 140\,\text{eV}$, at emission angles of $\Theta = 60°$ and $\Theta = 0°$ in top and bottom panel, respectively. Image reproduced from [89].

An asymmetry of $\alpha = 0.04$ has been reported in literature before [19]. The Si $2p$ spectra in figure 6.9 are recorded with a photon energy of h$\nu = 140$ eV at emission angles $\Theta = 60°$ and $\Theta = 0°$, as displayed in top and bottom panel, respectively. The corresponding fit parameters are presented in table 6.3. Similar spectra are recorded at a photon energy of h$\nu = 180$ eV. They are shown in the appendix in figure A.4 and table A.3, giving similar results. Due to the metallic influence of the Au-atoms on the Si components the spectra are fitted using a Doniach-Sunjic function [40] convolved with a Gaussian-distribution and a Tougaard-background function [37], as described in the sections 2.3.2 and 2.3.1, respectively. The signals reveal a split of $\Delta E_{\mathrm{soc}} = 0.61$ eV due to spin-orbit coupling between the Si $2p_{1/2}$ and the Si $2p_{3/2}$ component. Each signal is split in two chemically shifted components Si_1 in light blue and Si_2 in dark blue. The area $\mathrm{Si}_1/\mathrm{Si}_2$-ratio is 2/1. A variation of the emission angle revealed no significant variation between the components. This indicates that the Si-atoms are located only at the surface without emplacement of Si-atoms in the bulk. Both components reveal a similar FWHM of approximately 0.27 eV and an asymmetry parameter of $\alpha = 0.12$ which is in good accordance to literature [19]. Similar to what has already been described for the silicon nano-ribbon system, the Au-Si alloy exhibits a comparatively large asymmetry parameter. This indicates a strong metallic character of the silicon formation which has been reported for silicon nano-ribbons on Au [17] and also on Ag [102]. For further structural investigation XPD measurements are performed for the Au-Si alloy system.

6.5 XPD measurements of the Au-Si alloy

For the Au-Si alloy system, XPD patterns are recorded of the Au $4f$ and also of the Si $2p$-signal and compared to simulated patterns of different atom cluster models. The patterns are recorded with a pass-energy of $E_{\mathrm{pass}} = 5.85$ eV, an increment of $\Delta E_{\mathrm{inc}} = 0.061$ eV, at a polar angle range of $24° \leq \Theta \leq 70°$ and a full $\Phi = 360°$ scan with increments of $\Delta\Phi = 1.8°$ and $\Delta\Theta = 2°$. Both patterns feature a twofold rotational symmetry, and a mirror symmetry along the horizontal and vertical directions. Beside a background subtraction, a step removal, and the application of an anisotropy function, the symmetry operations are applied to the raw data. Moreover, a Gaussian-blur with radius 2 is used to remove statistical fluctuations as described in section 2.5.2. The Si $2p$ XPD pattern, measured at a photon energy of h$\nu = 140$ eV, is shown in figure 6.10 a). The Au $4f$ XPD pattern, recorded at h$\nu = 180$ eV, is dis-

played in figure 6.10 c). The Au $4f$ pattern of the Au-Si alloy reveals several features similar to the pattern of the (2×1)-reconstructed Au(110) surface in figure 6.4 a). Nevertheless, differences in the details of the structure can be spotted. Initially, the structure system as proposed by Enriquez et al. [7] and displayed in figure 4.9 a) is simulated. For the Au $4f$ and the Si $2p$ simulation the EDAC, and MSPHD packages are used, respectively. The emitter radii are determined from the IMFP at the corresponding kinetic energy as $6\,\text{Å}$ for Au $4f$ and $7\,\text{Å}$ for Si $2p$. Slight variations of the emitter radii are tested. A variation of several groups and also single atoms in the first layers of the unit cell in x-, y-, and z-direction of $0.3\,\text{Å}$ and a scaling of the whole cluster of $\pm 1.0\%$ in all three dimensions are applied. Due to the appearance of two mirrored domains, a twofold rotational symmetry as well as a mirror symmetry for $\Theta = 90°$ are applied to the simulation. The resulting simulated XPD pattern for the Au $4f$-signal of structure A is shown in figure 6.10 b) with an R-factor of 0.41. In figure 6.10 d), the simulated Si $2p$ pattern reveals an R-factor of 0.35. A visual comparison as well as the R-factors of around 0.4 indicate that the proper structure is not yet found. The Au pattern shows more structural consistencies than the Si pattern. The reason could be that for the Au environment the influence of the bulk emitters are stronger than for the Si environment.

For further simulations, new cluster models with different silicon arrangements at the surface are tested. Based on the XPS results there is no evidence of Si-atoms located beneath the top-most layer. An even number of Si-atoms symmetrically placed within the unitcell was recommended by former investigations [7]. Both, the clean Au(110) surface and also the nano-ribbon coated surface reveal a (2×1)-reconstruction at the surface [17]. Therefore, it is likely that the transition phase also shows a similar atomic arrangement. Nevertheless, the spots of the reconstruction seem to disappear in the LEED pattern. This could indicate a rearrangement of the top-most Au-atoms between the Si arrangement. Systematically single Au-atoms are added and removed within different Si arrangements in the unit cell. Cluster models with different amounts of Si-atoms are tested in combination with a flat and unre-constructed surface, a (2×1)-reconstructed model, and a mixed system, respectively. Each cluster model is simulated for Au $4f$ and also Si $2p$. Again, a twofold rotational symmetry and also a mirror symmetry for $\Theta = 90°$ are applied to the simulation. A variation of all surface-atoms in x-, y-, and z-direction of $0.15\,\text{Å}$ and a scaling of the whole cluster of $\pm 0.5\%$ are applied.

a) Si 2p experiment
E_{kin} = 36.5 eV

b) Si 2p simulation structure A
E_{kin} = 36.5 eV

R = 0.41

c) Au 4f experiment
E_{kin} = 91.9 eV

d) Au 4f simulation structure A
E_{kin} = 91.9 eV

R = 0.35
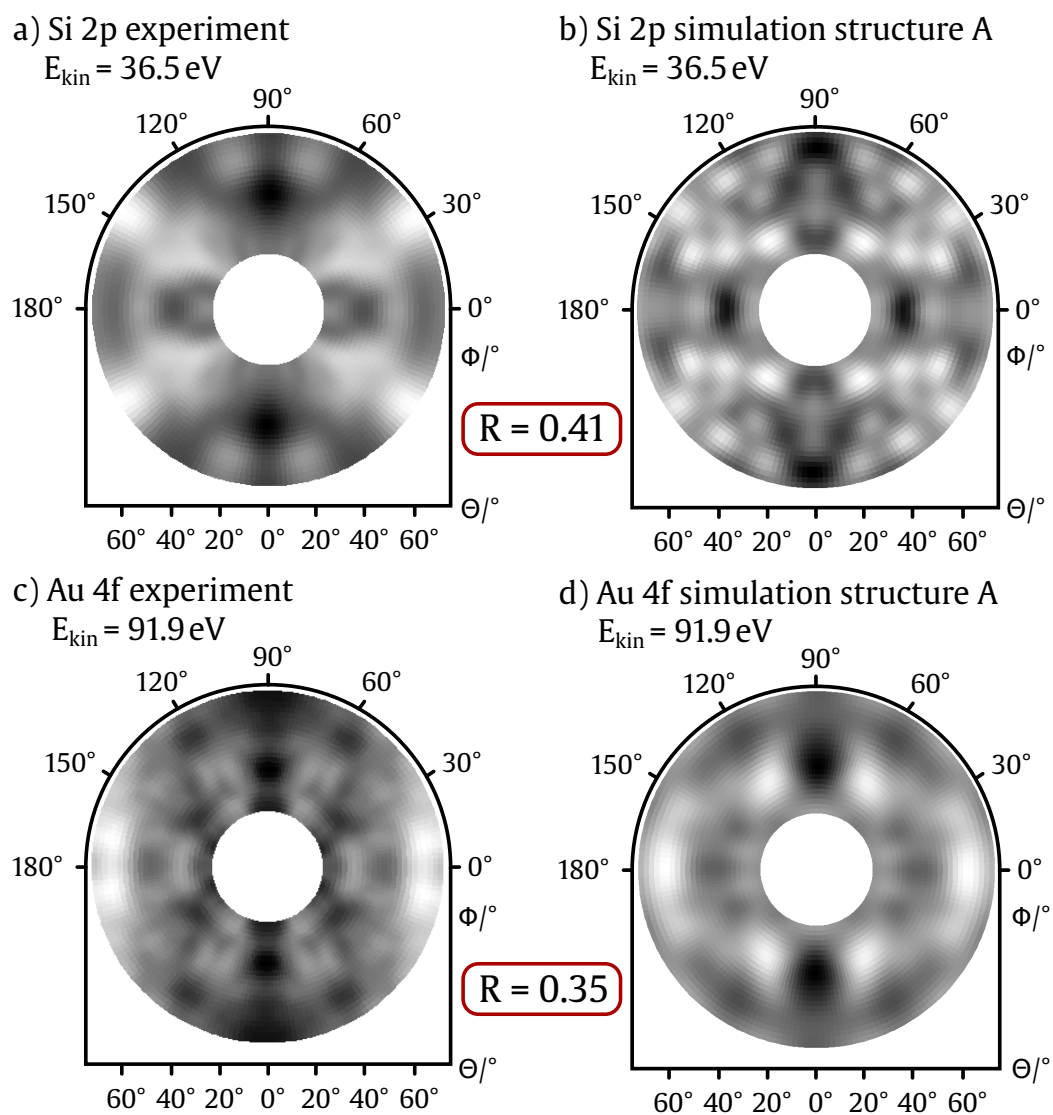
Figure 6.10 X-ray photoelectron diffraction patterns of the Au-Si alloy recorded at photon energies of hν = 140 eV for Si 2p a) and at hν = 180 eV for Au 4f c). Simulated patterns of the structure model A [7] are shown in b) and d) for Si 2p and Au 4f, respectively. Image reproduced from [89].
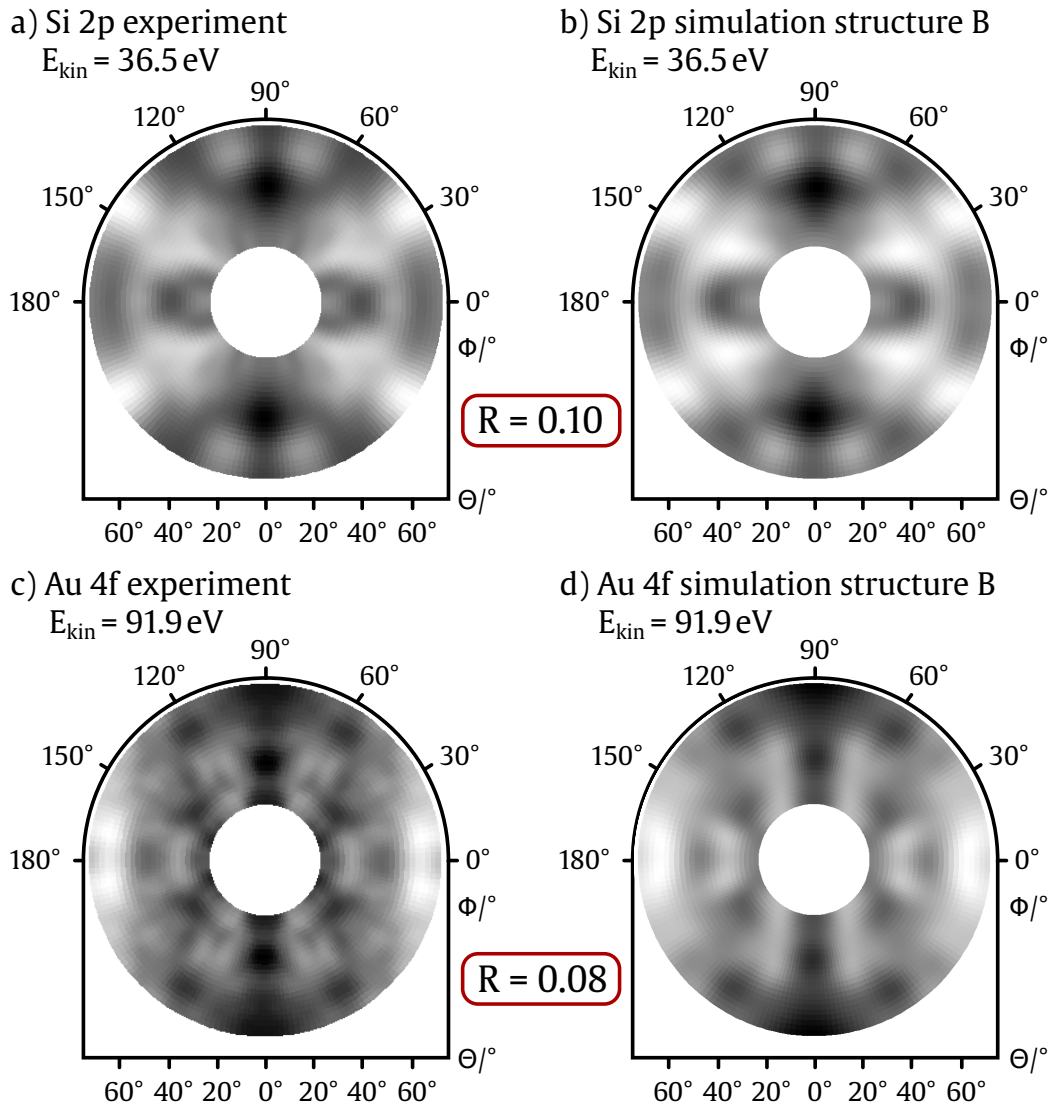
Figure 6.11 X-ray photoelectron diffraction patterns of the Au-Si alloy recorded at photon energies of hν = 140 eV for Si 2p a) and at hν = 180 eV for Au 4f c). Simulated patterns for the best structure model B are shown in b) and d) for Si 2p and Au 4f, respectively. Image reproduced from [89].

top view

topmost Au layer

cut
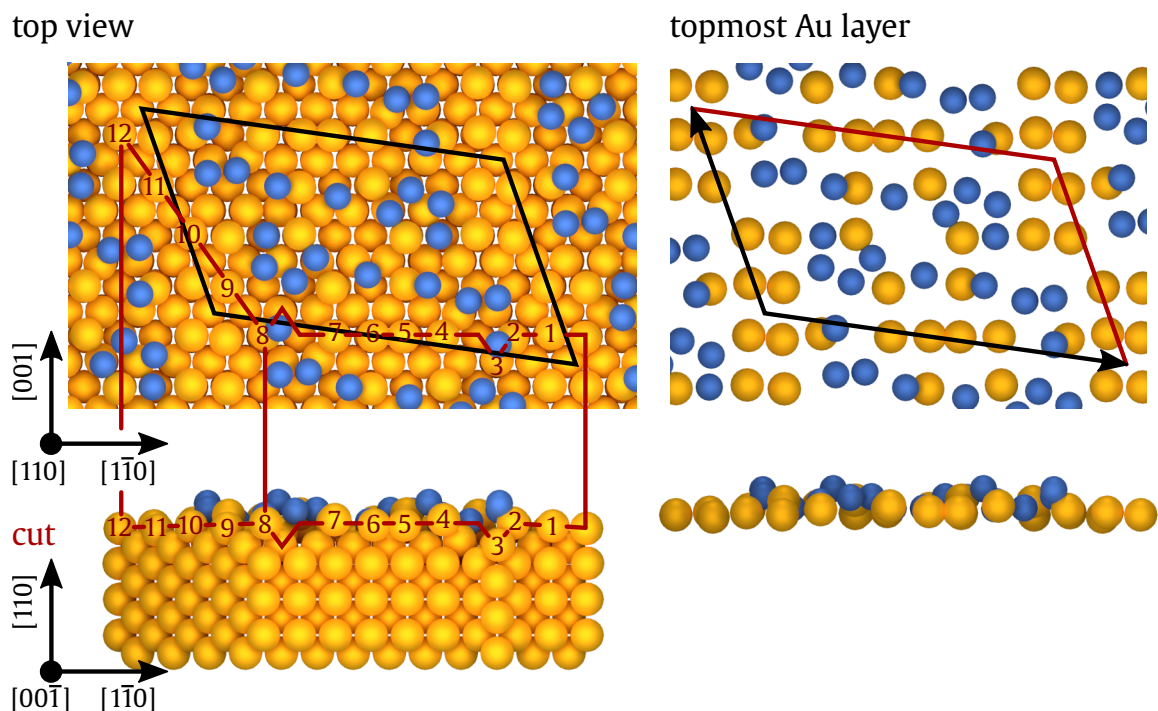
Figure 6.12 Structure model of the Au-Si alloy surface in a top and a cut side view. The yellow spheres represent gold atoms and the blue spheres denote Si-atoms. Additionally, the top-most layer is shown in the two selected perspectives. Image reproduced from [89].

The simulation is performed using the EDAC package for the Au $4f$ simulation with an emitter radius of $6\,\text{Å}$ and the MSPHD package for the Si $2p$ pattern with $7\,\text{Å}$ as emitter radius. Using the genetic algorithm the best fitting simulation is compared to the measured patterns in figure 6.11. For the simulated Si $2p$ pattern in figure 6.11 b) an R-factor of R $= 0.10$ is reached. The simulated Au $4f$ pattern is displayed in figure 6.11 d) and it is in excellent accordance to the experimental pattern indicated by R $= 0.08$. This result is reached for the cluster model displayed in figure 6.12. The resulting structure shows the same periodicity, symmetry and has identical size of the unit cell as the structure model proposed by Enriquez et al. [7]. The unit cell is also in accordance with the matrices $\left(\begin{smallmatrix} 10 & -2 \\ -1 & 4 \end{smallmatrix}\right)$ and $\left(\begin{smallmatrix} 10 & 2 \\ 1 & 4 \end{smallmatrix}\right)$ identified from the LEED pattern. Nevertheless, there are some remarkable differences in the structural arrangement. The Au substrate structure is a modification of the (2×1)-reconstructed missing-row structure. Here, the top-most Au-atoms are arranged between the Si adsorbate instead of building the typical row-like arrangement. This could be an indication of the vanishing missing-row spots in the LEED pattern. Instead of 12 Si-atoms and

38 Au-atoms as in the former proposed structure, the unit cell of the new system contains 18 Si-atoms and 54 Au-atoms. All of the Si-atoms are located in the top-most layer, exactly as the XPS-measurement indicated. The silicon unit cell has a maximum distance of $23.4\,\text{Å}$ and $17.5\,\text{Å}$ in $[\bar{1}10]$ and $[001]$ direction, respectively. The distance from the uppermost to the lowest Si-atom in $[110]$ direction is $1.6\,\text{Å}$. For a more detailed analysis of the chemical components found in the XPS measurements, a decomposition of the Si $2p$ XPD pattern is performed.

6.5.1 Decomposition of the Au-Si alloy XPD pattern

By separating the two different components fitted to the Si $2p$ high-resolution XPS spectra for each of the 4800 spectra in the corresponding Si $2p$ XPD pattern, new patterns related to each single component are generated. A simulation containing different groups of emitter atoms enables an identification of the distinct components. Therefore, the Si $2p$ XPD pattern which is displayed in figure 6.11 a) is separated into the two individual components found in the XPS fit of the spectra in figure 6.13 b). The resulting new patterns are displayed in figure 6.13 a) and figure 6.13 c) for the components Si_1 and Si_2, respectively. For the MSPHD simulation of the components different groups of Si-atoms are set as emitter atoms with a radius of $6\,\text{Å}$. Again, variations of $0.15\,\text{Å}$ in x-, y-, and z-directions, and a scaling of the whole cluster of $\pm0.5\%$ are applied to the cluster model. The best resulting combination of Si-atom groups is shown in figure 6.13 e). The corresponding simulated patterns are displayed in figure 6.13 d) and 6.13 f) for the components Si_1 and Si_2, respectively. The R-factor for both patterns is < 0.1 which indicates an excellent agreement to the decomposed experimental pattern. The component Si_1 which is the dominant component and displayed in light blue results from 12 Si-atoms in the unit cell. Each of the Si-atoms is located on top of a triplet of gold atoms, as indicated in figure 6.13 b). The minor component Si_2 as depicted in dark blue results from a group of 6 atoms in the unit cell. Each of those atoms is located in a centered position above a gold atom. The fit of the Si $2p$ XPS high-resolution spectra resulted in a 2:1 stoichiometry which is confirmed by the ratio of the respective atom numbers.
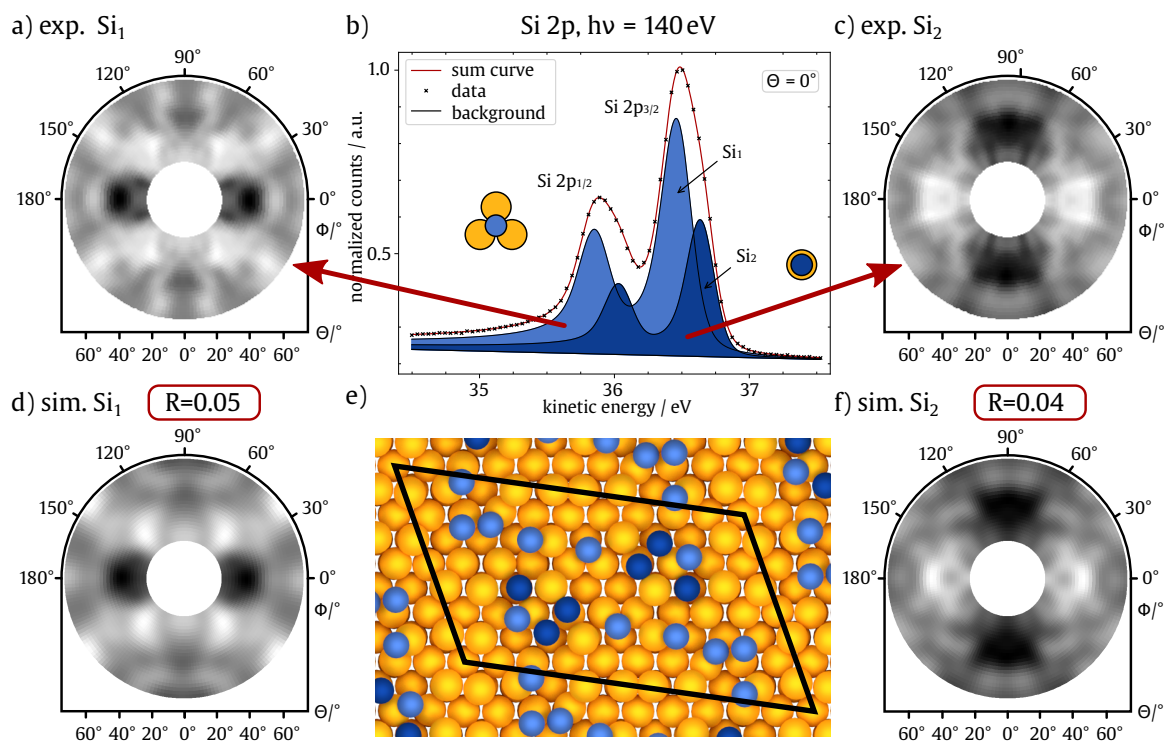
Figure 6.13 Decomposition of the Si 2*p* photoelectron diffraction pattern of the Au-Si alloy recorded at a photon energy of hν = 180 eV. The experimental pattern is decomposed into two components Si_1 a) and Si_2 c) based on the XPS spectrum b). The simulated patterns of the components are displayed beneath the experimental patterns d) and f) for Si_1 and Si_2, respectively. The light and dark spheres denote the components Si_1 and Si_2 in the structure image e). Image reproduced from [89].

Chapter 7

Conclusion

This work addresses the structural arrangement and chemical properties of silicon-based low-dimensional surface structures. Using complementary surface-sensitive methods, a detailed analysis of two sub-monolayer systems and also the clean substrates is carried out. The samples are investigated using LEED, XPS, and XPD techniques. Initially, a clean Si(100) surface is investigated and subsequently coated with a platinum layer, forming a Si-Pt silicide. As a second system, a clean and reconstructed Au(110) substrate is examined with sub-monolayer silicon as adsorbate, forming a Au-Si alloy phase. All measurements are conducted at beamline 11 at the electron storage ring DELTA in Dortmund.

The clean Si(100) surface is achieved by flashing the sample up to $T \approx 1000\,°\mathrm{C}$ and subsequently cooling to room temperature. The cleanness is checked by XPS survey spectra that lack the presence of any oxygen signatures. At the clean surface, a $\mathrm{p}(2 \times 1)$-reconstruction is observed in LEED measurements. Further high-resolution XPS spectra of the Si $2p$-signal reveal several chemically shifted components. Beside the silicon bulk component a surface component arises, shifted by $\Delta E_\mathrm{chem} = 0.35\,\mathrm{eV}$. Due to long data acquisition times and the high reactivity of the silicon sample, an oxidation of the sample could not entirely be omitted. Thus, the cleaning and reconstruction procedure is repeated and checked by LEED and XPS before the XPD measurements are performed. For the XPD data analysis, the bulk component from the XPS spectrum was used. The obtained experimental XPD patterns were compared with the results from the EDAC simulation. The simulation reveals a buckled dimer structure with a $\mathrm{p}(2 \times 1)$-periodicity as expected from the LEED pattern. The atomic relaxations of the reconstruction are in good accordance to literature. After an additional cleaning process, a thin layer of platinum is evaporated onto the surface.

Sub-monolayer platinum on Si(100) can yield different structural arrangements at the surface, depending on the initial coverage and on the annealing temperature. In this study, 1/6 ML platinum are deposited onto a clean and reconstructed Si(100) surface via electron beam evaporation. After the deposition, the sample is annealed in a flashing process up to $T \approx 1000\,°C$. The investigation via LEED reveals a change from the p(2×1)-reconstruction spot arrangement of the clean surface to a combination of c(4×2) and c(4×6)-spots. High-resolution core-level XPS spectra of the Si $2p$-signal reveal two components, chemically shifted by $\Delta E_{\text{chem}} = 0.34\,\text{eV}$. The Pt $4f$-signal is fitted using one doublet component. This indicates that the platinum atoms are solely bound to the silicon substrate without a significant Pt-Pt bound. XPD measurements and simulation of the recorded pattern are performed for the Si $2p$-signal and the Pt $4f$-signal using the EDAC package. Different structural arrangements with a combination of the c(4×2) and the c(4×6) are tested. In an iterative simulation process of both signals a final structure with R-factors below 0.1 is achieved. The structure reveals a deposition of the platinum atoms in a valley bridge position in a T3 adsorption state and a minimal height of $0.58\,Å$ above the top-most silicon layer. The unit cell is described by the matrix $\left(\begin{smallmatrix} 3 & -6 \\ 4 & 0 \end{smallmatrix} \right)$ and contains 4 Pt-atoms above the top-most silicon layer. The top-most silicon atoms, which are arranged in dimers are buckled in one direction on the clean surface and are rearranged between the platinum. A cross-like structure is obtained.

The clean Au(110) surface is prepared with alternating cycles of argon ion sputtering and subsequent annealing. After a final annealing process at $T_{\text{anneal}} \approx 450\,°C$ for approximately 30 min a (2×1) missing-row reconstruction is confirmed by LEED measurements. XPS survey spectra confirmed the cleanness of the sample. High-resolution core-level XPS spectra of the Au $4f$-signal reveal a surface and a bulk component, chemically shifted by $\Delta E_{\text{chem}} = 0.35\,\text{eV}$. Furthermore, XPD measurements are conducted and a simulation of the surface reconstruction confirmed the (2×1)-surface reconstruction as reported in literature. Additionally, a sub-monolayer coverage of silicon is evaporated onto the reconstructed surface.

Silicon on Au(110) can also show different structural arrangements, depending on the silicon coverage. In this work, the focus is set on a low dimensional Au-Si alloy appearing at a coverage of 0.2 ML. Silicon is evaporated onto the surface via physical vapor deposition while the sample is held at a temperature of $T_{\text{sample}} \approx 400\,°C$ to form a stable ordered phase. The process is monitored by XPS survey spectra and LEED

measurements. After the deposition of 0.2 ML silicon, two overlapping domains described by the matrices $\left(\begin{smallmatrix} 10 & -2 \\ -1 & 4 \end{smallmatrix}\right)$ and $\left(\begin{smallmatrix} 10 & 2 \\ 1 & 4 \end{smallmatrix}\right)$ are obtained in the LEED pattern, which has been reported in prior work including a first structural suggestion [7]. Thereby, the characteristic spots of the missing-row reconstruction seem to vanish, thus the suggested structure model is based on a flat and unreconstructed Au(110) surface. High-resolution core-level XPS spectra of the Au $4f$ and the Si $2p$-signals are recorded under normal emission and also a surface sensitive angle. The Au $4f$ spectrum reveals three components. Beside the bulk signal, two new AuSi components arise with a chemical shift of $\Delta E_{\text{chem}} = 0.67\,\text{eV}$ and $\Delta E_{\text{chem}} = 0.38\,\text{eV}$ for AuSi_1 and AuSi_2, respectively. The Si $2p$-signal also reveals two components that are assigned to AuSi bonds. Subsequently, XPD measurements are recorded of Au $4f$ and the Si $2p$-signals. Iterative simulation of both materials resulted in R-factors below 0.1 which indicates excellent accordance. The new proposed structure contains 12 Si-atoms in the unit cell. Furthermore, it features a rearrangement of the top-most missing-row Au-atoms to a new structure between the silicon. This is likely an indicator for the vanishing reconstruction spots in the LEED pattern. Additionally, a decomposition of the XPS Si $2p$-signal is performed. An identification of the two distinct chemical environments is accomplished. The Si_1 component origins from one single Si-atom on top of a triplet of Au-atoms. The Si_2 component is assigned to a Si-atom on top of a gold atom. The components appear with a stoichiometry of 2:1, which is in agreement with both, the results of the XPS and the XPD investigation.

An outlook of the performed analysis is the further investigation of both systems. Especially for the combination of platinum on silicon, additional measurements of the chemical and structural properties will give insights into the characteristics of other known Si-Pt silicide phases. Again, XPS and XPD are the favored methods for this purpose. Additional DFT studies promise to complement the discovered material properties. These can be compared with already existing results in the literature for silicon on gold. Furthermore, an interesting extension of the studies is the modification of the surface alloy type. The alloying of the materials may occur after diffusion of the adsorbed material into the first layers and thus a transition to type 2 could produce new material properties. The addition of another constituent leads to a type 3 surface alloy and thus ternary systems are created. These systems are excellent for studying the characteristics of composed materials. Here, also XPS and XPD measurements are of great advantage as they examine not only the surface but also the interface of the sample.

In summary, this thesis successfully examined two low-dimensional silicon-based surface-structures. The results provide a detailed insight into the chemical and structural properties of the reconstructed Si(100) and Au(110) surfaces as well as the combined systems Pt/Si(100) and Si/Au(110). Photoemission experiments and systematic simulation of different atomic arrangements reveal new proposed structure models for both systems. Most notably, the atoms of the adsorbent material are solely located in the top-most layer, forming type 1 surface alloys.

Chapter A

Appendix

A.1 LEED Si-Pt silicide

Clean Si(100)
E_{kin}=40 eV E_{kin}=60 eV E_{kin}=80 eV E_{kin}=100 eV E_{kin}=120 eV

Si-Pt Silicide
E_{kin}=40 eV E_{kin}=60 eV E_{kin}=80 eV E_{kin}=100 eV E_{kin}=120 eV
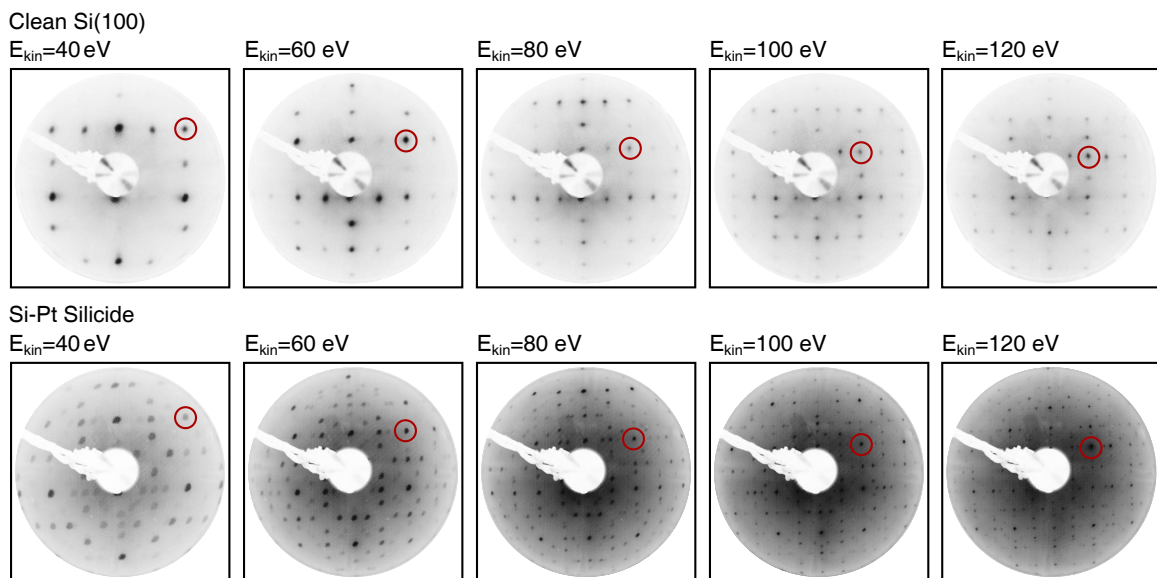
Figure A.1 LEED pattern of reconstructed Si(100) (top) and a Si-Pt silicide coated Si(100)-surface (bottom), recorded at kinetic energies of $E = 40, 60, 80, 100$, and 120 eV, respectively.

A.2 XPS Au-Si alloy

Table A.1 XPS fit parameters of Au $4f$ high-resolution spectra of the clean Au(110) surface at a photon energy of $h\nu = 340\,\text{eV}$. Each spectrum shows a spin-orbit coupling of $3.67\,\text{eV}$.

$\Theta/°$	Comp.	E_{kin}/eV	FWHM/eV	α	A_{rel}/%
60	Au bulk	252.02	0.55	0.04	60
	Au surface	252.37	0.60	0.04	40
0	Au bulk	252.00	0.56	0.04	81
	Au surface	252.35	0.60	0.04	19

Table A.2 XPS fit parameters of Au $4f$ high-resolution spectra of the Au-Si alloy at a photon energy of $h\nu = 340\,\text{eV}$. Each spectrum shows a spin-orbit split couple separated by $3.67\,\text{eV}$.

$\Theta/°$	Comp.	E_{kin}/eV	FWHM/eV	α	A_{rel}/%
60	Au bulk	251.68	0.58	0.04	54
	$AuSi_1$	251.01	0.80	0.04	27
	$AuSi_2$	251.28	0.63	0.04	18
0	Au bulk	251.66	0.58	0.04	72
	$AuSi_1$	250.98	0.79	0.04	17
	$AuSi_2$	251.26	0.62	0.04	11

Table A.3 XPS fit parameters of Si 2p high-resolution spectra of the Au-Si alloy at a photon energy of h$\nu = 180$ eV. The spectra show a spin-orbit coupling of 0.61 eV.

$\Theta/°$	Comp.	E_{kin}/eV	FWHM/eV	α	A_{rel}/%
60	Si$_1$	76.41	0.30	0.14	67
	Si$_2$	76.59	0.29	0.14	33
0	Si$_1$	76.41	0.30	0.14	67
	Si$_2$	76.59	0.28	0.14	33
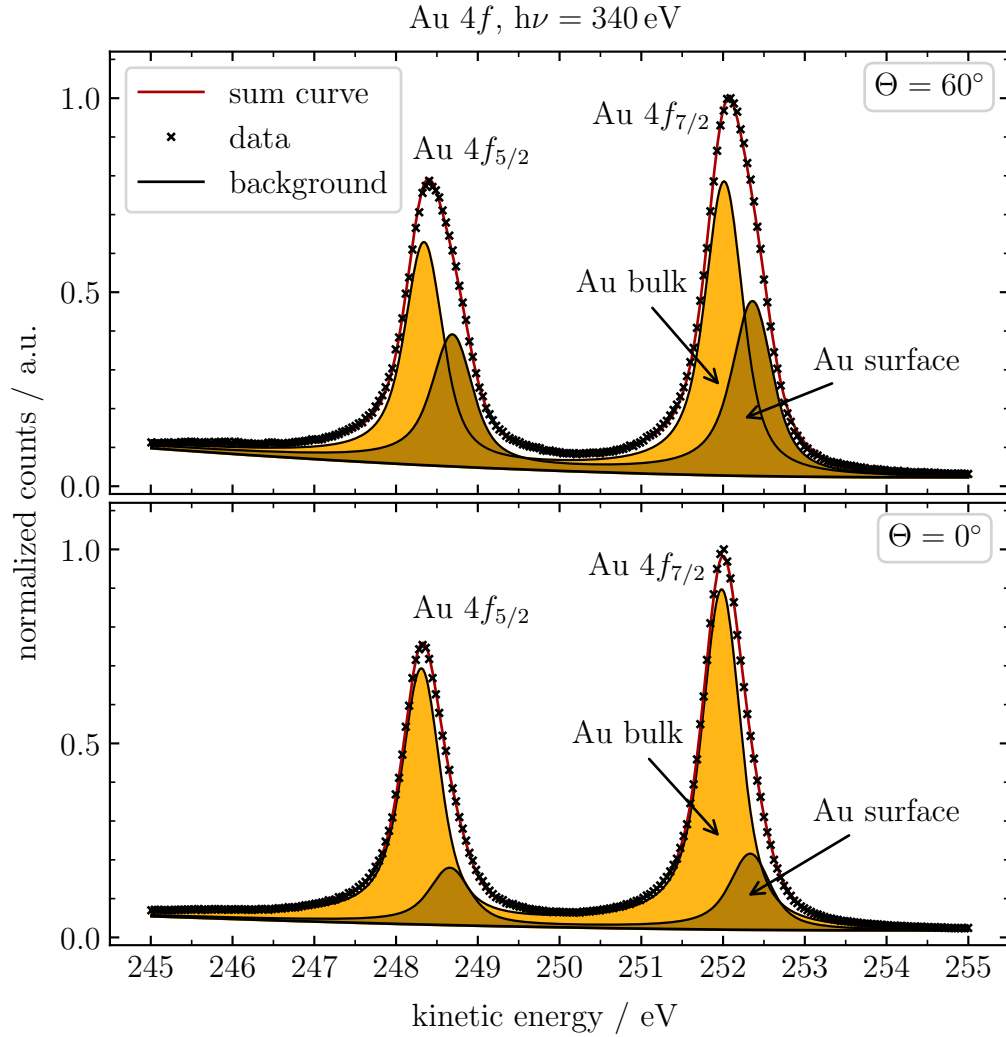
Au $4f$, h$\nu = 340\,\text{eV}$

Figure A.2 High-resolution XPS spectra of the clean Au(110) surface recorded at a photon energy of h$\nu = 340\,\text{eV}$. The Au $4f$ core-level spectra are shown at emission angles of $\Theta = 60°$ and $\Theta = 0°$ in top and bottom panel, respectively. The signal is chemically split into two components, that can be identified as bulk and surface components.
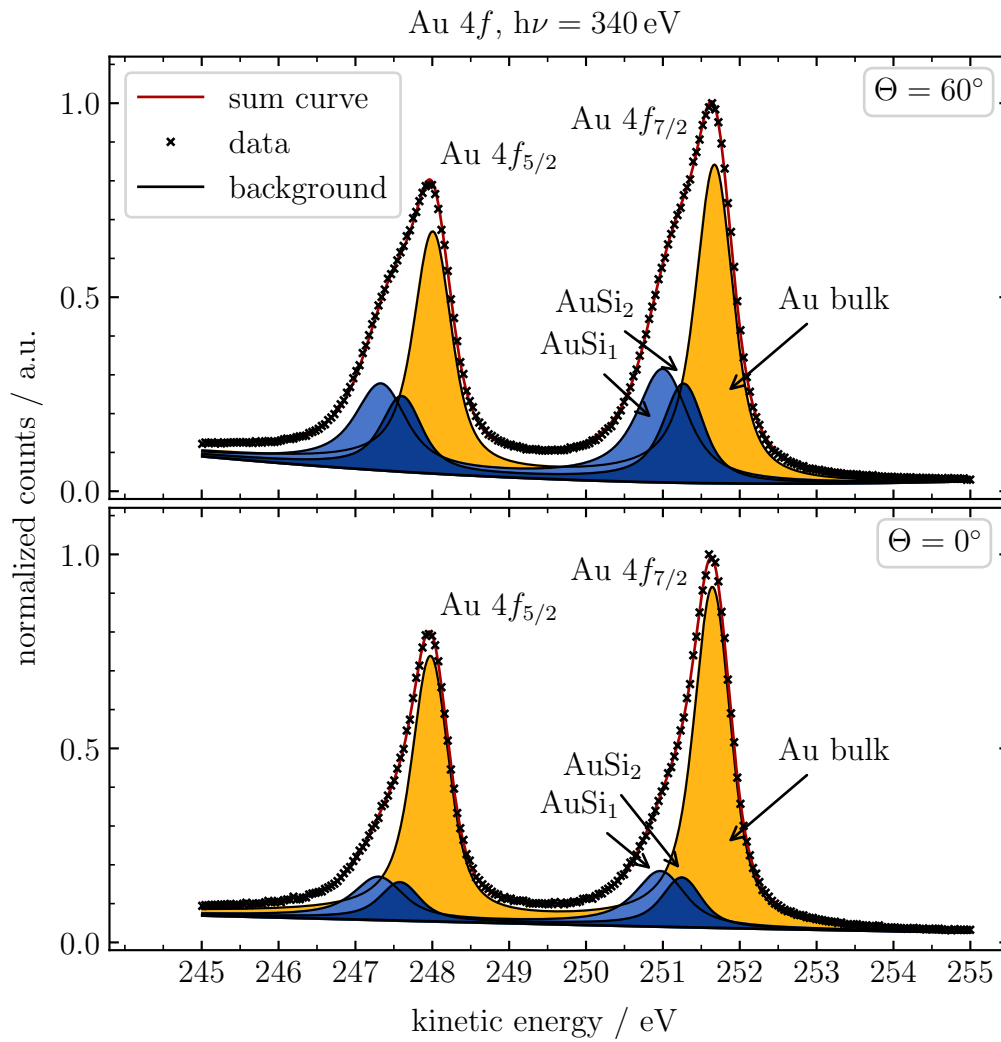
Figure A.3 High-resolution XPS spectra of the Au-Si alloy recorded at a photon energy of h$\nu = 340\,\text{eV}$. The Au $4f$ core-level spectra are shown at emission angles of $\Theta = 60°$ and $\Theta = 0°$ in top and bottom panel, respectively. Besides the Au bulk signal (yellow), two AuSi components arise, shifted towards lower kinetic energies, displayed in blue.
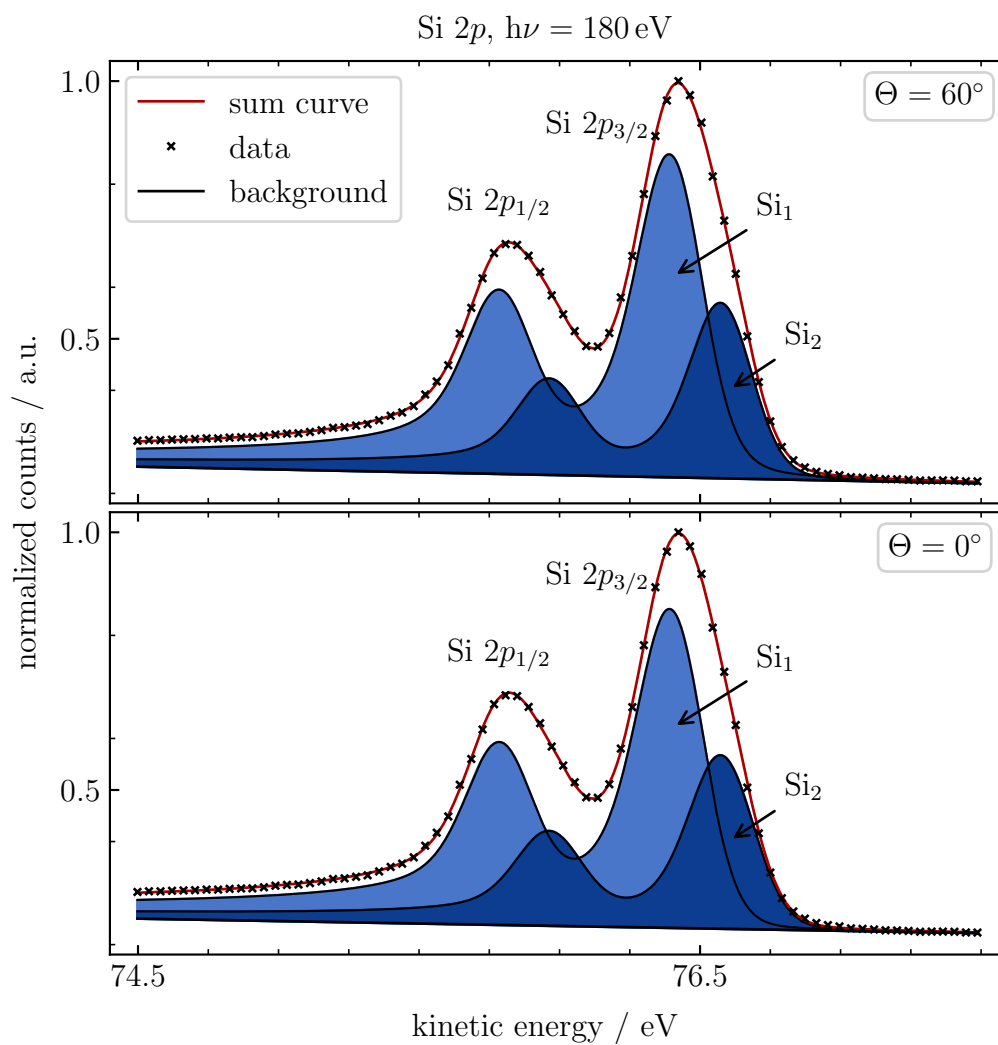
Figure A.4 High-resolution XPS spectra of the Si 2*p*-signal of the Au-Si alloy, recorded at a photon energy of h$\nu = 180$ eV, at emission angles of $\Theta = 60°$ and $\Theta = 0°$ in top and bottom panel, respectively.

List of acronyms

PE	pass energy	18
PGM	plane-grating monochromator	32
QCM	quartz crystal microbalance	34
QN	quantum number	5
sc	simple cubic	6
STM	scanning tunneling microscopy	3
U55	undulator 55	32
UHV	ultra-high vacuum	31
XPD	x-ray photoelectron diffraction	3, 22, III, IV
XPS	x-ray photoelectron spectroscopy	2, 3, 8, III, IV

List of symbols

List of figures

List of tables

Bibliography

[1] R. P. Feynman, *There's Plenty of Room at the Bottom*, Engineering and Science **23**, 22 (1960).

[2] A. S. Sidorenko, *Physics, Chemistry and Biology of Functional Nanostructures III*, Beilstein Journal of Nanotechnology **8**, 590 (2017).

[3] D. A. Stirling, *The Nanotechnology Revolution: A Global Bibliographic Perspective*, CRC Press, Boca Raton, USA (2018).

[4] T. D. Thangadurai, N. Manjubaashini, S. Thomas, and H. J. Maria, *Nanostructured Materials*, Springer Nature, Basingstoke, UK (2020).

[5] D. K. Lim, S.-S. Bae, J. Choi, D. Lee, D. E. Sung, S. Kim, J. K. Kim, H. W. Yeom, and H. Lee, *Unidirectional Pt Silicide Nanowires Grown on Vicinal Si(100)*, The Journal of Chemical Physics **128**, 094701 (2008).

[6] M. Rachid Tchalala, H. Enriquez, A. J. Mayne, A. Kara, S. Roth, M. G. Silly, A. Bendounan, F. Sirotti, T. Greber, B. Aufray, G. Dujardin, M. Ait Ali, and H. Oughaddou, *Formation of One-Dimensional Self-Assembled Silicon Nanoribbons on Au(110)-(2 × 1)*, Applied Physics Letters **102**, 083107 (2013).

[7] H. Enriquez, A. Mayne, A. Kara, S. Vizzini, S. Roth, B. Lalmi, A. P. Seitsonen, B. Aufray, T. Greber, R. Belkhou, G. Dujardin, and H. Oughaddou, *Adsorption of Silicon on Au(110): An Ordered Two Dimensional Surface Alloy*, Applied Physics Letters **101**, 021605 (2012).

[8] H. Hoster, *Properties of Surface Alloys*, in *Surface and Interface Science*, John Wiley & Sons, Hoboken, USA, chap. 12, 61–100 (2013).

[9] R. J. Behm, *Spatially Resolved Chemistry on Bimetallic Surfaces*, Acta Physica Polonica A **93**, 259 (1998).

[10] A. Groß, *Reactivity of Bimetallic Systems Studied from First Principles*, Topics in Catalysis **37**, 29 (2006).

[11] C. Ji, R. Ragan, S. Kim, Y. A. Chang, Y. Chen, D. A. A. Ohlberg, and R. S. Williams, *Surface Reconstruction of Pt/Si(001)*, Applied Physics A **80**, 1301 (2005).

[12] D. S. Choi, J. W. Jung, D. S. Shin, M. S. Yoon, W. S. Cho, J. Y. Kim, K. H. Chae, K. H. Jeong, and C. N. Whang, *Surface Structure of Pt/Si()*, Surface Science **505**, L222 (2002).

[13] H. Itoh, S. Narui, A. Sayama, and T. Ichinokawa, *Low-Energy Electron Diffraction and Scanning-Tunneling-Microscopy Studies of the Pt/Si(001) Surface*, Physical Review B **45**, 11136 (1992).

[14] D. K. Lim, D. Lee, H. Lee, S.-S. Bae, J. Choi, S. Kim, C. Ji, R. Ragan, D. A. A. Ohlberg, Y. A. Chang, and R. S. Williams, *Structure and Electronic Properties of Self-Assembled Pt Silicide Nanowires on Si(100)*, Nanotechnology **18**, 095706 (2007).

[15] C. Leandri, G. L. Lay, B. Aufray, C. Girardeaux, J. Avila, M. E. Dávila, M. C. Asensio, C. Ottaviani, and A. Cricenti, *Self-Aligned Silicon Quantum Wires on Ag(110)*, Surface Science **574**, L9 (2005).

[16] P. Espeter, C. Keutner, P. Roese, K. Shamout, U. Berges, G. Wenzel, L. Bignardi, N. F. Kleimeier, H. Zacharias, and C. Westphal, *Facing the Interaction of Adsorbed Silicon Nano-Ribbons on Silver*, Nanotechnology **28**, 455701 (2017).

[17] P. Roese, K. Shamout, P. Espeter, R. Hönig, U. Berges, and C. Westphal, *Structure Determination of Substrate Influenced Silicon Nano-Ribbon Growth*, Applied Surface Science **467-468**, 580 (2019).

[18] D. Woodruff, *Surface Structural Information from Photoelectron Diffraction*, Journal of Electron Spectroscopy and Related Phenomena **178-179**, 186 (2010).

[19] P. Roese, *Strukturbestimmung einer niedrig-dimensionalen Siliziumstruktur auf einer Au(110)-Oberfläche mittels Photoelektronenspektroskopie und Photoelektronenbeugung*, Ph.D. thesis, TU Dortmund University, Dortmund (2018).

[20] M. Henzler and W. Göpel, *Oberflächenphysik des Festkörpers*, Springer-Verlag, Heidelberg, Berlin, Germany (2013).

[21] S. Hofmann, *Auger- and X-Ray Photoelectron Spectroscopy in Materials Science: A User-Oriented Guide*, Springer Science & Business Media, Heidelberg, Berlin, Germany (2012).

[22] G. Greczynski and L. Hultman, *X-Ray Photoelectron Spectroscopy: Towards Reliable Binding Energy Referencing*, Progress in Materials Science **107**, 100591 (2020).

[23] D. Matsakis, A. Coster, B. Laster, and R. Sime, *A Renaming Proposal: "The Auger–Meitner Effect"*, Physics Today **72**, 10 (2019).

[24] NIST, *X-ray Photoelectron Spectroscopy Database*, 20, National Institute of Standards and Technology, Gaithersburg MD, USA (2000).

[25] J. H. Scofield, *Theoretical Photoionization Cross Sections from 1 to 1500 keV.* (1973).

[26] H. Abitan, H. Bohr, and P. Buchhave, *Correction to the Beer-Lambert-Bouguer Law for Optical Absorption*, Applied Optics **47**, 5354 (2008).

[27] M. P. Seah and W. A. Dench, *Quantitative Electron Spectroscopy of Surfaces: A Standard Data Base for Electron Inelastic Mean Free Paths in Solids*, Surface and Interface Analysis **1**, 2 (1979).

[28] S. Tanuma, C. J. Powell, and D. R. Penn, *Calculations of Electron Inelastic Mean Free Paths for 31 Materials*, Surface and Interface Analysis **11**, 577 (1988).

[29] C. J. Powell, *Practical Guide for Inelastic Mean Free Paths, Effective Attenuation Lengths, Mean Escape Depths, and Information Depths in x-Ray Photoelectron Spectroscopy*, Journal of Vacuum Science & Technology A: Vacuum, Surfaces, and Films **38**, 023209 (2020).

[30] S. Tanuma, C. J. Powell, and D. R. Penn, *Calculation of electron inelastic mean free paths (IMFPs) VII. Reliability of the TPP-2M IMFP predictive equation*, Surface and Interface Analysis **35**, 268 (2003).

[31] NIST, *Electron Inelastic-Mean-Free-Path Database*, 1.2, National Institute of Standards and Technology, Gaithersburg MD, USA (2000).

[32] R. Hesse, C. Bundesmann, and R. Denecke, *Automatic Spike Correction Using UNIFIT 2020*, Surface and Interface Analysis **51**, 1342 (2019).

[33] G. H. Major, N. Fairley, P. M. A. Sherwood, M. R. Linford, J. Terry, V. Fernandez, and K. Artyushkova, *Practical Guide for Curve Fitting in X-Ray Photoelectron Spectroscopy*, Journal of Vacuum Science & Technology A **38**, 061203 (2020).

[34] J. Végh, *The Shirley Background Revised*, Journal of Electron Spectroscopy and Related Phenomena **151**, 159 (2006).

[35] D. A. Shirley, *High-Resolution X-Ray Photoemission Spectrum of the Valence Bands of Gold*, Physical Review B **5**, 4709 (1972).

[36] S. Hüfner, *Photoelectron Spectroscopy: Principles and Applications*, Springer Science & Business Media, Heidelberg, Berlin, Germany (2013).

[37] S. Tougaard, *Quantitative Analysis of the Inelastic Background in Surface Electron Spectroscopy*, Surface and Interface Analysis **11**, 453 (1988).

[38] S. Tougaard, *Practical Guide to the Use of Backgrounds in Quantitative XPS*, Journal of Vacuum Science & Technology A **39**, 011201 (2020).

[39] D. Briggs and J. T. Grant, *XPS: Basic Principles, Spectral Features and Qualitative Analysis*, in: Surface Analysis by Auger and X-ray Photoelectron Spectroscopy, IM Publications LLP, Chichester, West Sussex, UK, 31–36 (2003).

[40] S. Doniach and M. Sunjic, *Many-Electron Singularity in X-Ray Photoemission and X-Ray Line Spectra from Metals*, Journal of Physics C: Solid State Physics **3**, 285 (1970).

[41] P. Auger, *The Auger Effect*, Surface Science **48**, 1 (1975).

[42] C. S. Fadley, *The Study of Surface Structures by Photoelectron Diffraction and Auger Electron Diffraction*, in *Synchrotron Radiation Research: Advances in Surface and Interface Science Techniques*, edited by R. Z. Bachrach, Springer US, Boston, MA, Synchrotron Radiation Research, 421–518 (1992).

[43] C. Westphal, *The Study of the Local Atomic Structure by Means of X-Ray Photoelectron Diffraction*, Surface Science Reports **50**, 1 (2003).

[44] T. Lühr, *Messung und Simulation von XPD Mustern der Si(110)/SiO2-Grenzschicht*, Diploma thesis, TU Dortmund University, Dortmund (2009).

[45] F. J. García de Abajo, M. A. van Hove, and C. S. Fadley, *Multiple Scattering of Electrons in Solids and Molecules: A Cluster-Model Approach*, Physical Review B **63**, 075404 (2001).

[46] R. Gunnella, F. Solal, D. Sébilleau, and C. R. Natoli, *MSPHD: A Full Multiple Scattering Code for Low Energy Photoelectron Diffraction*, Computer Physics Communications **132**, 251 (2000).

[47] R. Rauter, *Berechnung, Vergleich und Analyse von XPD Mustern*, Master's thesis, TU Dortmund University, Dortmund (2017).

[48] R. Döll and M. A. van Hove, *Global Optimization in LEED Structure Determination Using Genetic Algorithms*, Surface Science **355**, L393 (1996).

[49] D. P. Woodruff and A. M. Bradshaw, *Adsorbate Structure Determination on Surfaces Using Photoelectron Diffraction*, Reports on Progress in Physics **57**, 1029 (1994).

[50] M. A. van Hove, W. H. Weinberg, and C.-M. Chan, *Low-Energy Electron Diffraction: Experiment, Theory and Surface Structure Determination*, Springer Science & Business Media, Heidelberg, Berlin, Germany (1986).

[51] D. P. Woodruff, *Low-energy Electron Diffraction*, in *Materials Science and Materials Engineering*, Elsevier (2002).

[52] N. W. Ashcroft and N. D. Mermin, *Festkörperphysik*, Oldenbourg Verlag, München, Germany (2013).

[53] K. E. Hermann and M. A. van Hove, *LEEDpat - PC-based software tool to visualize and analyze LEED patterns of substrates and overlayers* (2014).

[54] G. Held, *Low-Energy Electron Diffraction: Crystallography of Surfaces and Interfaces*, in *Methods in Physical Chemistry*, edited by R. Schäfer and P. C. Schmidt, Wiley-VCH Verlag GmbH & Co. KGaA, Weinheim, Germany, 625–642 (2010).

[55] M. Tolan, T. Weis, C. Westphal, and K. Wille, *DELTA: Synchrotron Light in Nordrhein-westfalen*, Synchrotron Radiation News **16**, 9 (2003).

[56] H. Bendfeldt-Hoppe, J. Friedl, A. Gasper, A. Jankowiak, D. Nölle, C. Piel, T. Weis, and K. Wille, *Reconstruction of the 75 MeV Linac of the DELTA Synchrotron Radiation Facility*, Proceedings of EPAC 634 (2000).

[57] R. G. Heine, P. Hartmann, and T. Weis, *Characterisation of the EU-HOM-Damped Normal Conducting 500 MHz Cavity from the Beam Power Spectrum at DELTA*, Proceedings of EPAC 2856 (2006).

[58] H. Winick, G. Brown, K. Halbach, and J. Harris, *Wiggler and Undulator Magnets*, Physics Today **34**, 50 (1981).

[59] C. Westphal, U. Berges, S. Dreiner, R. Follath, M. Krause, F. Schäfers, D. Schirmer, and M. Schürmann, *The Plane-Grating Monochromator Beamline at the U55 Undulator for Surface and Interface Studies at DELTA*, Journal of Electron Spectroscopy and Related Phenomena **144-147**, 1117 (2005).

[60] K. Wille, *Physik der Teilchenbeschleuniger und Synchrotronstrahlungsquellen: Eine Einführung*, Springer-Verlag, Heidelberg, Berlin, Germany (2013).

[61] G. Sauerbrey, *Verwendung von Schwingquarzen zur Wägung dünner Schichten und zur Mikrowägung*, Zeitschrift für Physik **155**, 206 (1959).

[62] SPECS Surface Nano Analysis GmbH, *User manual for the ErLEED optics and power supplies*, Berlin, Germany (2003).

[63] N. M. Ahmed, F. A. Sabah, H. I. Abdulgafour, A. Alsadig, A. Sulieman, and M. Alkhoaryef, *The Effect of Post Annealing Temperature on Grain Size of Indium-Tin-Oxide for Optical and Electrical Properties Improvement*, Results in Physics **13**, 102159 (2019).

[64] J. G. Aase, J. K. Burchill, D. Knudsen, J. P. Hackett, and B. Moffat, *Spatial Resolution and Relative Brightness of a Microchannel Plate Detector System with P20 and P43 Phosphor Screens*, Optical Engineering **50**, 064001 (2011).

[65] O. Sise and T. J. M. Zouros, *Position, Energy, and Transit Time Distributions in a Hemispherical Deflector Analyzer with Position Sensitive Detector*, Journal of Spectroscopy **2015**, 153513 (2015).

[66] K. Hans Wedepohl, *The Composition of the Continental Crust*, Geochimica et Cosmochimica Acta **59**, 1217 (1995).

[67] P. Haas, F. Tran, and P. Blaha, *Calculation of the Lattice Constant of Solids with Semilocal Functionals*, Physical Review B **79**, 085104 (2009).

[68] A. Rastogi, D. K. Tripathi, S. Yadav, D. K. Chauhan, M. Živčák, M. Ghorbanpour, N. I. El-Sheery, and M. Brestic, *Application of silicon nanoparticles in agriculture*, 3 Biotech **9**, 90 (2019).

[69] K. Sakamoto, R. Y. Lochhead, H. I. Maibach, and Y. Yamashita, *Cosmetic science and technology: theoretical principles and applications*, Elsevier, Amsterdam, NL (2017).

[70] L. C. Andreani, A. Bozzola, P. Kowalczewski, M. Liscidini, and L. Redorici, *Silicon Solar Cells: Toward the Efficiency Limits*, Advances in Physics: X **4**, 1548305 (2019).

[71] M. J. S. Spencer and T. Morishita, *Silicene: strucutre, properties and applications*, Springer International Publishing, Basel, CH (2016).

[72] B. H. Lipshutz and Y. Yamamoto, *Introduction: Coinage Metals in Organic Synthesis*, Chemical Reviews **108**, 2793 (2008).

[73] R. Koch, M. Borbonus, O. Haase, and K. H. Rieder, *Reconstruction Behaviour of Fcc(110) Transition Metal Surfaces and Their Vicinals*, Applied Physics A Solids and Surfaces **55**, 417 (1992).

[74] D. J. Chadi, *Atomic and Electronic Structures of Reconstructed Si(100) Surfaces*, Physical Review Letters **43**, 43 (1979).

[75] C. Xiao, X. Wang, X. Pi, S. A. Yang, Y. Feng, Y. Lu, and S. Zhang, *Spontaneous Symmetry Lowering of Si (001) towards Two-Dimensional Ferro/Antiferroelectric Behavior*, Physical Review Materials **3**, 044410 (2019).

[76] A. Ramstad, G. Brocks, and P. J. Kelly, *Theoretical Study of the Si(100) Surface Reconstruction*, Physical Review B **51**, 14504 (1995).

[77] X.-Y. Ren, H.-J. Kim, C.-Y. Niu, Y. Jia, and J.-H. Cho, *Origin of Symmetric Dimer Images of Si(001) Observed by Low-Temperature Scanning Tunneling Microscopy*, Scientific Reports **6**, 27868 (2016).

[78] S. B. Healy, C. Filippi, P. Kratzer, E. Penev, and M. Scheffler, *Role of Electronic Correlation in the Si(100) Reconstruction: A Quantum Monte Carlo Study*, Physical Review Letters **87**, 016105 (2001).

[79] J.-H. Cho and K. S. Kim, *Metastable Phase of Symmetric Dimers on Si(001)*, Physical Review B **69**, 125312 (2004).

[80] Z. Zhu, N. Shima, and M. Tsukada, *Electronic States of Si(100) Reconstructed Surfaces*, Physical Review B **40**, 11868 (1989).

[81] N. Roberts and R. J. Needs, *Total Energy Calculations of Dimer Reconstructions on the Silicon (001) Surface*, Surface Science **236**, 112 (1990).

[82] D. D. dos Reis, F. R. Negreiros, V. E. de Carvalho, and E. A. Soares, *Geometry of the Au(110)-(1×2) Missing-Row Clean Surface: A New LEED and DFT Study*, Surface Science **604**, 568 (2010).

[83] W. Moritz and D. Wolf, *Structure Determination of the Reconstructed Au(110) Surface*, Surface Science **88**, L29 (1979).

[84] D. S. Choi, J. W. Jung, M. S. Yoon, K. H. Jung, and C. N. Whang, *Relaxation of Si Dimer on the Si (001) Surface Induced by Pt Adsorption*, Modern Physics Letters B **16**, 171 (2002).

[85] H. Itoh, S. Narui, H. Tanabe, and T. Ichinokawa, *Nucleation and Surface Reconstruction of Pd on Si(100) Observed by Scanning Tunneling Microscopy*, Surface Science **284**, 236 (1993).

[86] W. Klement, R. H. Willens, and P. Duwez, *Non-Crystalline Structure in Solidified Gold–Silicon Alloys*, Nature **187**, 869 (1960).

[87] J. Han, D. Jeon, and Y. Kuk, *Surface Crystalline Gold Silicide Formation on the Au(100) Surface*, Surface Science **376**, 237 (1997).

[88] L. Tang, F. Li, and Q. Guo, *A Structured Two-Dimensional Au–Si Alloy*, Applied Surface Science **258**, 1109 (2011).

[89] M. Schmitz, L. Kesper, M. G. H. Schulte, P. Roese, U. Berges, and C. Westphal, *Surface and Interface Analysis of a Low-Dimensional Au–Si Surface Alloy on Au(110) by Means of XPS and XPD*, Journal of Physics: Condensed Matter **33**, 275001 (2021).

[90] N. M. Ravindra, K. Ravindra, S. Mahendra, B. Sopori, and A. T. Fiory, *Modeling and Simulation of Emissivity of Silicon-Related Materials and Structures*, Journal of Electronic Materials **32**, 1052 (2003).

[91] A. Mesarwi and A. Ignatiev, *X-Ray Photoemission Study of Y-Promoted Oxidation of the Si(100) Surface*, Surface Science **244**, 15 (1991).

[92] A. Carnera, P. Mazzoldi, A. Boscolo-Boscoletto, F. Caccavale, R. Bertoncello, G. Granozzi, I. Spagnol, and G. Battaglin, *On the Formation of Silicon Oxynitride by Ion Implantation in Fused Silica*, Journal of Non-Crystalline Solids **125**, 293 (1990).

[93] L. I. Johansson, F. Owman, and P. Mårtensson, *High-Resolution Core-Level Study of 6H-SiC(0001)*, Physical Review B **53**, 13793 (1996).

[94] L. Ley, Y. Wang, V. N. Van, S. Fisson, D. Souche, G. Vuye, and J. Rivory, *Initial Stages in the Formation of PtSi on Si(111) as Followed by Photoemission and Spectroscopic Ellipsometry*, Thin Solid Films **270**, 561 (1995).

[95] H. Okamoto, *Pt-Si (Platinum-Silicon)*, Journal of Phase Equilibria **16**, 286 (1995).

[96] C. J. Powell, *Recommended Auger Parameters for 42 Elemental Solids*, Journal of Electron Spectroscopy and Related Phenomena **185**, 1 (2012).

[97] A. Ouerghi, J. Penuelas, C. Andreazza-Vignolle, P. Andreazza, N. Bouet, and H. Estrade-Szwarckopf, *Chemical and Structural Aspects of CoPt Silicide Nanostructures Grown on Si(100)*, Journal of Applied Physics **100**, 124310 (2006).

[98] T. Ichinokawa, H. Itoh, A. Schmid, D. Winau, and J. Kirschner, *Scanning Tunneling Microscopic Studies of Surface Reconstructed Structures for Metal/Si(100) Systems*, Ultramicroscopy **54**, 116 (1994).

[99] R. Nyholm, A. Berndtsson, and N. Martensson, *Core Level Binding Energies for the Elements Hf to Bi (Z=72-83)*, Journal of Physics C: Solid State Physics **13**, L1091 (1980).

[100] A. N. Mansour, *Gold Mg K $_\alpha$ XPS Spectra from the Physical Electronics Model 5400 Spectrometer*, Surface Science Spectra **3**, 197 (1994).

[101] H. Oughaddou, H. Enriquez, M. R. Tchalala, A. Bendounan, A. J. Mayne, F. Sirroti, and G. Dujardin, *Silicene on Ag(111) and Au(110) Surfaces*, in *Silicene: Structure, Properties and Applications*, edited by M. J. S. Spencer and T. Morishita, Springer International Publishing, Basel, CH, 167–181 (2016).

[102] P. D. Padova, C. Leandri, S. Vizzini, C. Quaresima, P. Perfetti, B. Olivieri, H. Oughaddou, B. Aufray, and G. L. Lay, *Burning Match Oxidation Process of Silicon Nanowires Screened at the Atomic Scale*, Nano Letters **8**, 2299 (2008).

Publications

Articles

[A1] W. Tillmann, N. F. Lopes Dias, D. Stangier, M. Bayer, H. Moldenhauer, J. Debus, M. Schmitz, U. Berges, C. Westphal, *Interaction Effects of Cathode Power, Bias Voltage, and Mid-Frequency on the Structural and Mechanical Properties of Sputtered Amorphous Carbon Films*, Applied Surface Science **487**, 857 (2019).

[A2] M. G. H. Schulte, A. Jeindl, I. Baltaci, P. Roese, M. Schmitz, U. Berges, O. T. Hofmann, and C. Westphal, *Structural investigation of caffeine monolayers on Au(111)*, Physical Review B **101**, 245414 (2020).

[A3] M. Schmitz, L. Kesper, M. G. H. Schulte, P. Roese, U. Berges, and C. Westphal, *Surface and interface analysis of a low-dimensional Au-Si surface alloy on Au(110) by means of XPS and XPD*, Journal of Physics: Condensed Matter **33**, 275001 (2021).